von Karman Institute for Fluid Dynamics
Chaussée de Waterloo, 72
B - 1640 Rhode Saint Genèse - Belgium

Project Report 1990-31 June 1990

SWEPT FIN INDUCED SHOCK WAVE/LAMINAR BOUNDARY LAYER INTERACTIONS AN ANALYTICAL, COMPUTATIONAL, AND EXPERIMENTAL STUDY

Thomas R. Bewley

Supervisors : M. Carbonaro & J.F. Wendt

ACKNOWLEDGEMENTS

I would like to gratefully acknowledge the help of my advisors on this project, Prof. Mario Carbonaro and Prof. John Wendt.

I would also like to thank Prof. Herman Deconinck for his advise and assistance on the conical 2-D computations performed in conjunction with his CFD course at the VKI. Robert Struys provided invaluable help applying a code written by Robert Schricke and Pascal Lardy to the present geometry.

Also, it is important to note the help of the VKI technicians and technical assistants, whose time and assistance made these measurements possible, and everyone in the shop, whose craftsmanship did not go unnoticed or unappreciated. Thanks also to Phil Santangelo for help with the experimental work.

I am also grateful for a scholarship and an academic delay from the U.S. Air Force.

To Sarah

ABSTRACT

The three-dimensional interaction of shock waves with flat plate boundary layers is a topic which remains largely unexplained. The basic structure of the separation region is known. However, the importance of different properties of the flow on the precise structure of the separation region is not well understood. Also, the horizontal and vertical growth rates of the separation region are not known. In the turbulent case, the horizontal growth rate appears to be approximately linear. The boundary layer, however, does not grow linearly. It is unclear at this point exactly what effect this has on the rest of the interaction.

Much experimental work has been conducted in the turbulent regime, because this is directly applicable to many situations. It is the philosophy of the author that understanding the laminar interaction is an important prerequisite to such work. Laminar interactions are much easier to model numerically. Since boundary layers are generally thinner for laminar flows at low total pressures than for turbulent flows, the "far field" (in terms of boundary layer thicknesses from the leading edge of the model) can be studied more extensively in the same size tunnel. Laminar boundary layers are less robust than turbulent ones, so separation effects are more pronounced. Possibly most important is the fact that laminar boundary layers grow at a rate of $x^{1/2}$, which is significantly different than the turbulent boundary layer growth rate $x^{4/5}$. For conical bodies, the model and its associated inviscid flow scale with x. Thus, to determine whether the magnitude of the interaction in the far field in both the vertical and horizontal directions scale primarily with the inviscid flow (the so-called conical symmetry of the interaction) or with the boundary layer thickness, it is a more sensitive measure to study the fully laminar case.

The present work approached the problem from several directions. The inviscid flow over the present geometry was first studied in detail. Regimes of shock attachment and flow choking were examined analytically. Conical Euler computations examined flow field structures. Finally, swept fins were designed and constructed for a laminar Mach 2 facility at the VKI, and a series of LDV measurement of streamwise velocities and flow visualizations begun.

The main goals of the experiments are: 1) to measure the horizontal and vertical growth rates of the interaction region, which need not be equal, and 2) to provide benchmark velocity profiles to be used to verify numerical codes. Once a fully 3-D, viscous numerical code is able to reproduce the streamwise velocity profiles measured in these tests, it can be reliably used to examine the entire interaction region. Only then can the secrets of this phenomenon be revealed.

TABLE OF CONTENTS

Acknowledgements.....iii
Abstract.....v
Table of Contents.....vii
List of Figures.....viii
Nomenclature.....ix

Chapter 1 - Introduction.....1

Chapter 2 - Analytical and Computational Study of Inviscid Flow.....4
2.1 Prediction of shock attachment to edges.....4
2.2 Prediction of flow choking.....5
2.3 Computation of complete inviscid flow field.....9
2.4 Curvature of the inviscid shock.....10
2.5 Examination of flow field structures.....12
2.6 Shock generator geometry.....13
2.7 Effect of flow field structures on shock/boundary layer interactions.....15

Chapter 3 - Experimental Investigation.....17
3.1 Model size and positioning in the nozzle.....17
3.2 Surface flow visualizations.....18
3.3 Flow seeding.....21
3.4 Preliminary results and analysis.....25

Chapter 4 - Conclusions and Future Projects.....32

Appendix 1 - Conical Formulations of the Euler Equations.....34

Appendix 2 - Plots of Computations of Conical Flows.....36

Appendix 3 - The VKI S-1 Supersonic Tunnel.....50

Appendix 4 - The Laser Doppler Velocimeter.....51

Appendix 5 - Table of Values of Chapman and Rubesin Variables.....58

Appendix 6 - Error Propagation of a Linear Regression Fit.....64

Bibliography.....66

LIST OF TABLES

Table 1: Summary of β_o and $\delta M/\delta\beta$ for entire range of fin sizes at Mach 2.....13
Table 2: Selected values of the Chapman and Rubesin variables.....63

LIST OF FIGURES

Figure 1: Oblique view of set-up with nomenclature and dimensions ix
Figures 2a, 2b: Oblique views of inviscid flows 4
Figures 3a - 3c: Hypothetical bodies for prediction of choking 5
Figures 4a - 4h: Regimes of shock attachment and choking 7, 8
Figures 5: Relation between shock curvature and Mach number gradient behind shock 11
Figures 6a, 6b: Plan views of asymmetric and symmetric fins 14
Figures 7a, 7b: Relaxation effects over asymmetric and symmetric swept fins 15
Figures 8a, 8b: Schlieren photographs indicating starting of the tunnel 17
Figure 9: Characteristics plotted in a nozzle similar to that used in S-1 18
Figure 10: Surface flow visualization via injection of oil covered model 19
Figures 11a, 11b: Flow visualization by disturbance streaks in sublimation pattern 20, 21
Figure 12: New particle seeding system for LDV 22
Figure 13: Schematic of the atomizer used in the seeding system 22
Figure 14a - 14d: Sample histograms of velocity measurements 26
Figure 15: Comparison of velocity (~ f') and deceleration (~ $f''\eta$) profiles for the Chapman and Rubesin boundary layer 28
Figure 16: Streamwise boundary layer velocity profiles for first velocity survey 29
Figure 17a - 17d: Model of structure of the normal fin induced shock wave/turbulent boundary layer interaction proposed by Settles et. al. 30
Figure 18: Comparison of methods for evaluating velocity histograms 31

Appendix 2

Figures 19a, 19b: Velocity vectors plotted in a cross-flow plane 36
Figure 20: Example of grid used for numerical computations 37
Figure 21a - 21ff: Pressure isolines for Euler flow over various fins in a cross-flow plane .. 38-48
Figures 22a, 22b: Numerical solution plotted on IRIS workstation with PLOT3D 49

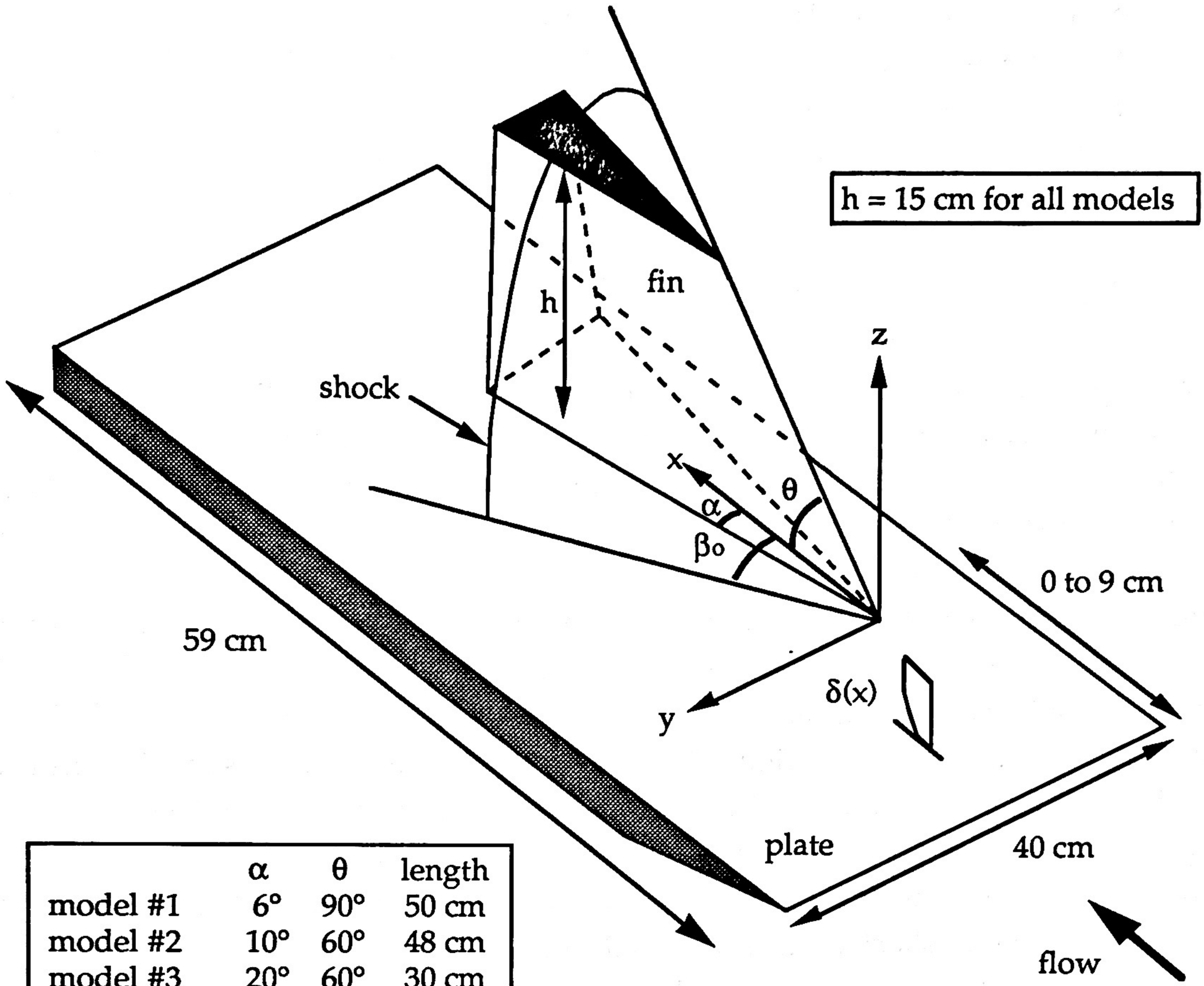
Appendix 3

Figure 23: S-1 50

Appendix 4

Figure 24: LDV system, oblique view 51
Figure 25: Schematic of beam collimator 52
Figure 26: Operation of polarization rotator 52
Figure 27: Operation of a laser in various TEM_{XX} modes 54
Figure 28: Probe volume fringes 56

NOMENCLATURE



	α	θ	length
model #1	6°	90°	50 cm
model #2	10°	60°	48 cm
model #3	20°	60°	30 cm
model #4	20°	30°	30 cm

Figure 1: Oblique view of set-up with nomenclature and dimensions

α = half angle of fin in x-y plane (plane of plate)

θ = half angle of fin in x-z plane (plane of symmetry)

λ_1 = $\pi/2 - \alpha$ = bottom edge sweepback angle

λ_2 = $\pi/2 - \theta$ = top edge sweepback angle

β_o = inviscid shock wave angle on test surface measured from x axis

δ = boundary-layer thickness (a function of the distance in the x direction to the leading edge of the plate)

x_1 = set back distance of fin from leading edge of plate

M = Mach number

$(\,)_n$ = normal section angle (angle taken in a plane normal to an edge line)

x, y, z = Cartesian coordinate system as indicated above.

R, β, ϕ = Spherical coordinate system, $R = x^2 + y^2 + z^2$, $-\pi/2 \le \phi \le \pi/2$, $-\pi < \beta \le \pi$,
$\phi = 0, \beta = 0$ corresponds to the positive x-axis,
$\phi = 0, \beta = \pi/2$ corresponds to the positive y-axis, and
$\phi = \pi/2$ corresponds to the positive z-axis.

r, β, z = Cylindrical coordinate system, $r = x^2 + y^2$, β and z defined as above.

"top edge": the ray defined by the angle θ in figure 1.

"bottom edges": the rays defined by the angles α and $-\alpha$ in figure 1.

"fin vertex": $x = y = z = 0$ in figure 1.

"conical flow": flow which is constant (ρ, ρu, ρv, ρw, and ρE are constant) along rays from an origin somewhere in the flow. This <u>does not</u> imply that the flow itself is aligned with these rays. Further, this does not imply the shape of the body is a cone - it means the body must must be aligned with rays from the origin. Such is the case for the fins under consideration.

"semi-infinite": a body large enough in extent that the region of the flow under consideration would be the same if the body extended to infinity.

"normal fin": a body as shown in figure 1 for which $\theta=90°$.

"swept fin": a body as shown in figure 1 for which $\theta<90°$, with α and θ such that the inviscid shock (shown approximately in figure 1) remains attached to the top edge of the fin.

"compression ramp" or "compression corner": a body as shown in figure 1 for which $\alpha=90°$.

"swept compression corner": a body as shown in figure 1 for which $\alpha<90°$, with α and θ such that the inviscid shock remains attached to the bottom edge.

"far field": that part of the shock wave - boundary layer interaction region away from the fin vertex in which the interaction region has been fully established. It is hypothesized that some sort of symmetry exists in this region.

Chapter 1 - Introduction

The geometry under consideration in this project is illustrated in figure 1. The specific region under investigation is the area in which the shock wave induced by the swept fin impinges on the boundary layer of the flat plate. In this interaction region, three dimensional separation effects are clearly seen experimentally. The basic structure of this interaction is well understood, and is similar in the cross-flow plane to 2-D shock-induced boundary layer separation. It contains, among other things, a separation shock, a separation line, a reattachment line, and a recirculation bubble. This recirculation bubble is not closed in the 3-D case because the bubble grows (and therefore takes in more fluid) as it progresses downstream.

There are several possible contributing factors to the interaction region, including:

1) boundary layer thickness and growth rate,
2) inviscid shock wave strength and angle, and
3) inviscid shock wave curvature and flow field gradients behind the shock.

Also, the size and growth rate of the separation region immediately upstream of the region in question may be identified as another important parameter. We may thus expect to see an "inception" region near the origin of the shock (where the height of the boundary layer is comparable to the height of the model) in which the upstream separation region is reduced, and a "developed" region away from the origin of the shock in which the effect of upstream separation reaches a constant level and some sort of symmetry may be seen.

To study the influence of each factor in an overall equation governing boundary layer separation, some factors must be varied with respect to the others, and the effects noted. The boundary layer thickness and growth rate can be varied by changing the measurement position and the total conditions. The set back distance of the fin from the leading edge may be varied to study the inception distance. To vary parameters 2 and 3, different shock generators must be employed. For these tests, a series of symmetric swept fins were chosen.

The viscous boundary layer in the region under consideration is only 2 mm high. The features of the inviscid flow behind the shock in this region vary on a length scale which is at least an order of magnitude larger. Thus, it is appropriate for an initial analysis to examine these two parts separately. Disturbances in the viscous layer, and the layer itself, alter the inviscid flow to some degree, but a calculation of the flow without this layer provides useful information on where the shock may be expected and how the flow varies behind the shock. A thorough understanding of this theoretical inviscid flow is important in the analysis of the extent of the interaction of the two regimes.

The inviscid flow is first examined in chapter 2. Oblique shock theory can be used to evaluate whether or not the shock created by the fin can attach to either the top or bottom edge of the fin. Also, oblique shock theory and comparisons to cone flow solutions may be used to estimate the choking point of these fins. Analyses of these problems are made in sections 2.1 and 2.2.

For the calculation of the complete inviscid flow field over the present geometry, the 3-D Euler equations can be reduced to two dimensions. This is so because the semi-infinite model (considered infinite in extent) has no length scale. The Euler equations themselves may be cast in a non-dimensional form which illustrate that they also contain no length scale. The lack of any length scale in the problem leads to the powerful simplification that all terms in the 3-D Euler equations in spherical coordinates containing derivatives with respect to r may be dropped. A similar sort of analysis allows this conical formulation of the Euler equations to be cast in the cross-flow variables **y** and **z** at a specified downstream location **x**. These formulations are derived in section 2.3 and written out in full in appendix 1.

The curvature of the inviscid shock may be related to the flow gradients behind the shock via an analysis of the equations of flow over a cone. This method is discussed in section 2.4.

An existing conical solver was implemented to compute the inviscid flow over the present geometry in a cross flow plane for a wide variation of fin parameters. Results are presented in section 2.5 and appendix 2.

To produce a suitable grid for the numerical computations, a powerful grid generation technique was developed using conformal mappings. This code was generalized to other geometries and can also be used to find incompressible potential flow solutions. This work is described in full in Ref. [38].

The geometrical considerations of the design of the test fins are discussed in detail in section 2.6. Two competing designs were considered. The decision to use a symmetric design was reinforced by the numerical calculations illustrating that these fins more significantly alter the flow field conditions behind the shock and thus may be more useful in the comparison of the contribution of each factor to the nature of the interaction.

Important conclusions from chapter 2 are summarized in section 2.7. In this chapter, possible implications of the analysis of the inviscid flow on the viscous/inviscous interaction are discussed.

The experimental work completed during this project is discussed in Chapter 3. Positioning of the model in the nozzle is discussed in section 3.1. A schematic of the tunnel itself is given in Appendix 3.

Results of the surface flow visualizations illustrate very good two-dimensionality of the flow in the test section away from the model. A novel technique of surface flow visualization was employed as oil flow visualizations (even using injection models) are somewhat unreliable due to the extended start up and shut down times of the tunnel. This new visualization technique is discussed in section 3.2.

In this project, 3 swept fins were designed and constructed for LDV tests. These 3 fins, and an existing normal fin, are intended for a comprehensive set of LDV tests in the VKI wind tunnel S-1 at Mach 2. The LDV system in use is described in appendix 4. A new seeding system, discussed in section 3.3, was developed for these LDV tests. Some preliminary results of these tests are discussed in section 3.4. The effects of particle lag are also discussed in this section, by comparing to a Chapman and Rubesin boundary layer. A program written to compute the variables used in the Chapman and Rubesin model is included in appendix 5. Also, a method of analysis for error propagation is given in appendix 6.

Conclusions and suggestions for future projects are presented in Chapter 4.

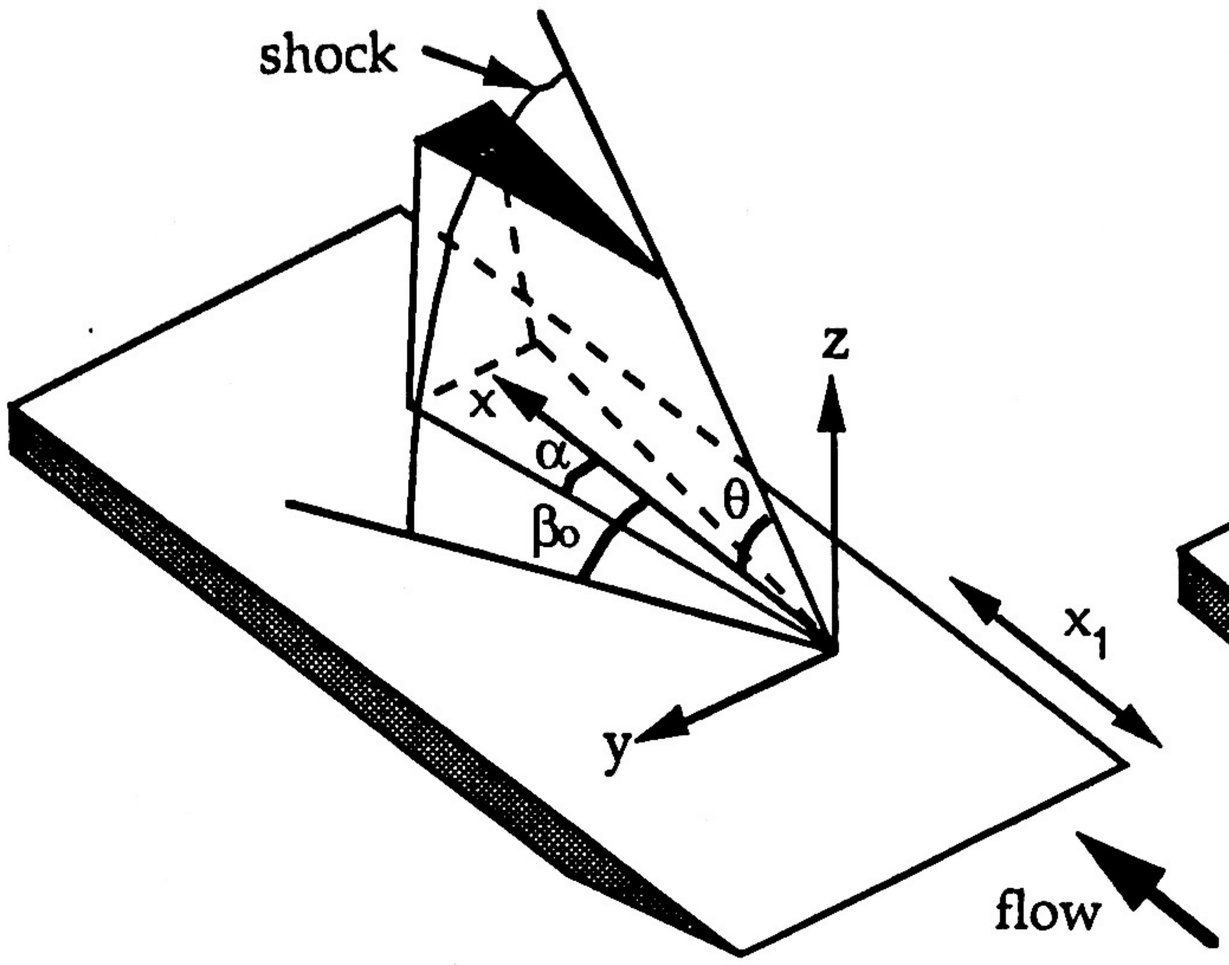


Fig 2a. Swept fin

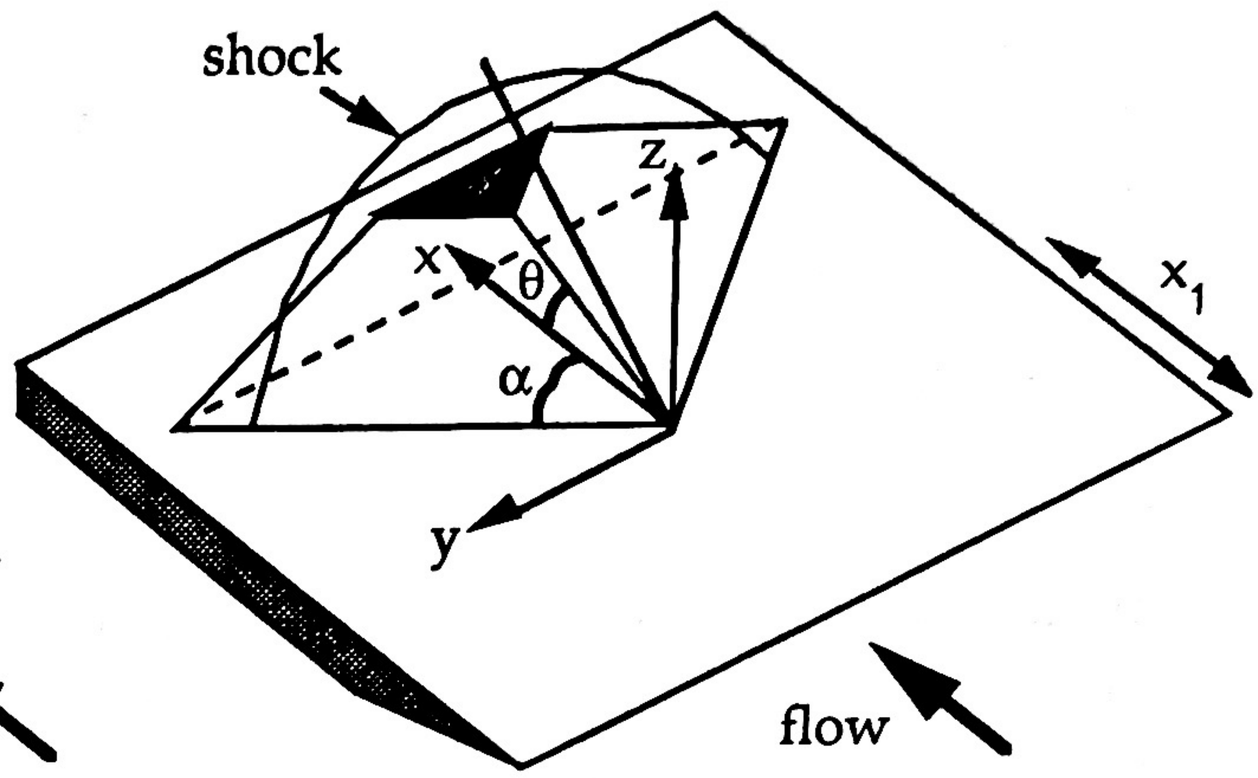


Fig 2b. Swept compression corner

Figure 2: Oblique views of inviscid flows.

This chapter examines the seemingly simple problem of inviscid flow over swept fins and compression corners. A thorough understanding of this class of flows is very important, for it forms the basis for the study of the much more complicated problem of the interaction of inviscid flows with underlying viscous boundary layers. These interactions are of two types: those for which a shock wave terminates on a surface with a boundary layer, such as seen with a swept fin as shown in figure 2a, and those for which a shock wave emanates from a surface with a boundary layer, as seen with a swept compression corner as shown in figure 2b.

The inviscid flow over swept fins has previously been investigated experimentally[1]. By removing the plate in figure 2a, reflecting the fin through the **z=0** plane, and rotating the resulting delta wing around the **x** axis, Schlieren photography can reveal the approximate shock shape. However, as will be shown, this flow is simple enough that computations of the flow are relatively inexpensive and reveal much more information.

2.1 Prediction of shock attachment to edges. For different values of α, θ, and M, the inviscid shock wave may or may not be attached to the top and bottom edges of the fin. The regimes of shock attachment may be calculated as follows:

For any flow for which the shock is attached to an edge, the component of the flow in a plane normal to that edge must be governed by the 2-D oblique shock relations. The condition for shock attachment to the bottom edge of the fin is thus found by comparing the normal section

angle at this edge (a function of both α and θ) to the maximum turning angle at the normal Mach number **M*sin** α allowed by oblique shock theory.

The condition for shock attachment to the bottom of the fin is thus:

$$\theta_n \equiv \text{ArcTan}\left(\frac{\tan\theta}{\sin\alpha}\right) \leq \frac{4}{3\sqrt{3}(\gamma+1)} \frac{\left(M^2 \sin^2\alpha - 1\right)^{1.5}}{M^2 \sin^2\alpha}$$

Likewise, the condition for shock attachment to the top of the fin is:

$$\alpha_n \equiv \text{ArcTan}\left(\frac{\tan\alpha}{\sin\theta}\right) \leq \frac{4}{3\sqrt{3}(\gamma+1)} \frac{\left(M^2 \sin^2\theta - 1\right)^{1.5}}{M^2 \sin^2\theta}$$

2.2 Prediction of flow choking. For large enough α and θ at a given Mach number, the flow chokes. Since there is no length scale in the conical, semi-infinite, inviscid problem, it is immediately recognized that a fixed stand-off distance of the shock from the fin vertex is not possible. Therefore, if the fin angles are so large that the shock must separate from the vertex, the shock propagates infinitely far upstream and chokes the flow. No supersonic solution is possible in this regime. If the fin is finite in extent, on the other hand, a fixed stand of distance of the shock from the fin vertex is possible, with a length scale provided by the size of the fin.

Calculation of the point of flow choking can not be made directly. Comparison of the fin under consideration to bodies for which choking can be predicted becomes useful at this point:

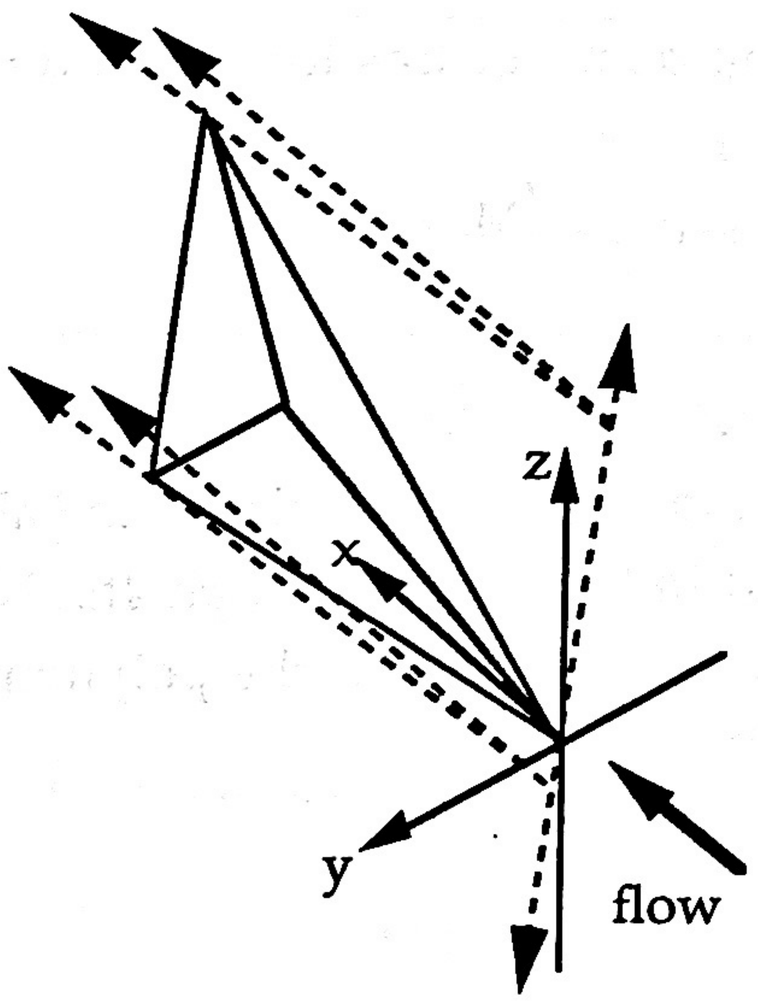


Fig. 3a. Face extended to half plane

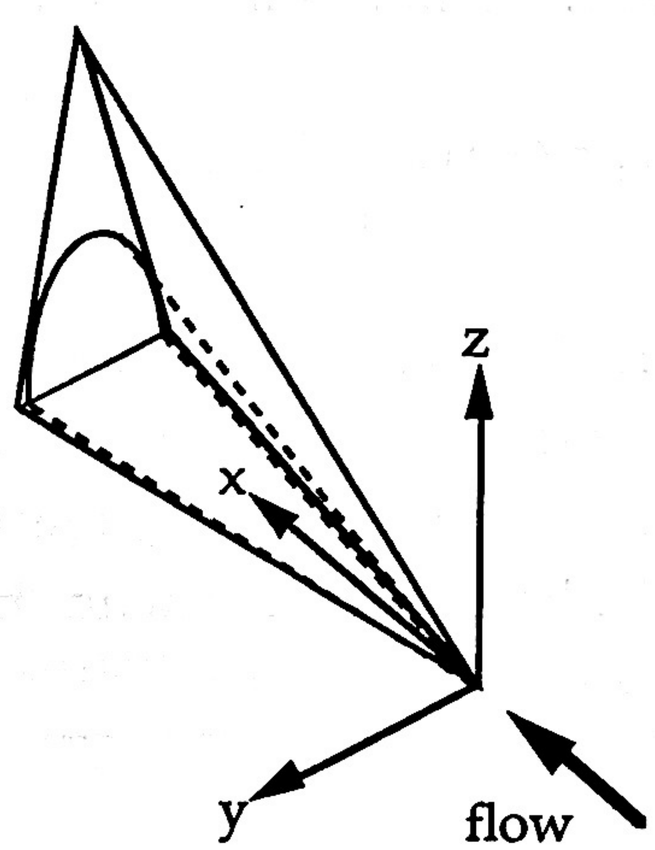


Fig. 3b. Inscribed cone

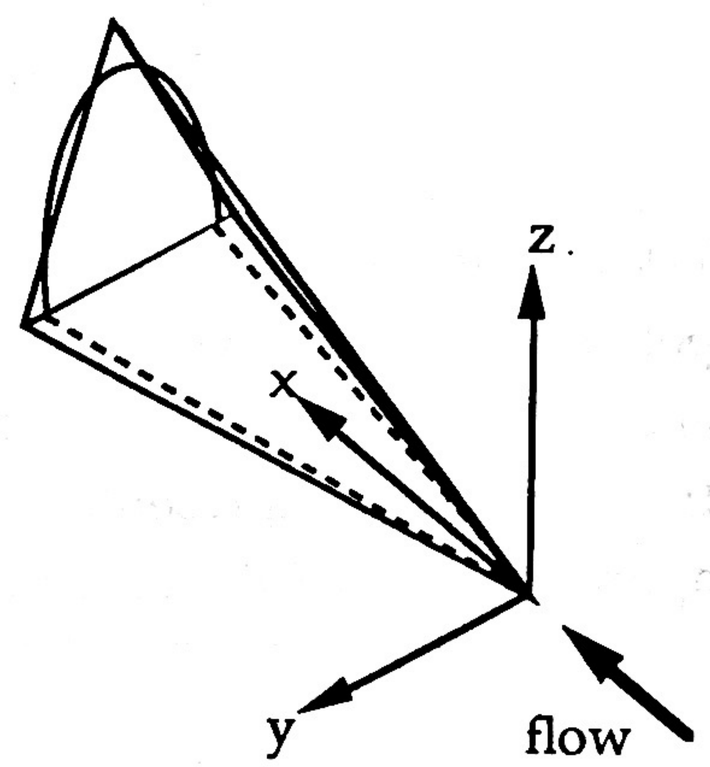


Fig. 3c. Equi-area cone

Figure 3: Hypothetical bodies for prediction of flow choking

If one of the faces of a fin is extended beyond its edges to a half plane bounded by a line for which **x=0**, as shown in figure 3a, the problem reduces to a simple geometry governed by the conventional 2D oblique shock relations, and a lower limit on the region where choking begins may be established. If choking occurs over the fin, it will certainly occur over this body, which is everywhere larger. Further, as either α or θ approaches 90°, the shape of the fin approaches the shape of this body. Thus, such a calculation provides an estimation of the choking point in these limits. One condition for unchoked flow is therefore:

$$\delta_{\text{half plane}} \equiv \text{Arctan}\left(\tan\theta \cdot \sin\left(\text{Arctan}\frac{\tan\alpha}{\tan\theta}\right)\right) \leq \frac{4}{3\sqrt{3}(\gamma+1)}\frac{(M^2-1)^{1.5}}{M^2}$$

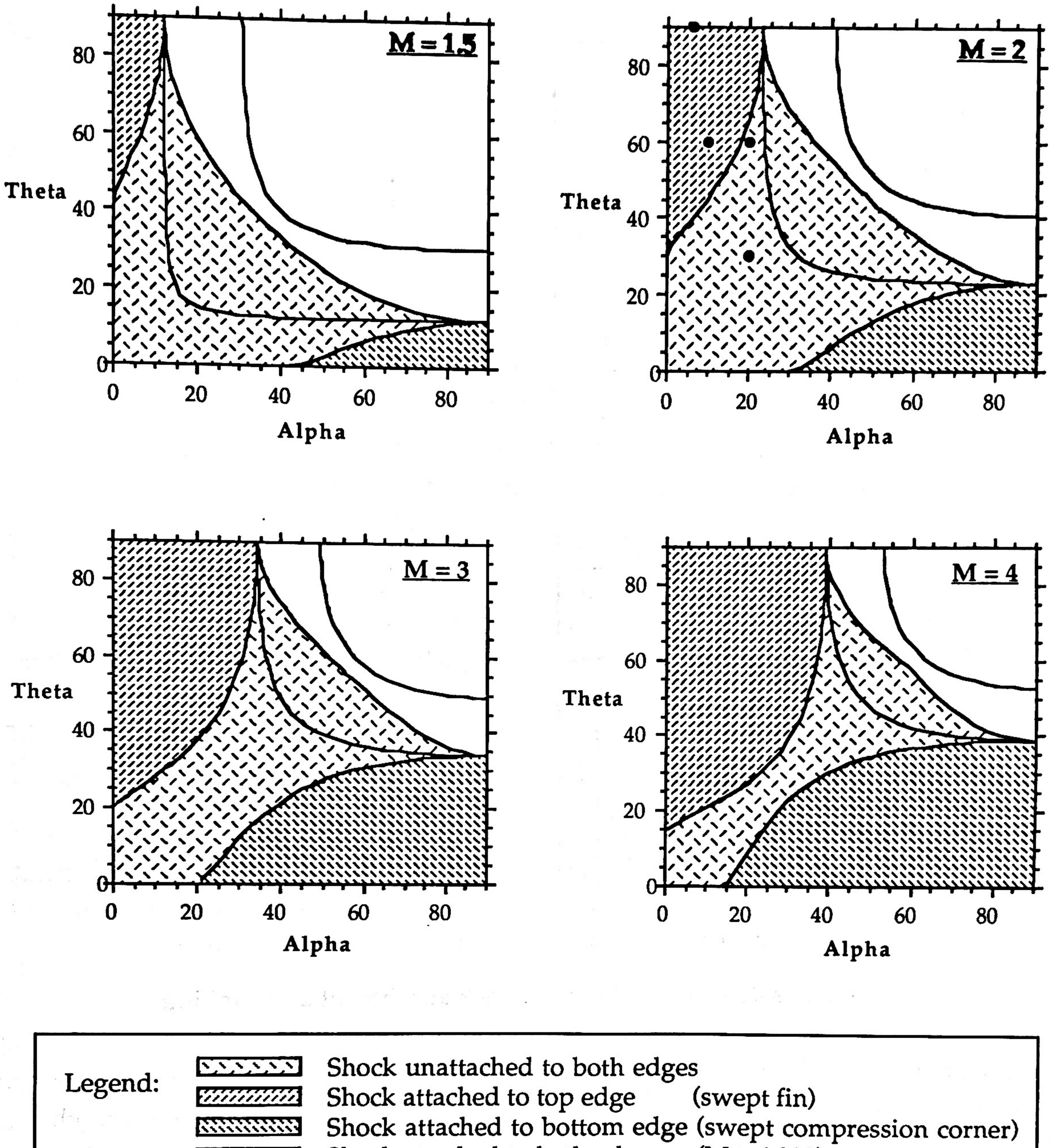
If the fin is replaced by a right circular cone which can be inscribed into the fin, as shown in figure 3b, an upper limit on the region where choking begins may be established. If choking occurs over this cone, it will certainly occur over the fin, which is everywhere larger. The equations for flow over a cone may be reduced to a system of ordinary differential equations and solved numerically, as shown in a following section. Thus, one condition for choked flow is:

$$\delta_{\text{inscribed cone}} \equiv \text{Arctan}\left(\tan\theta \cdot \sin\left(\text{Arctan}\frac{\tan\alpha}{\tan\theta}\right)\right) \geq \delta_{\text{cone choking}}(M, \gamma)$$

In fact, for a fin in which $\alpha \approx \theta$, flow choking occurs at approximately same point as it does for a cone with the same cross-sectional area at a given **x** location, as shown in figure 3c. This idea is physical because shortly before choking occurs over such bodies the flow fields are quite similar. Both shocks are almost perfect cones. It is the total "blockage" that is the important parameter for such fins. Thus, one estimation for the choking point for fins for which $\alpha \approx \theta$ is:

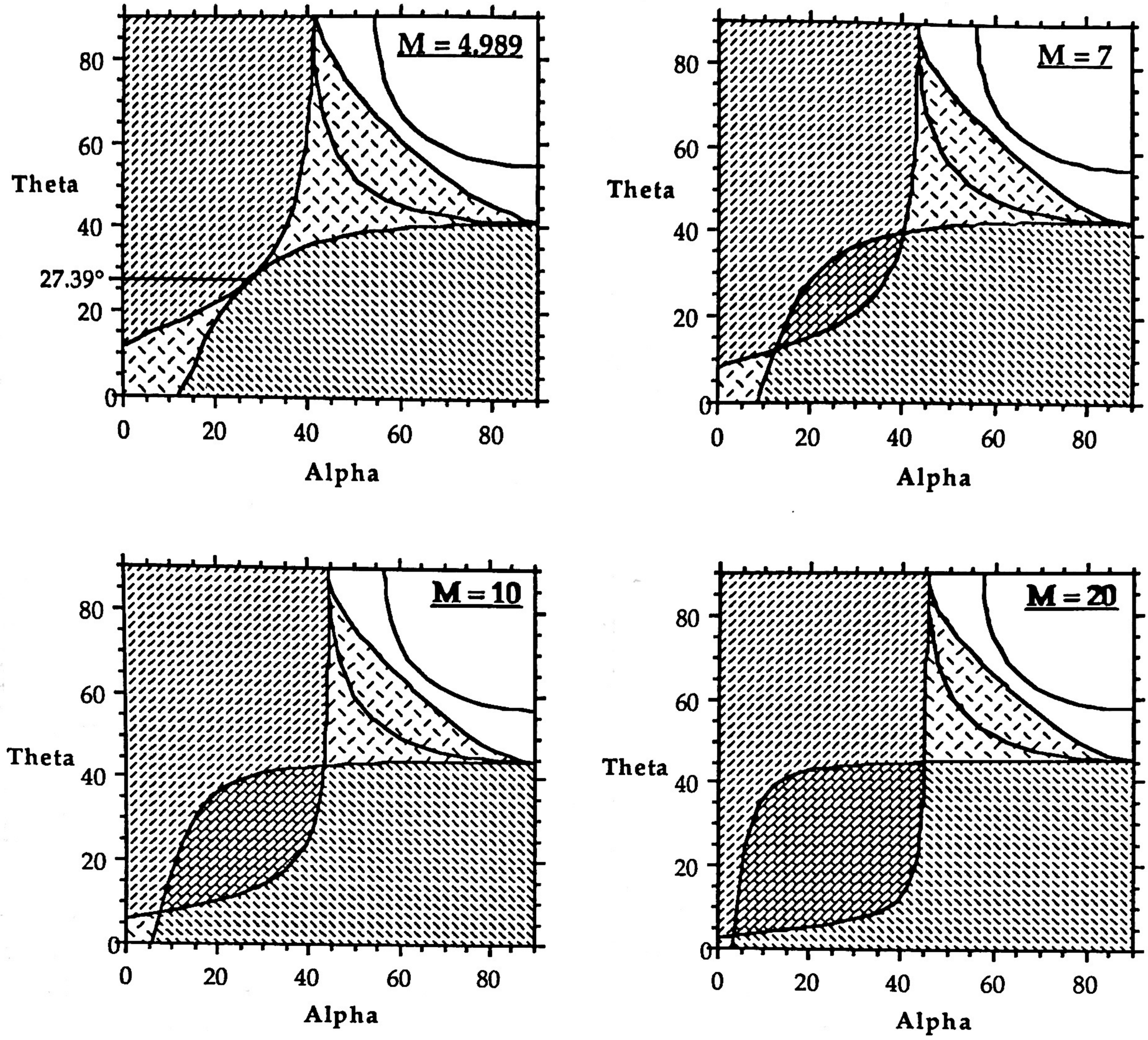
$$\delta_{\text{equi-area cone}} \equiv \text{Arctan}\sqrt{\frac{2}{\pi}\tan\alpha\tan\theta} \approx \delta_{\text{cone choking}}(M, \gamma)$$

Taking the comparisons described above coupled with symmetry considerations, a polynomial curve may be constructed which estimates flow choking. The results of the above analyses of flow choking and shock attachment are illustrated in figures 4a through 4h. Note that the curves representing the limits which contain the choking curve and the polynomial approximation of the curve itself are included.



Figures 4a - 4d: Regimes of shock attachment and choking

(continued on next page)



Figures 4e - 4h: Regimes of shock attachment and choking

Thus, the regimes of shock attachment and choking have been established as a function of Mach number. In addition to "swept fins" and "swept compression corners", two other important classes of fins may be identified: those for which the shock is unattached to both edges, and those for which the shock is attached to both edges. The former can be visualized as a fin for which $\alpha \approx \theta$, or a fin which is quite like a cone in terms of how it affects the flow; the shock attaches only to the fin vertex, and itself is approximately conical in shape. The latter also applies for fins for which $\alpha \approx \theta$, but only at moderate values of these angles and hypersonic Mach numbers for which the shock lies close to the body.

It is easily seen that if the shock is unattached to the top edge, it must be perpendicular to the symmetry plane of the fin, and if the shock is unattached to the bottom edge, it must be perpendicular to the plane of the plate. It is required that the velocity of the flow normal to these planes be zero. This is the case for the free stream flow, which is the condition just upstream of the shock. If the shock were not perpendicular to one of these planes, the flow through the shock would acquire a component of velocity through this plane, and the requirement would be violated. Numerical computations confirm that, if the shock is attached to an edge, it will be angled as required near that edge to satisfy the oblique shock relations in the plane normal to the edge line.

2.3 Computation of complete inviscid flow field. Since the model presents no length scale to the inviscid flow, the flow is strictly conical. In other words, posed in spherical coordinates, all derivatives with respect to **r** may be dropped in the inviscid flow (Euler) equations. When this is done, it is seen that all explicit dependences on **r** also drop, and the equations governing the flow over the fin reduce to the two independent variables β and ϕ.

Posed in Cartesian coordinates, a similar simplification may be made. The requirement that derivatives with respect to **r** must vanish for conical flows may be used to eliminate all derivatives with respect to one of the independent variables, in the present case taken to be the streamwise direction **x**, as follows:

$$\frac{\partial}{\partial r} = \frac{\partial x}{\partial r}\frac{\partial}{\partial x} + \frac{\partial y}{\partial r}\frac{\partial}{\partial y} + \frac{\partial z}{\partial r}\frac{\partial}{\partial z} = 0$$

leads to:

$$\frac{x}{r}\frac{\partial}{\partial x} + \frac{y}{r}\frac{\partial}{\partial y} + \frac{z}{r}\frac{\partial}{\partial z} = 0$$

and finally:

$$\frac{\partial}{\partial x} = -\frac{y}{x}\frac{\partial}{\partial y} - \frac{z}{x}\frac{\partial}{\partial z}$$

When the above condition is applied to the inviscid flow equations in Cartesian coordinates, all derivatives with respect to **x** may be replaced by derivatives with respect to **y** and **z**. When **y** and **z** are both normalized by **x**, it is again seen that all explicit dependences of the equations on **x** drop, and the equations are again posed in two independent variables. Using this conical formulation of the equations, any cross-flow plane of the flow over the fin may be solved via a system of differential equations in two independent variables. The Euler equations in both the conical form and the full 3D form in both spherical and Cartesian coordinates are written out in full in appendix 1.

Viscous terms may be added to this formulation of the equations. Viscous separation effects have been successfully captured via this technique[37]. It is easily seen that, when when all

derivatives with respect to **r** are set equal to zero in the viscous flow (Navier-Stokes) equations in Cartesian coordinates, explicit dependences on **x** are retained in the form of a Reynolds number based on **x**. This provides the equations with enough information to model the boundary layer thickness correctly.

Note that setting all derivatives with respect to **r** in the viscous equations equal to zero imposes a linear, conical growth of the boundary layer, which is clearly incorrect. However, as the boundary layer grows at a rate of $x^{1/2}$ or $x^{4/5}$, this error in boundary layer growth rate becomes less and less important as the boundary layer flattens downstream. Perhaps, then, in the far field, where the effects of nonlinear boundary layer growth have diminished and the separation region is fully established, a conical viscous calculation of the flow may capture all of the important separation phenomenon. If this turns out to be true, such conical calculations will be by far the most economical method of computing separated flows in the far field.

2.4 Curvature of the inviscid shock. An important property of an inviscid shock is its curvature. As a conventional planar two-dimensional oblique shock has an infinite radius of curvature, this quantity is, in a way, a measure of the three-dimensional relaxation effects of the flow. A small radius of curvature indicates significant flow gradients behind the shock. In fact, a relation may be established between shock wave curvature and the Mach number gradient behind the shock by examining cone flow solutions, as described below. In this analysis, the spherical coordinate system reduces to the two independent variables **r** and β, with u_r and u_β the velocities in the positive **r** and β directions, respectively.

For the inviscid flow of a perfect gas over a cone, the equations of conservation of mass, radial momentum, and energy after the shock may be posed as[33]:

$$\frac{\partial f_\beta}{\partial \beta} = - f_r + \frac{f_c^2 \left(f_r + f_\beta \cot \beta\right)}{f_\beta^2 - f_c^2} \qquad \frac{\partial f_r}{\partial \beta} = f_\beta \qquad f_c^2 = \frac{\gamma + 1}{2} - \frac{\gamma - 1}{2}\left(f_\beta^2 + f_r^2\right)$$

where:

$$f_r = \frac{u_r}{c_*} \qquad f_\beta = \frac{u_\beta}{c_*} \qquad f_c = \frac{c}{c_*}$$

The boundary conditions (given by the oblique shock relations and simple geometrical considerations) applied at the shock at some given shock angle $\beta=\beta_o$ are:

$$f_r = \sqrt{\frac{\left(\gamma + 1\right)\cos^2 \beta_o}{\left(\gamma - 1\right) + 2/M_\infty^2}} \qquad f_\beta = - f_r \tan\left(\beta_o - \omega\right)$$

where:

$$\omega = \text{ArcTan}\left[\frac{2\cot\beta_o\left(M_\infty{}^2\sin^2\beta_o - 1\right)}{(\gamma+1)M_\infty{}^2 - 2\left(M_\infty{}^2\sin^2\beta_o - 1\right)}\right]$$

The above ordinary differential equations may be numerically solved up to the (unknown) surface of the cone, at which point $f_\beta = 0$, in order to compute the entire flow field. It is also apparent that the above equations give directly the Mach number gradient behind the conical shock wave as follows:

$$M = \frac{\sqrt{u_\beta{}^2 + u_r{}^2}}{c} = \sqrt{\frac{f_\beta{}^2 + f_r{}^2}{f_c{}^2}} = \sqrt{2} \Big/ \sqrt{\frac{\gamma+1}{f_\beta{}^2 + f_r{}^2} - \gamma + 1}$$

$$\frac{\partial M}{\partial \beta} = \frac{\sqrt{2}\,(\gamma+1)\left(f_\beta\frac{\partial f_\beta}{\partial \beta} + f_r\frac{\partial f_r}{\partial \beta}\right)}{\left(f_\beta{}^2 + f_r{}^2\right)^2\left(\frac{\gamma+1}{f_\beta{}^2 + f_r{}^2} - \gamma + 1\right)^{1.5}}$$

This expression is plotted in figure 5 for different values of free stream Mach number over the full range of shock wave angles allowed at each Mach number. The very surprising result: all the curves collapse to form a general relation between shock wave curvature and Mach number gradient that is independent of free stream Mach number!

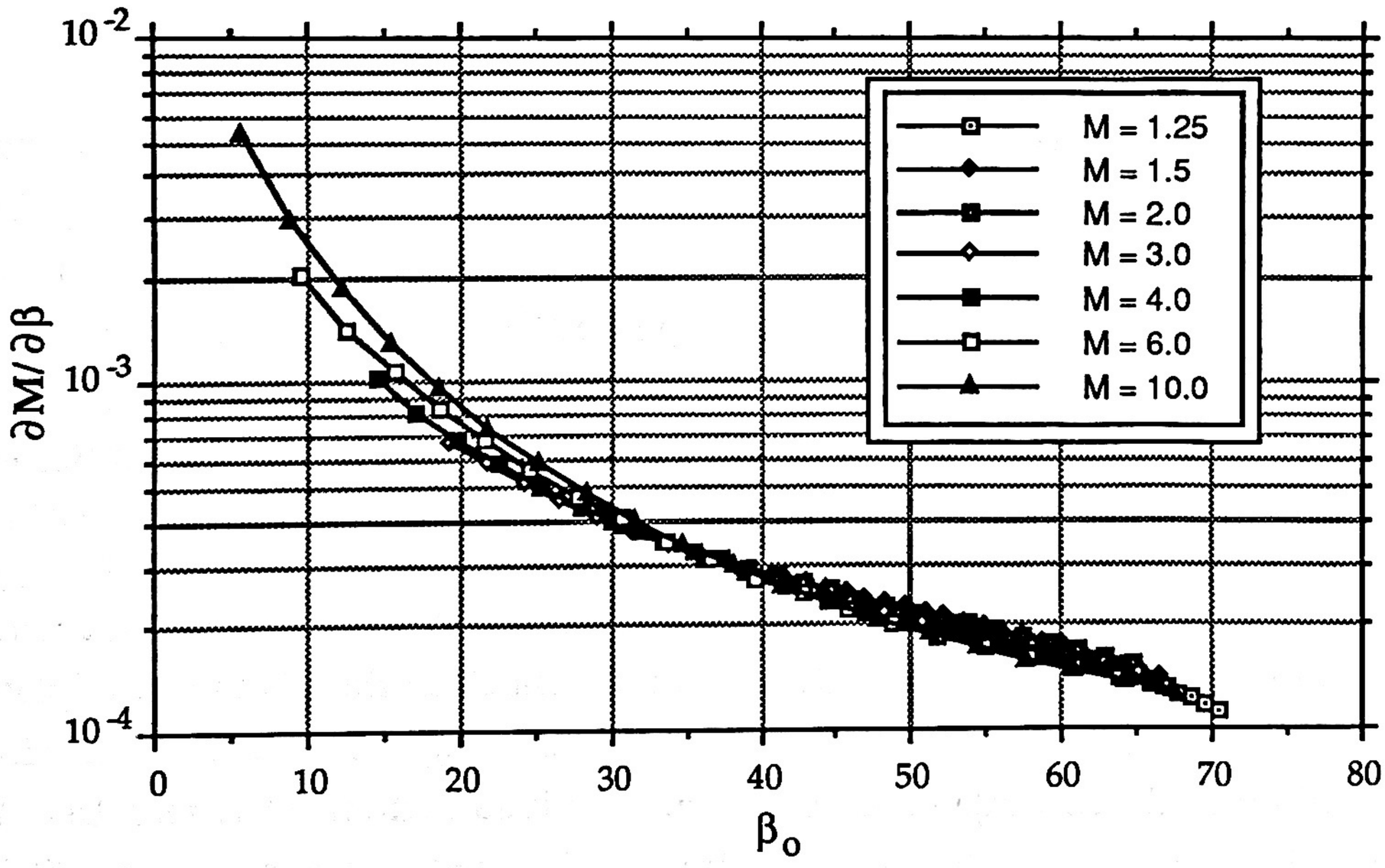


Figure 5: Relation between shock wave curvature and Mach number gradient behind the shock from cone-flow solutions.

The relation in figure 5 may be applied to a more general inviscid shock wave by fitting a cone into the inviscid shock which matches the curvature of the shock at the point in question. By measuring the cone angle in this way, the relation between shock wave curvature and Mach number gradient may then be applied. The accuracy of this technique is confirmed in the next section.

Since the flow is inviscid behind the shock, gradients of pressure and density may be related by the conventional isentropic flow equations:

$$\frac{\partial p}{\partial \beta} = - p_{t,2} \left(1 + \frac{\gamma - 1}{2} M^2 \right)^{\frac{1-2\gamma}{\gamma-1}} \gamma M \frac{\partial M}{\partial \beta}$$

$$\frac{\partial \rho}{\partial \beta} = - \rho_{t,2} \left(1 + \frac{\gamma - 1}{2} M^2 \right)^{\frac{-\gamma}{\gamma-1}} M \frac{\partial M}{\partial \beta}$$

where the total conditions after the shock are given by the conventional oblique shock relations.

Thus, shock wave curvature and flow gradients behind the shock have been related in a general sense. Knowledge of just one of these quantities is enough to find the others. This is important for the study of fin induced shock-wave boundary layer interactions. The pressure gradient behind the shock is the factor that most directly affects separation phenomenon, but some other parameter (for example, the shock wave curvature, via conical shadowgraphy[22]) may be the most accurate quantity to measure.

2.5 Examination of flow field structures. A complete set of 19 flow computations at Mach 2 over the full range of fin angles depicted in figure 3b has been completed. A second order accurate Roe flux vector splitting scheme[37] was used on a grid of 10,000 points constructed using a Schwartz-Christoffel transformation method[36, 38] which provided excellent grid orthogonality and smooth variation of grid density. Additionally, in most cases, the shape of the grid lines was found to fit the shape of the shock quite well. These qualities of the grid were important for maximizing the accuracy of the computations.

The most important results to be noted from these calculations are the shock wave angle and the Mach number gradient immediately behind the shock in the plane of the plate. Table 1 summarizes these quantities. Other parameters concerning the flow in this region may be found according to the formulae derived in the previous section. It is seen that, for the weakest shocks, the conical solver underestimated the shock wave angle by a little over 1°. In all other respects, these values of β_o seem to be quite consistent.

90°	*30°*	*39.31°*	*53.42°*							
80°	*30°*	did not converge								
70°	*30°*	34.1° 8.7e-5	43.1° 5.2e-5							
60°	*30°*	33.2° 1.5e-4	40.8° 9.6e-5	50.15° 8.6e-5						
50°	*30°*	32.3° 2.1e-4	38.9° 1.4e-4	46.45° 1.3e-4	55.2° 1.5e-4					
40°	*30°*	31.75° 3.1e-4	36.9° 1.9e-4	43.3° 1.9e-4	50.75° 2.1e-4	59.0° 2.6e-4				
30°	*30°*	30.7° 4.2e-4	34.85° 3.0e-4	40.15° 2.4e-4	47.0° 3.1e-4	54.63° 4.4e-4	63.0° 6.6e-4			
20°	*30°*	29.2° 4.3e-4	32.7° 3.8e-4	37.4° 3.8e-4	43.65° 4.9e-4	51.33° 1.2e-3	60.10° 1.7e-2	*70°*	*80°*	*90°*
10°	*30°*	28.8°	30.1° 5.1e-4	34.2° 5.8e-4	40.8° 1.9e-3	*50°*	*60°*	*70°*	*80°*	*90°*
0°	*30°*	*30°*	*30°*	*30°*	*40°*	*50°*	*60°*	*70°*	*80°*	*90°*
↑ θ α→	0°	10°	20°	30°	40°	50°	60°	70°	80°	90°

flow
choked

Table 1: Summary of β_0 and $\delta M/\delta\beta$ for entire range of fin sizes at Mach 2.
Normal type indicates results of the conical calculations, italics indicate exact values from 2D oblique shock theory or the shock attachment condition.

For the fins for which $\alpha \approx \theta$, the shock waves are approximately conical. Comparing the shock wave curvature (equal to the shock wave angle β_0) and the Mach number gradient for these fins from Table 1 to the relation found in figure 4 confirms the consistency of these computations.

2.6 Shock generator geometry. There are two logical choices for swept fin geometry: 1) one in which the surface of the fin generating the shock on the measurement side is normal to the plate, and 2) one in which the model is symmetric through a plane which is normal to the plate and the cross flow plane. The second geometry was chosen for this series of experiments. The most important reason is that this geometry varies the flow field conditions behind the shock near the plate most dramatically. Also, this geometry more

reasonably corresponds to fins on real aircraft, such as an F-104 wing, and can more easily be visualized and modelled numerically. This geometry is further illustrated in the figures below.

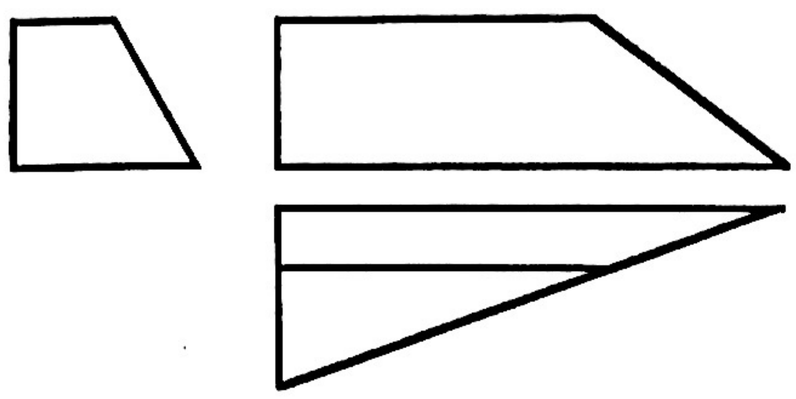


Fig. 6a Asymmetric Fin

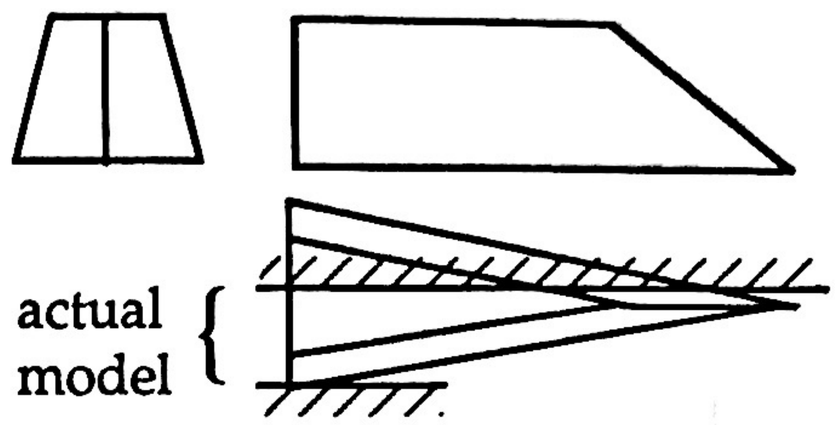


Fig. 6b Symmetric Fin

Figure 6: Plan views of asymmetric and symmetric fins.
(Note: European convention used for all plan views)

For the actual models, complete solid fins were not built, as illustrated in figure 6b. On the side away from the interaction, and in a small region near the rear of some models, material was left out to reduce blockage problems when starting the tunnel (see section 3.1). Note that information about the part of the model missing cannot propagate around the front of the models, for the flow in this region remains supersonic. Also, 3 to 4 windows were cut in each model to allow detection of the forward scatter LDV signals. The dimensions of the fins used are shown in figure 1 - detailed drawings illustrating normal section angles and dimensions of the windows in the fins are on file with Prof. Wendt.

Computationally, a comparison may be made between the flow over the two fins depicted in figure 6. Asymmetric fins have been used in the past by some authors[17] to investigate the effects of flow gradients and shock wave curvature on fin induced shock wave / boundary layer interaction phenomena. As mentioned previously, shock wave curvature is accompanied by flow gradients behind the shock. This is clearly seen in figure 7. By comparing figures 7a and 7b, it is plainly seen that the symmetric swept fin more significantly affects the flow gradients near the plate than does the asymmetric swept fin. Three dimensional relaxation effects (and therefore flow gradients) are seen primarily near the bottom edge of the fin for symmetric swept fins and near the top edge for asymmetric swept fins. Therefore, the symmetric swept fins are better suited for the study of the effects of flow field gradients behind the shock wave on the separation region.

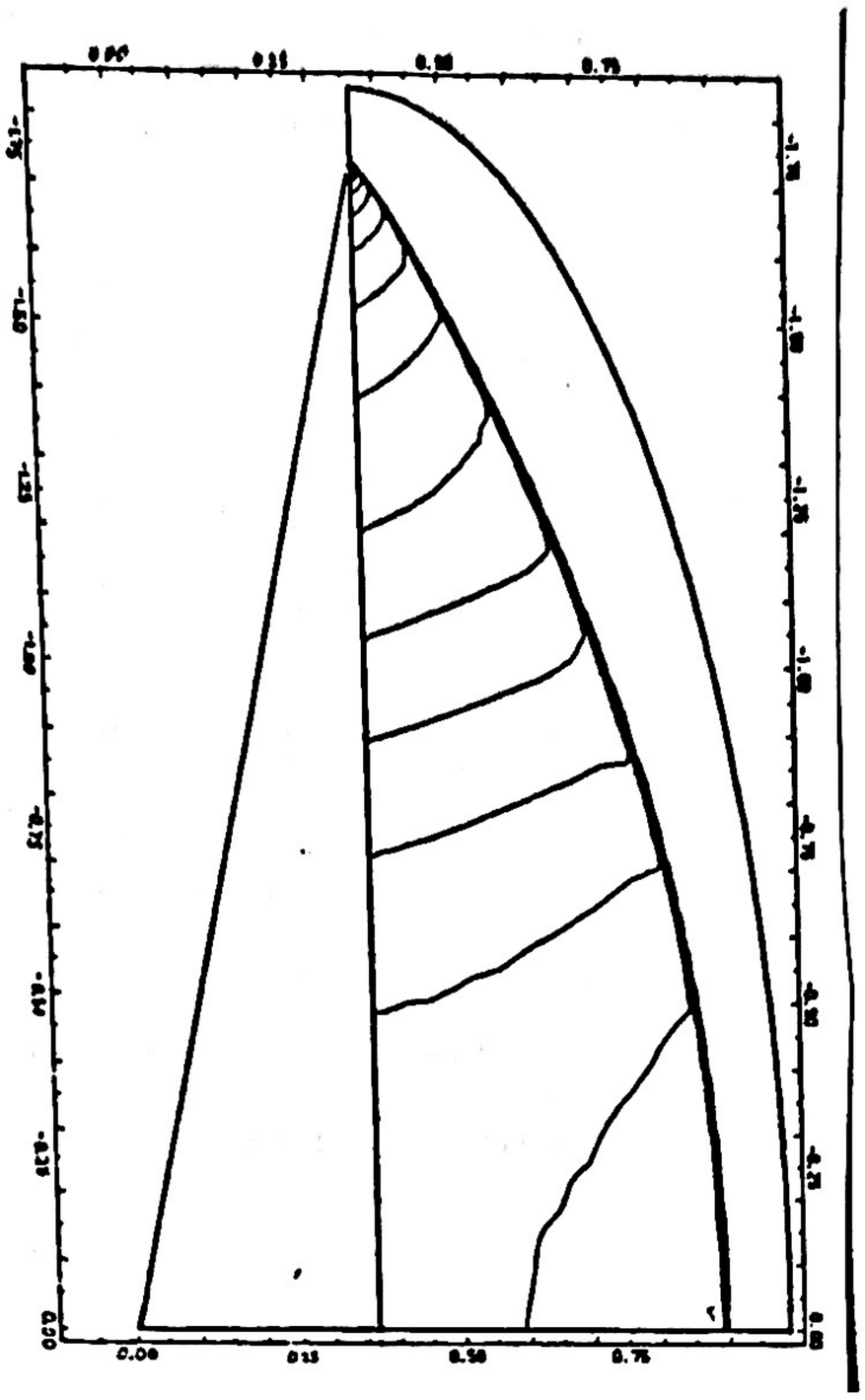


Fig. 7a. Asymmetric swept fin

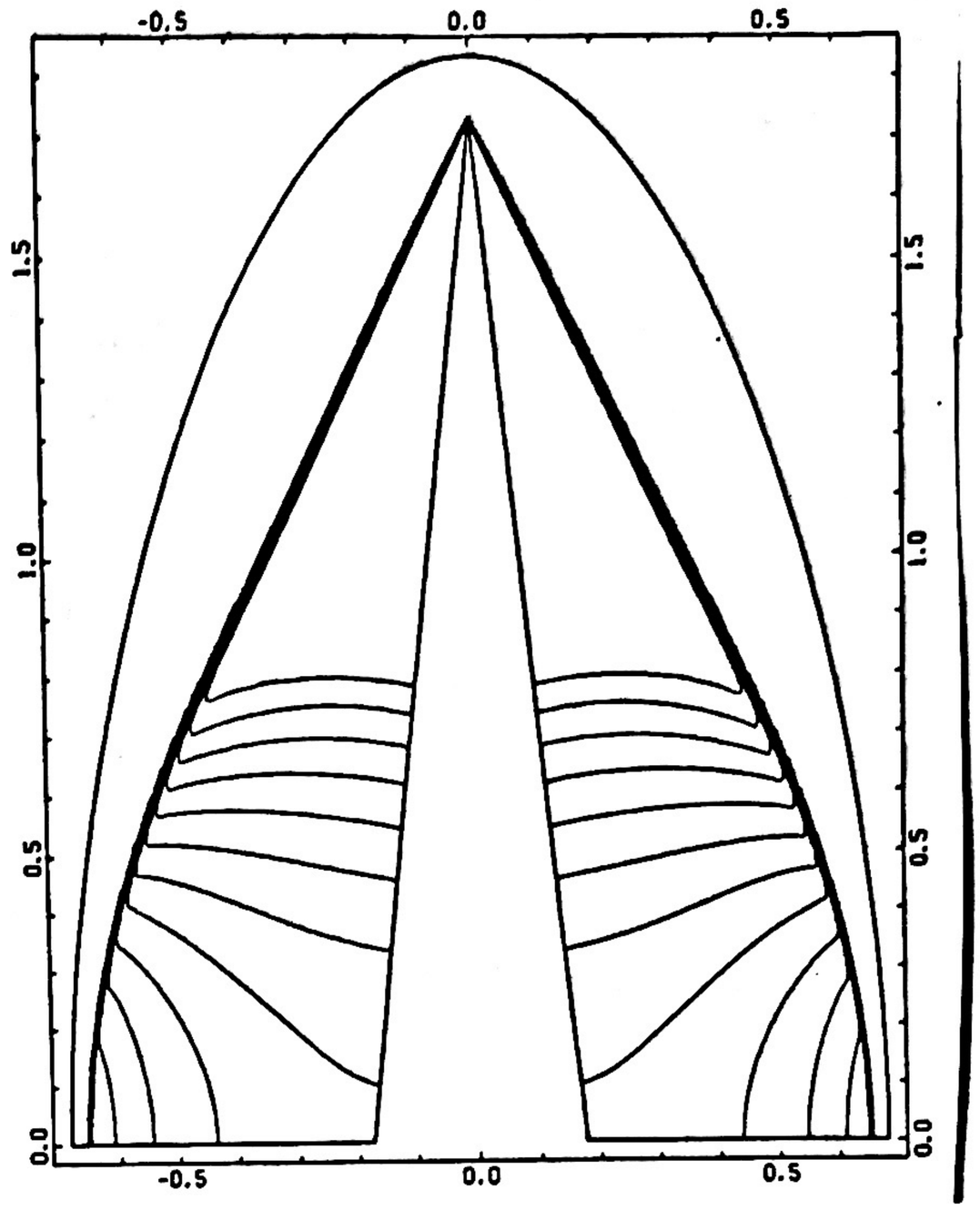


Fig. 7b. Symmetric swept fin

Figure 7: Comparison of relaxation effects over asymmetric and symmetric swept fins at Mach 2. Shown are pressure contours in a cross flow plane.

Both flows shown in figure 7 were calculated on just half of the domain shown. For flows of the second type, the symmetry conditions at the y=0 plane may be exploited, whether or not the shock is attached to the top edge of the model. For flows of the first type, if the shock is attached to the top edge of the model as it is in the figure, the flow may be calculated on just the measurement side, with free stream flow satisfying the boundary conditions everywhere on the opposite side. Note that if the shock detaches from the top edge, this is no longer true.

2.7 Effect of flow field structures on shock/boundary layer interactions. Although the inviscid flow over a normal fin is strictly conical and the inviscid shock wave is the cause of the separation region, the inviscid flow itself does not impart any conical sort of divergence to the underlying viscid flow. The inviscid flow over a normal fin in cylindrical coordinates has no variation in the **r** or **z** directions. In a way, though, it is even simpler than this, for the flow is uniform in front of and behind a planar shock wave through which a jump occurs. If the inviscid flow varied through any other angle β besides the shock wave angle β_o, or if the jump itself occurred through a finite angle $\Delta\beta$, some sort of conical divergence would be imposed on the underlying flow. This, however, is not the case.

For the sake of the boundary layer, the overlying inviscid flow over a swept fin also contains little information about conical divergence, which is contained only in the flow gradients which vary with β.

A similar statement may be made for the inviscid flow over swept compression corners. For bodies in which the flow is well attached to the bottom edge, the flow in the vicinity of this edge is uniform in front of and behind a planar shock wave attached to the edge. This means that the inviscid flow itself again applies no divergence of any sort to the separation region.

The inviscid flow over normal fins and swept and normal compression corners, therefore, contains nothing that imparts any sort of conical divergence to the viscous separation region. The boundary layer separation region is free to grow at the rate dictated by the mass accumulation of the vortex submerged in this region. The growth rates of this region in the vertical and horizontal directions need not be equal. The boundary layer growth rate is probably an important factor contributing to these separation region growth rates.

Chapter 3 - Experimental Investigation

3.1 Model size and positioning in the nozzle. During the start up of the tunnel, it is important that the model is small enough that blockage effects can be overcome by a large difference in pressure so that the flow starts, or becomes supersonic. The starting phenomenon in a wind tunnel is quite complex and is associated with many shocks sweeping through the test section until supersonic flow is established. To confirm that the flow was able to start, Schlieren photographs were taken of the plate in the tunnel without the fin, as shown in figure 8a, and with the fin, as shown in figure 8b (the ports are the LDV viewing windows). Figure 8a illustrates Mach lines from the leading edge of the plate at angle indicative of a free stream of $M \approx 1.9$. Figure 8b illustrates that the flow is not blocked behind the model ($y<0$ in figure 1) where the passage is quite restricted. Small disturbances (pieces of tape) applied to the plate behind these windows produced Mach lines indicated supersonic flow of $M \approx 1.3$.

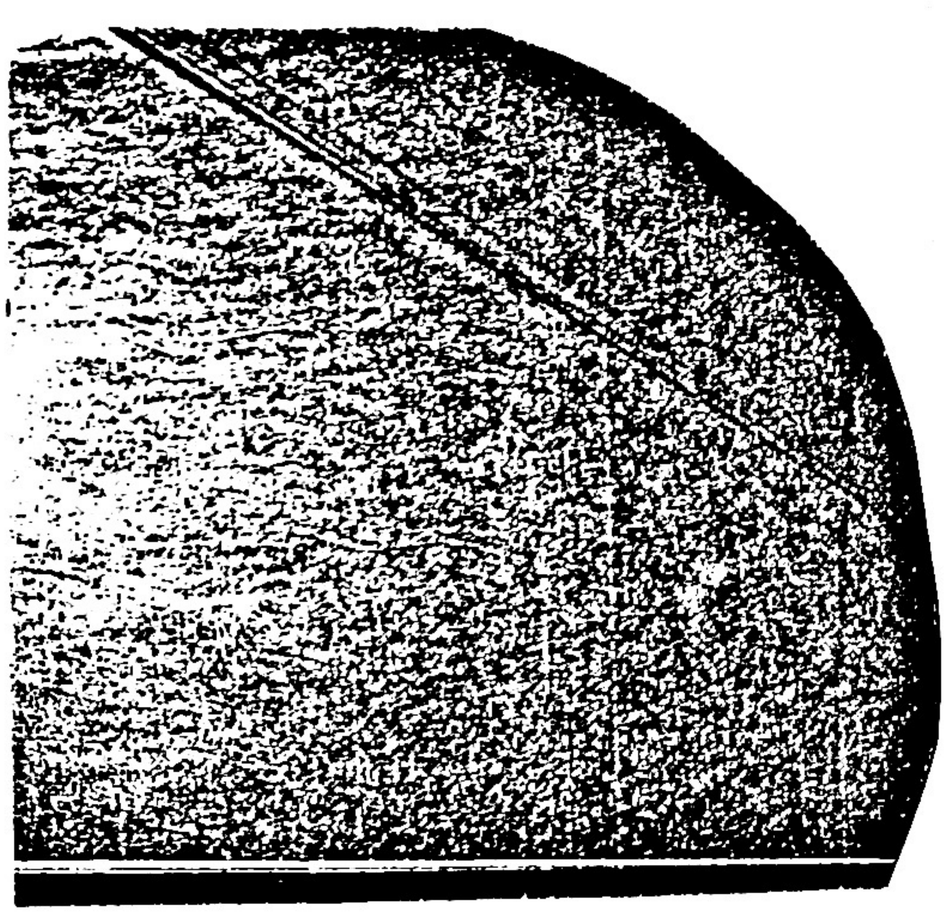


Fig. 8a. Flat plate

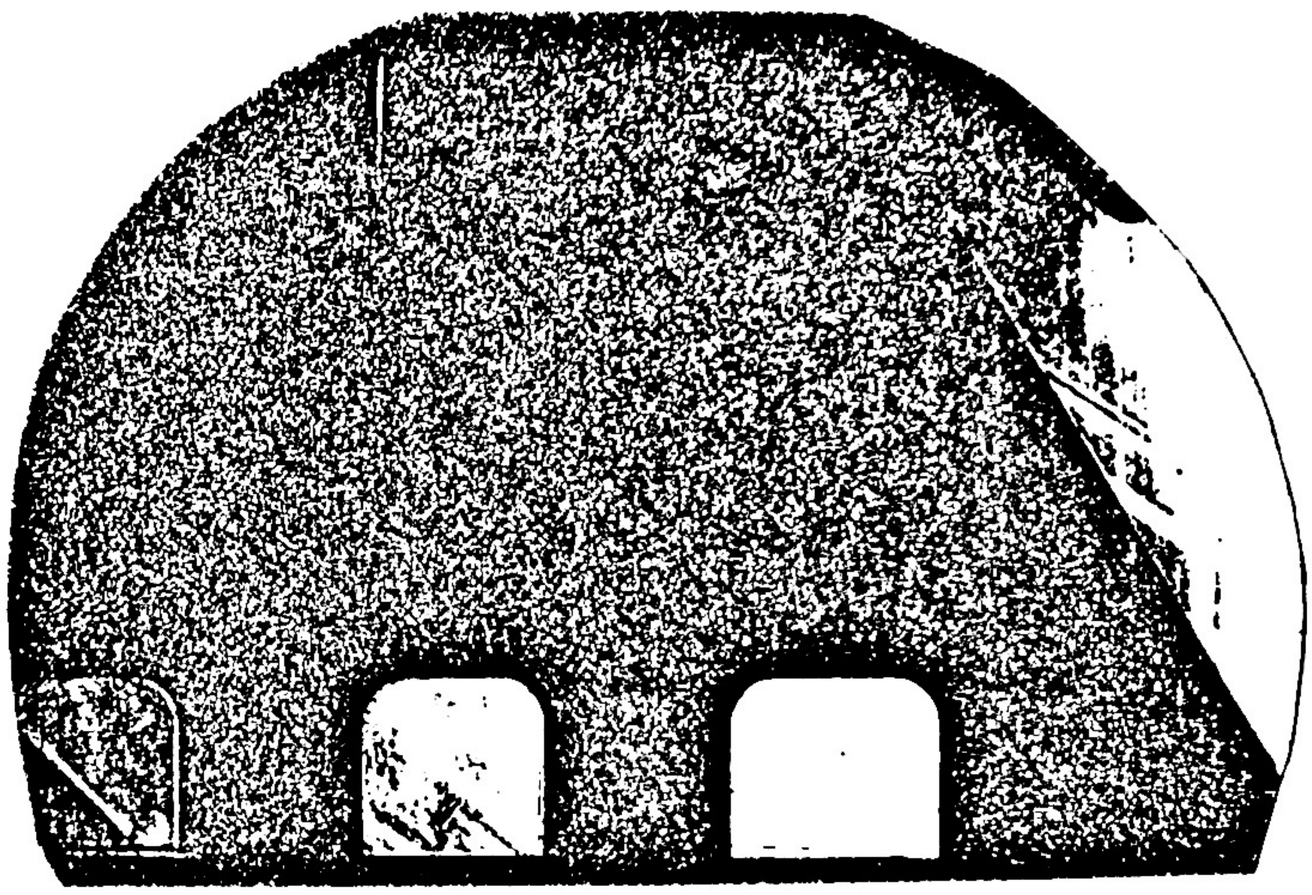


Fig. 8b. Flat plate with fin

Figure 8: Schlieren photographs indicating starting of the tunnel

It is also important to know that the model is positioned in that section of the nozzle designed for uniform Mach number. The nozzle used in S-1 (Ref. 37) was actually designed via Friedrich's method[39]. A correction to Friedrich's method was made for the growth of a laminar boundary layer along the tunnel walls. With some approximations, the method of characteristics may be used to evaluated the different regimes inside such a nozzle.

Assuming an inlet Mach number slightly greater than one (neglecting the effects of the precise location of the sonic line), and prescribing an arbitrary initial curving to the tunnel wall, characteristic lines may be drawn, followed through the flow field (taking into account

interactions with the other characteristic lines), reflected off the symmetry line, and then cancelled at the wall. This gives approximately the nozzle design currently used in S-1, and is useful for the present purpose simply to illustrate that the model is placed in the tunnel in the region designed for conditions of uniform flow.

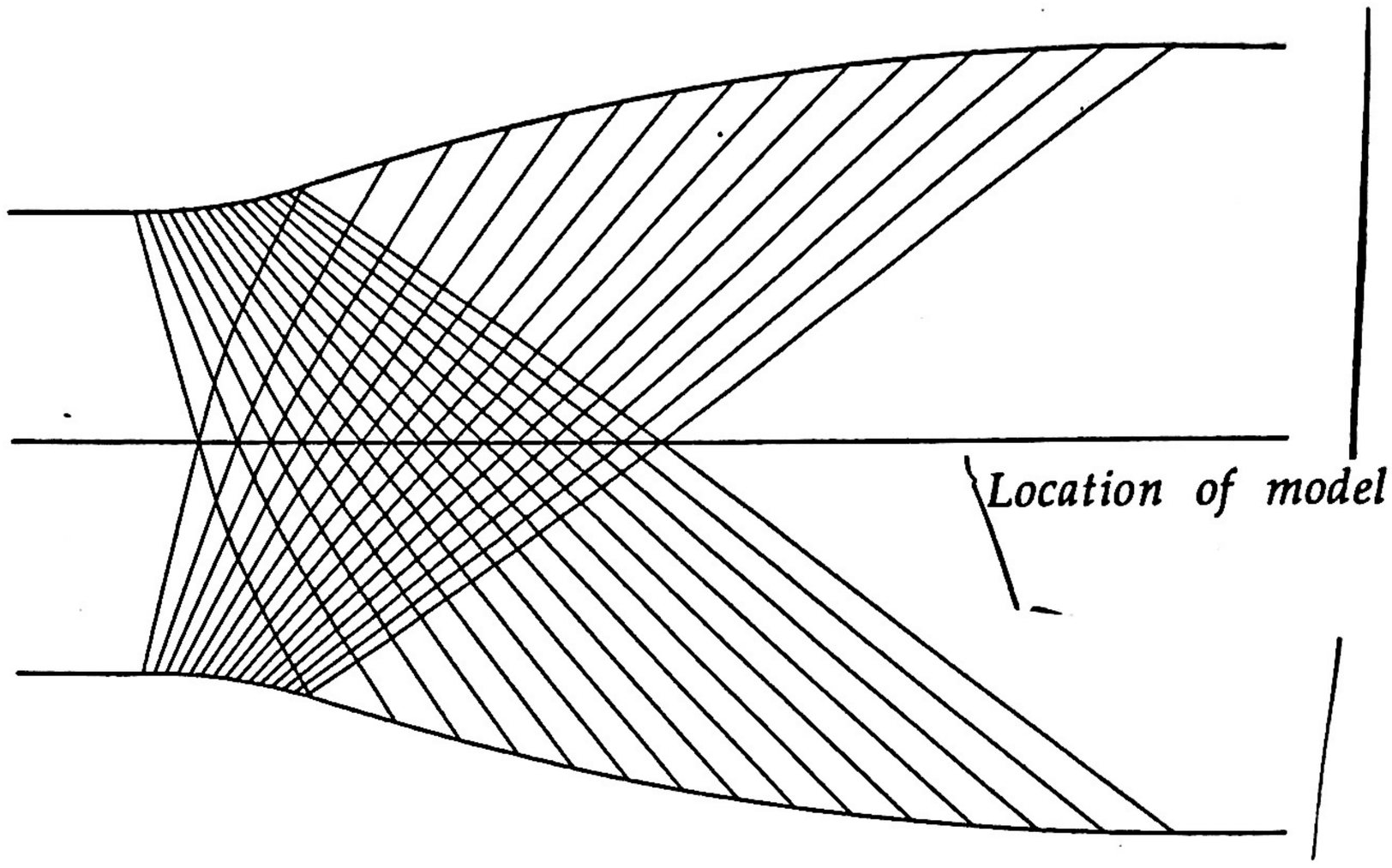


Figure 9: Characteristics plotted in a nozzle similar to that used in S-1.

3.2 Surface Flow Visualizations. The long start up and shut down times of the tunnel S-1 tend to hamper flow visualization using standard methods. Oil solutions applied to a model before a test usually flow too much before Mach 2 flow is established. Solvents added to the oil to set up the visualization before tunnel shut down tend to evaporate during start up. Paint injected during the test (through the surface of the plate using holes drilled for taking pressure measurements) tends to spurt into the very low pressure of the test section and disrupt the flow under consideration.

One method that provides fairly good results is by model injection: the model is covered with an oil (mixed with a powder so streaks can be seen) and stored in a special mechanism outside the tunnel which replaces a tunnel window. After supersonic flow is established (which takes 3-5 minutes after the 40 minutes it takes to pump the entire volume of the closed circuit tunnel to a total pressure of 0.13 atm), the model is pushed into the flow, the oil flow pattern is allowed to set up, the model is pulled back out of the flow, and finally the tunnel is shut down. Only then can the model be removed from the injection chamber and photographed. An example of a visualization by Degrez using this technique is given in figure 10.

There are two drawbacks of the injection method. First, it is difficult to seal the chamber outside the tunnel, so the oil flows even when the model is in this chamber. More important, though, is that, while being pushed the model into the tunnel and while being

pulled out, the model is subjected to a skewed flow and thus the visualization pattern is disturbed to some unknown degree.

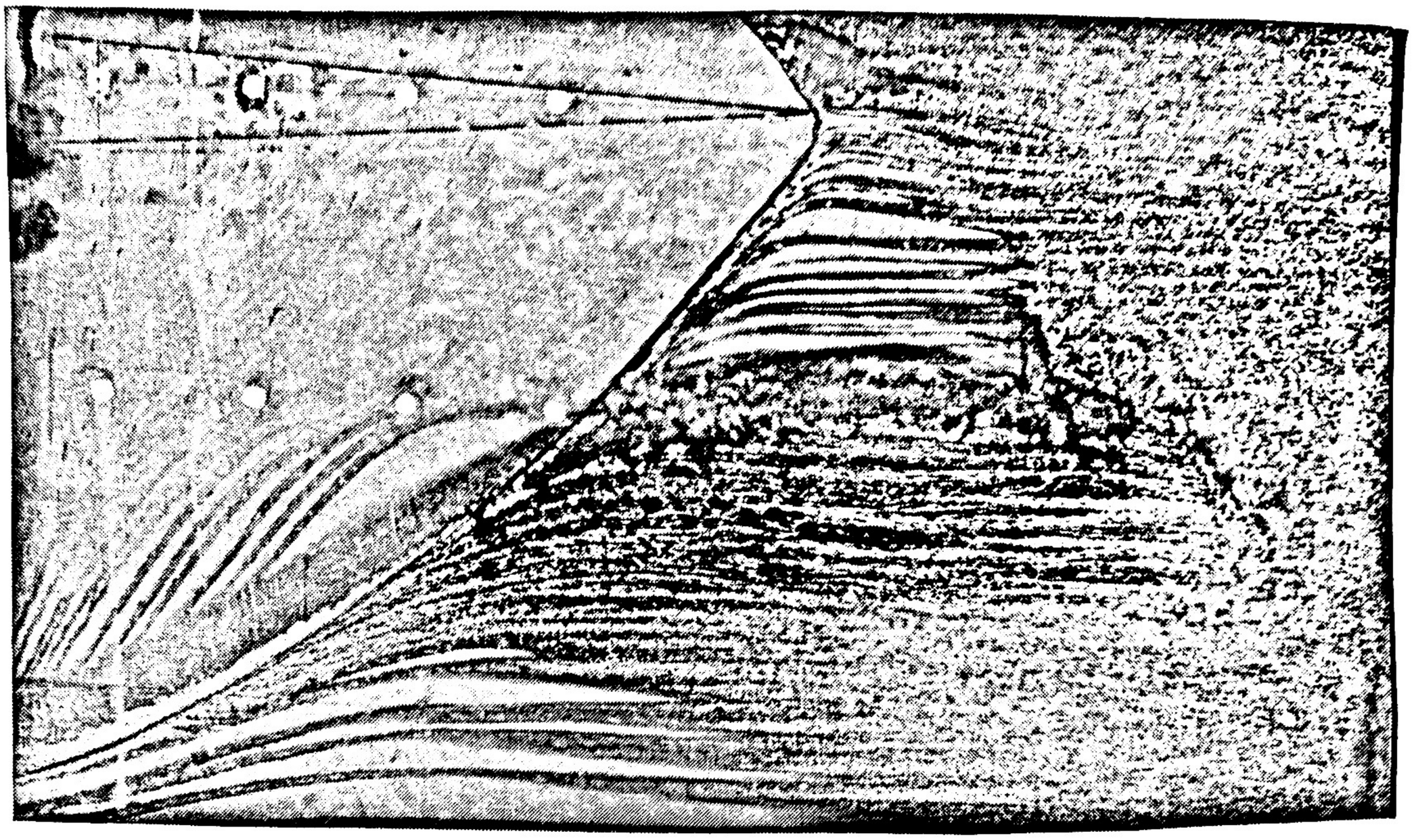


Figure 10: Surface flow visualization via injection of oil covered model.[8]

One technique suggested to improve oil flow visualization under such difficult conditions is to mix the visualization fluid with a liquid which decreases in viscosity dramatically when heated, such as honey. This would be done so that, while in the chamber (at the static temperature) the fluid would not flow, but when in the tunnel (at the recovery temperature) the fluid would flow. This idea has not yet been tried at the VKI.

In the new method of flow visualization, small particles immersed in the boundary layer were glued to the surface of the plate at various locations. Particles about half the boundary layer thickness worked best - in the present case about 1 mm. After applying these particles, a standard sublimation technique was used: a large organic compound called Acenaphthen { $C_{10}H_6$-1,8-CH_2 CH_2 } mixed in Diethyl ether { $(C_2H_5)_2O$ } at a concentration of 40 g/l was sprayed to the surface of the model and allowed to partially sublimate off the model during the test, which took about 30 minutes. The vortical disturbances emanating from the small particles in the boundary layer increased the skin friction, causing a higher sublimation rate and leaving streaks in the sublimation pattern. The disturbances follow the path of the flow, giving a good indication of the direction of the velocity of the flow. Also, regions where such streaks all tend to disappear is indicative of flow separation; the disturbances lift off the plate and no longer affect the sublimation pattern in such regions.

There are many drawbacks to this new method. The method does not provide the high resolution of separation and reattachment lines that an oil flow visualization can. The particles disrupt the boundary layer flow significantly and may cause early transition to turbulence. Unevenness of the coating of the sublimation material causes some patterns to develop faster than others; caution must be used when comparing the magnitude of the disturbances seen in different regions on the plate. Disturbances don't always die out with distance downstream; in fact, some are amplified when local transition is triggered.

With these drawbacks in mind, it may be best to visualize small regions of the model one at a time with this technique. That way, there is always a minimum number of particles disturbing the flow upstream of the point under examination.

The strength of this technique, of course, is that the sublimation pattern is virtually unaffected by the flow during start up and shut down.

In the present experiment, this technique was used to verify the two-dimensionality of the flow over a plate which was used to study fin induced shock-wave boundary layer interactions, as shown in figures 11a and 11b. These figures provide good examples of the strengths and weaknesses of the method as described above.



Figure 11a: Surface flow visualization by disturbance streaks in sublimation pattern.

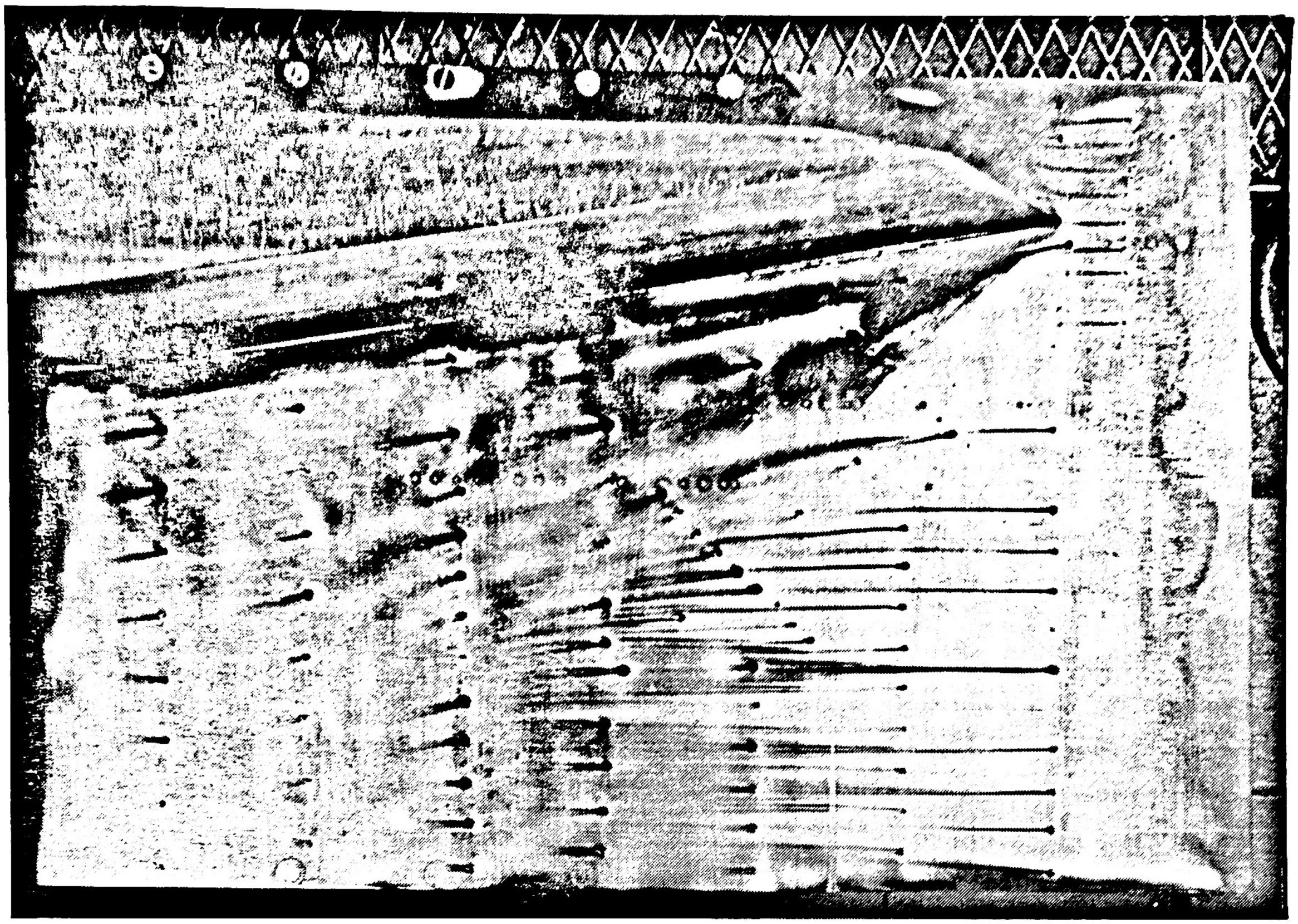


Figure 11b: Surface flow visualization by disturbance streaks in sublimation pattern.

3.3 Flow seeding. It is often recognized that the most difficult part of single component high speed LDV is proper flow seeding. Polystyrene spheres 1 μm in diameter prove to work well for this purpose. These particles are a good choice because they are small and light (so they track the flow well) but are large enough to reflect a significant amount of light. Also, an easy formula for production of these particles developed NASA Langley[26] may be used in any lab.

It is difficult to get the polystyrene particles into the tunnel directly in dry form without conglomeration - the individual particles tend to stick together and form large conglomerates which track the fluid velocity poorly. Thus, a method of injection was chosen which would inject droplets of a solution in which the seed particles were suspended. The droplets need to be small enough, and the injection point far enough upstream, that the carrier liquid evaporates before droplet reaches the probe volume. This leaves the individual particles which were formerly suspended in the solution, without significant particle contact and formation of conglomerates. The system shown in figure 12 was developed for this purpose.

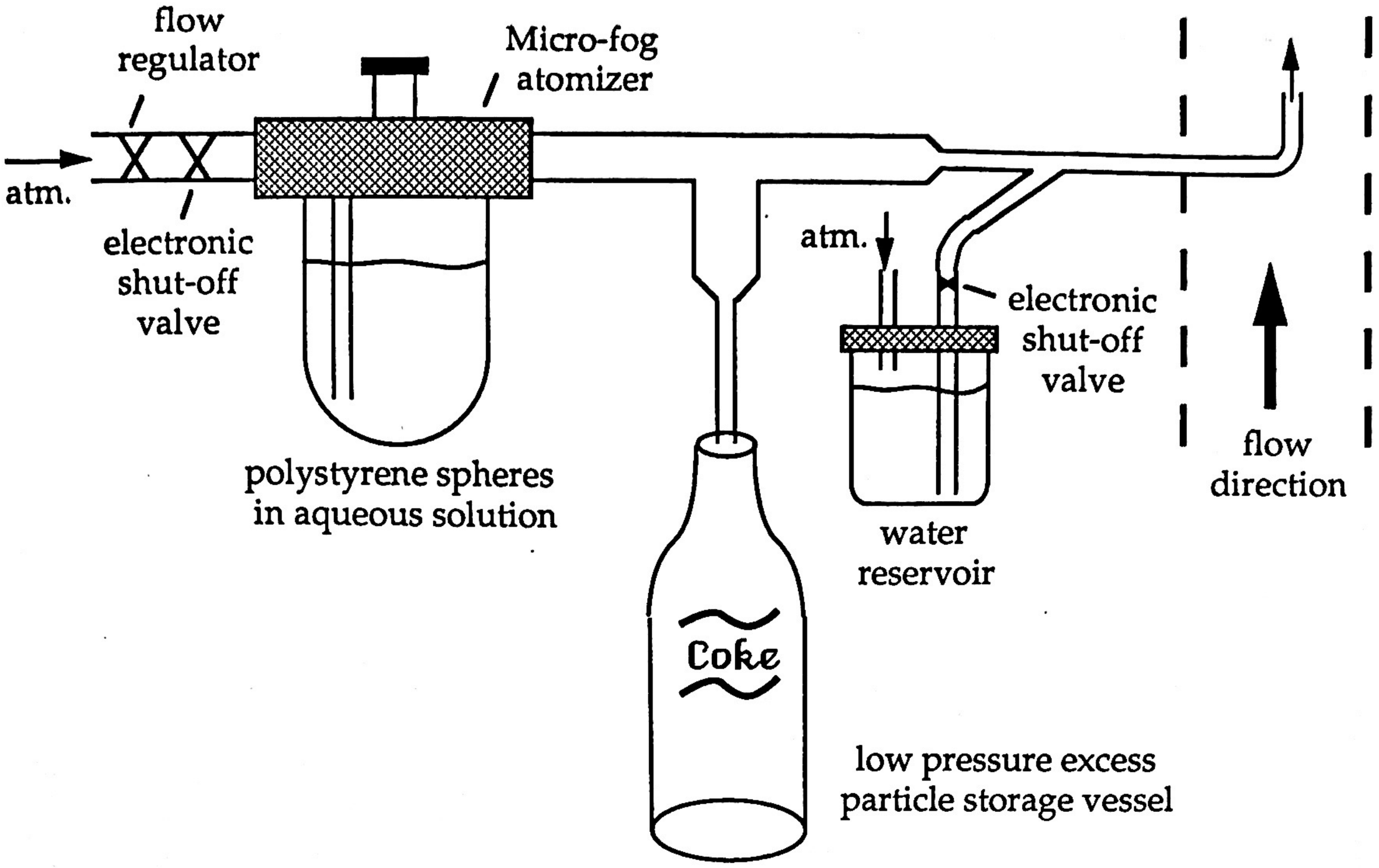


Figure 12: New particle seeding system for LDV

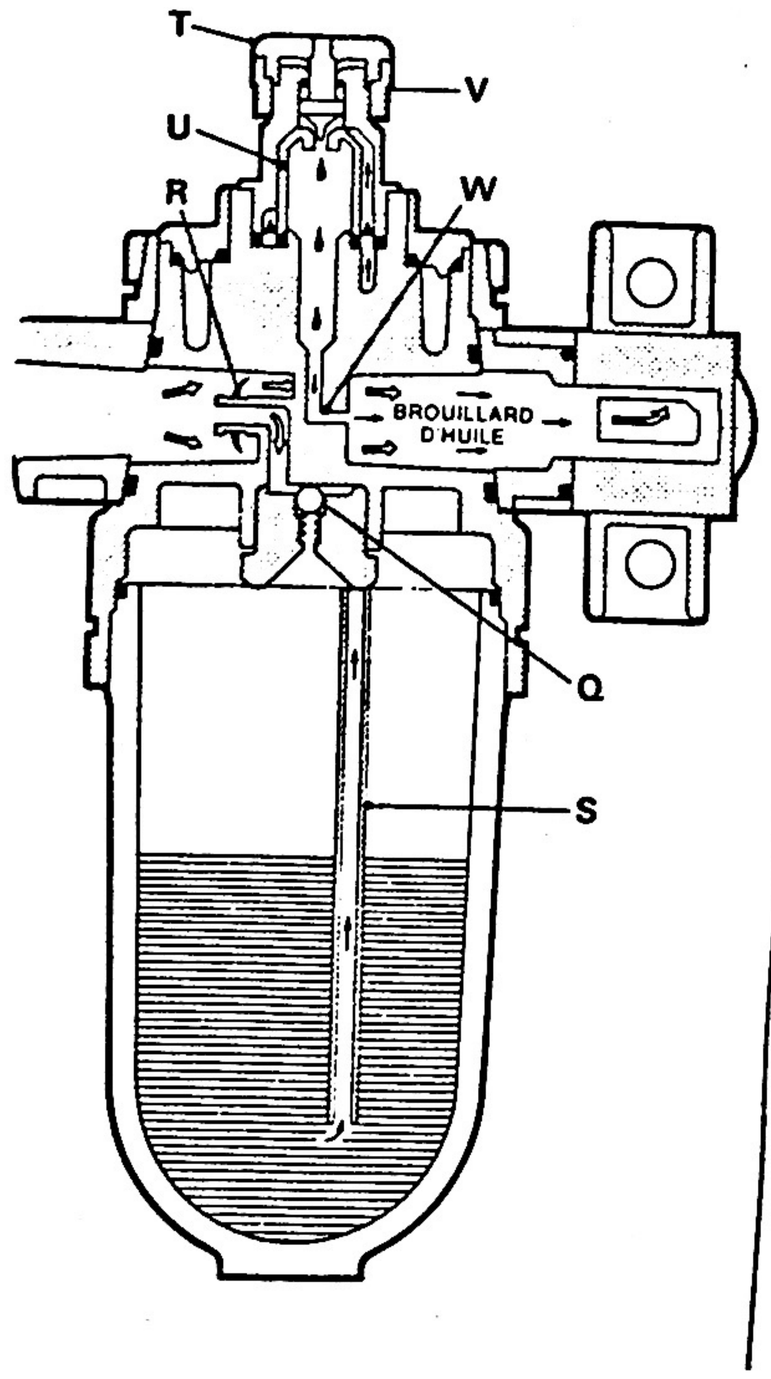


Figure 13: Schematic of the atomizer used in the seeding system

To create the small droplets (~10 μm in diameter), a commercial atomizer was used, driven by the difference in pressure between the atmosphere and the contraction section of the tunnel (at 0.1 atm). The atomizer (Norgren Oil Fog Lubrificateur Model Number L13-000-0PE03, shown in figure 13) occasionally became clogged with the particles. Regulation of the rate of injection by closing or opening the valve regulating the rate of air flow into the atomizer instead of adjusting the flow rate knob of the atomizer itself tended to alleviate this problem. Frequent cleaning of the atomizer and straining of the particles were also important.

An electronic valve was used to activate the particle generator only when measurements were being taken. This was crucial to limit the amount air, water, and particles admitted to the tunnel. This valve was controlled by a momentary contact switch - it was found that the finest mist was achieved by toggling this switch. A drainage hole in the large diameter tube after the atomizer into a pressurized storage vessel was required to remove the large droplets which are also emitted from the atomizer. The liquid collected in this vessel may be reused.

It was found that during a test particles tended to accumulate on the windows in the fin and thus diminish the strength of the forward scatter LDV signals. Particles also built up to a small extent on the plate itself, increasing the roughness slightly and thus disturbing the boundary layer under examination. To alleviate these problems, a commercial product (available at major supermarkets) called Rain-X was used. This product was originally developed for airplanes and is marketed for use on car windshields. When properly used, it fills in the microscopic pores and irregularities on the surface. This keeps water from beading up on the windshield (reducing visibility) and also helps keep dirt and insects from sticking to the glass. In the present situation, it was applied before each test to the windows, the fin, and the plate, and was found to virtually eliminate problems of particle build-up.

One feature of the current system is a mechanism for injection of water in parallel to the particle droplet generation system, as shown in figure 12. A small diameter tube was used to inject the particles into the flow 2 meters upstream of the probe volume in the subsonic region of the tunnel. It was found that these particles did not disperse much in the flow, which was laminar the entire distance. The tube therefore had to be positioned accurately or the particles would not pass through the probe volume. However, the tiny polystyrene particles were very difficult to see even when they passed through the probe volume and thus it was difficult to adjust the position of the injection tube. Use of the parallel water injection system when making such adjustments alleviated this problem.

Faster evaporation could have been obtained by using a solution which was more volatile - for example, by mixing the particle solution with methanol or ethanol. Careful attention to the flash point and the toxicity levels must be made if this is tried in a closed circuit tunnel.

Also, attention must be paid to what liquids the atomizer itself allows, and the deterioration rate of the polystyrene spheres in the liquid.

The rate of evaporation of a droplet may be examined to evaluate the effect of using different liquids. Assuming the particle is at the fluid velocity (where it isn't, the evaporation rate is much higher) and at the conditions of injection (at the test conditions, the evaporation rate is higher) the equations governing droplet evaporation can be used to put an upper limit on the expected lifetime of a small droplet of radius R:

mass diffusivity: $$\mathfrak{D}_{AB} = \frac{a}{p}(p_{cA}\, p_{cB})^{1/3}(T_{cA}\, T_{cB})^{5/12}\left(\frac{1}{M_A}+\frac{1}{M_B}\right)^{1/2}\left(\frac{T}{\sqrt{T_{cA}\, T_{cB}}}\right)^{b}$$ *units of cm²/sec*

mass transfer coefficient: $$k_{xM} = \frac{c_f \mathfrak{D}_{AB}}{R}$$ *units of g-mole / sec / cm²*

Evaporation rate: $$\mathfrak{w}_A^{(m)} = k_{xM}\, 4\pi R^2 \frac{x_{AD}}{1 - x_{AD}}$$ *units of g-mole / sec*

rate of decrease in radius of droplet: $$\frac{\partial R}{\partial t} = \frac{\mathfrak{w}_A^{(m)} M}{4\pi R^2}$$ *units of cm / sec*

where $c_f = \rho_{air} / M_{air}$; x_{AD} is the vapor pressure of the liquid; $a=3.64\times10^{-4}$, $b=2.334$ for water with air, and $a=2.75\times10^{-4}$, $b=1.823$ for nonpolar gasses with air. Although methanol and ethanol are polar gases, these constants are used here for a rough approximation. The other constants for the gases used are:

	T_c (° K)	P_c (atm)	M (g/g-mole)
methanol	513	78.5	32.04
ethanol	516	63	46.07
dry air	132	36.4	28.97
water	647	218	18.02

From these values, at a droplet radius of 5 μm and an air pressure of 0.1 atm and air temperature of 286° K and air pressure of 1.2×10^{-4} g/cm³, the rate of decrease of droplet radius can be evaluated using the above formulae. At these conditions, the vapor pressure of water is 0.025 atm, and the vapor pressure of methanol and ethanol are about 0.08 atm. The following rates are therefore calculated:

	water in air	ethanol in air	methanol in air
$\mathfrak{D}_{AB}$	2.4	1.0	1.2
k_{xM}	0.020	0.0082	0.010
$w_A^{(m)}$	1.6e-9	2.2e-9	2.7e-9
$\partial R/\partial t$	0.009	0.032	0.027
expected life	0.05 seconds	0.015 sec	0.018 sec

Thus, we see that methanol and ethanol droplets evaporate approximately three times faster than water droplets. So many approximations were used in arriving at the expected lifetime of droplets computed above that these numbers should be used for comparison only. For a more accurate estimation of water droplet life, a much more complicated calculation must be done.

Due to the acceptable evaporation rate shown above and the known capability of the tunnel to remove water from the circuit, water was chosen as the carrier liquid for the particles. Also, since the particles are actually prepared in a water solution, this eliminates the need for drying, which is suspected to be a major source of the particle conglomeration problem. Perhaps the droplets could be made to evaporate faster by mixing the aqueous particle solution with one of these alcohols.

3.4 Preliminary results and analysis. Surface flow visualization via the new technique (figure 11) confirmed that the flow under study is undisturbed by edge effects. Thus, the skewed visualization lines near the edge of the plate opposite the fin in Degrez's visualization (figure 10) are dismissed as artifacts of the tunnel start up and shut down and model injection processes. However, the distinctly curved shape of the separation line seen in Degrez's visualizations, which probably could not be caused by these effects, are evidence for a interaction region growth rate proportional to the (parabolic) boundary layer growth rate. Surface flow visualization also confirmed that no significant information about the removal of part of the model and the proximity of the tunnel wall was transmitted through the subsonic part of the boundary layer in front of the model, as the surface streamlines were symmetric about the plane y=0.

The LDV measurements were not quite as successful. A comprehensive set of 340 velocity histograms were taken at different points in one cross flow plane. This velocity survey was completed before several of the improvements in the seeding system shown in figure 12 were made. This data was very difficult to interpret. Below are examples of four of these histograms of velocity measurements:

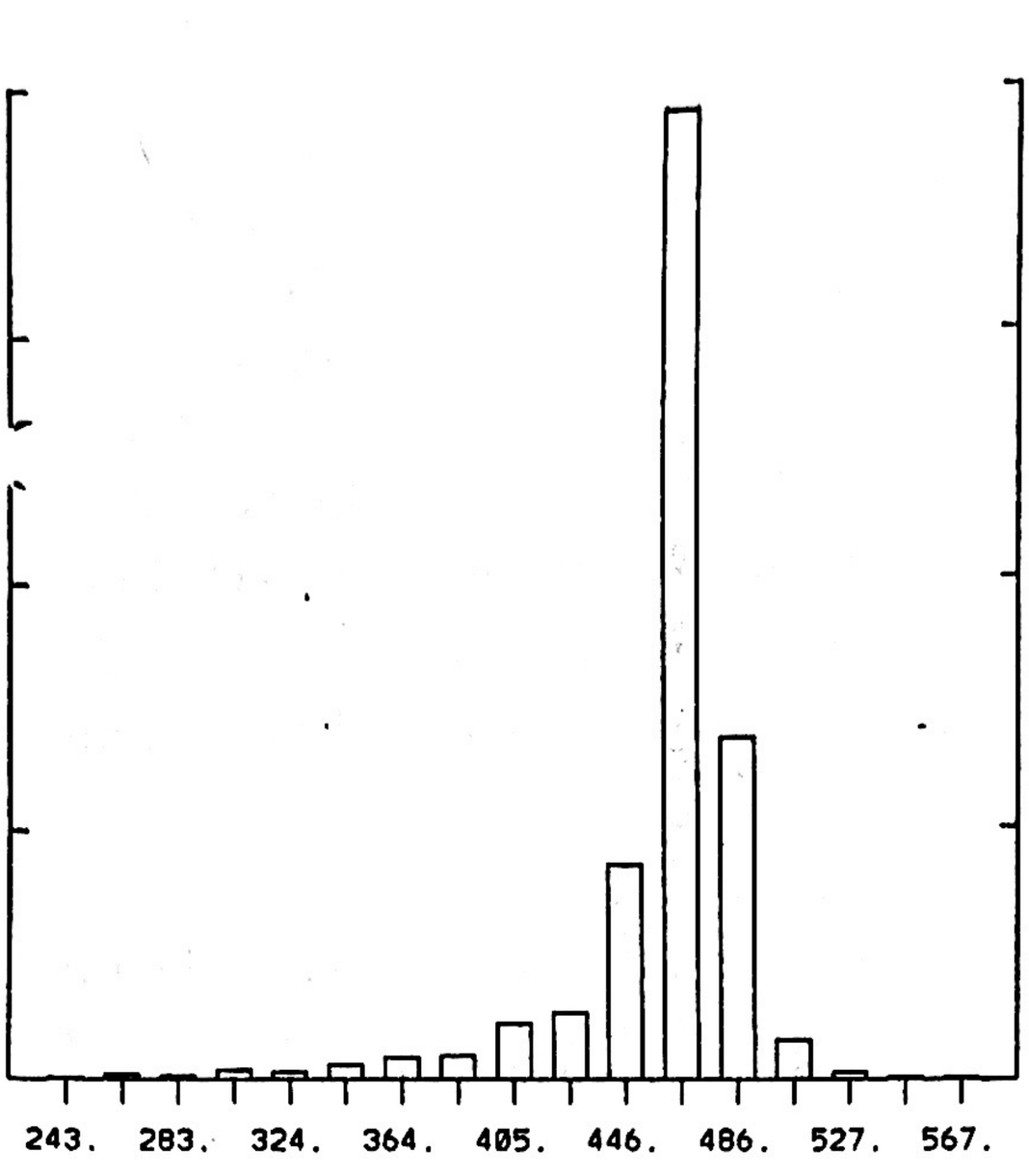


Fig. 14a. In the Free Stream

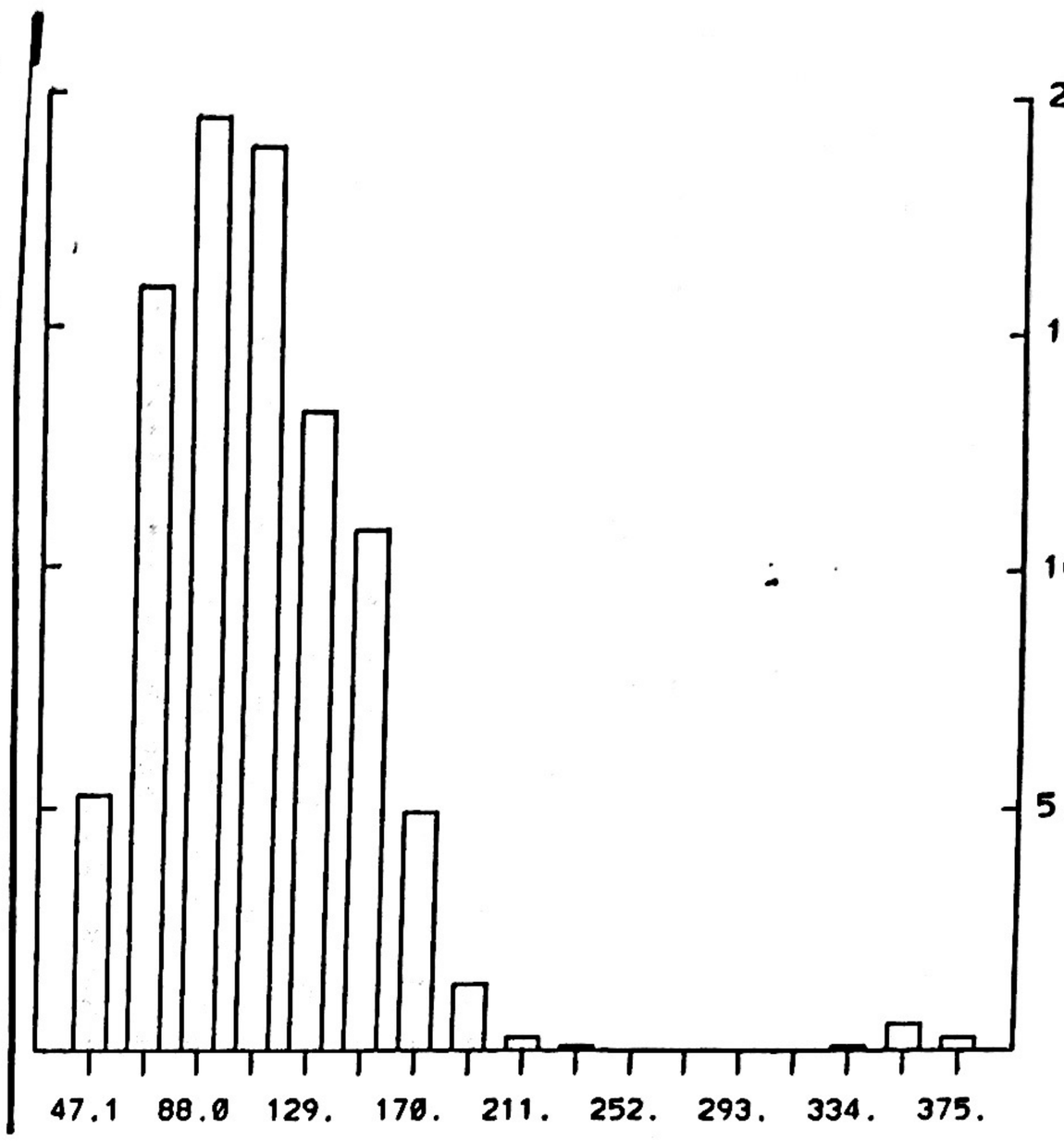


Fig. 14b.. Very near the wall

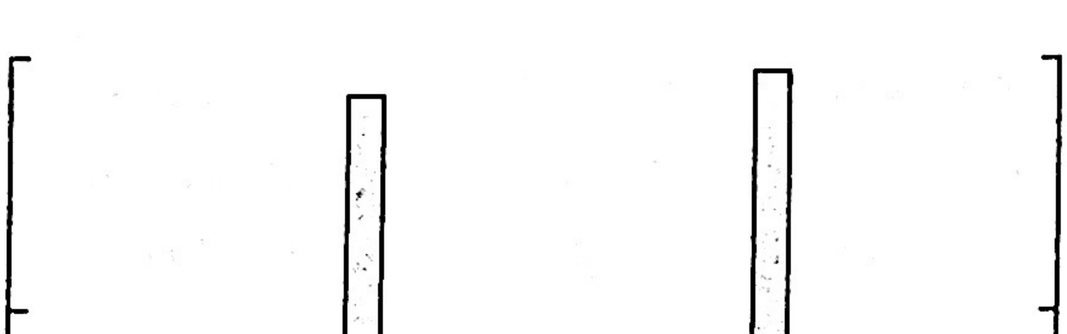


Fig. 14c. In the region of maximum deceleration

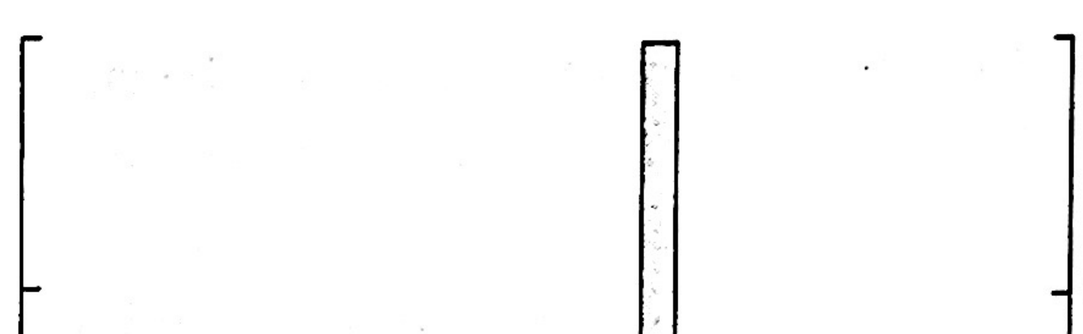


Fig. 14d. Ambiguous profile in the interaction region

Figure 14: Sample histograms of velocity measurements.

Abscissa is velocity in m/s, ordinate is percent occurrence in that category.

A discussion of the deceleration in the boundary layer using the model of Chapman and Rubesin is instructive at this point, because this approximation of a compressible boundary layer accurately models the undisturbed section of the boundary layer under consideration. As it progresses downstream on the plate, the boundary layer thickness increases at a rate of $x^{1/2}$. "Fresh" fluid at the free stream velocity enters at the top of the boundary layer and is decelerated. In fact, the fluid is decelerating everywhere in the boundary layer, as is shown below.

The Chapman and Rubesin solution of a compressible boundary layer is:

$$\frac{U}{U_\infty} = \frac{f'(\eta)}{2}$$

and

$$\frac{T}{T_\infty} = 1 + \frac{\gamma - 1}{2} M_\infty^2 \, r(\eta) + \frac{T_w - T_r}{T_\infty} Y_o(\eta)$$

where

$$\frac{y}{2}\sqrt{\frac{U_\infty}{\nu_\infty x C}} = \eta + \frac{\gamma - 1}{2} M_\infty^2 \, \bar{r}(\eta) + \frac{T_w - T_r}{T_\infty} \overline{Y_o}(\eta)$$

and

$$\bar{r}(\eta) = \int_0^\eta r(\eta)\, d\eta \quad \textit{and} \quad \overline{Y_o}(\eta) = \int_0^\eta Y_o(\eta)\, d\eta$$

and f, r, and Y_o are the solutions to the following ordinary differential equations obtained from the momentum and energy equations:

$$f \cdot f'' + f''' = 0$$
$$\textit{with } f(0) = f'(0) = 0 \textit{ and } f''(\infty) = 0$$

$$r'' + Pr \cdot f \cdot r' + \frac{Pr}{2}(f')^2 = 0$$
$$\textit{with } r'(0) = 0 \textit{ and } r(\infty) = 0$$

$$Y_o'' + Pr \cdot f \cdot Y_o' = 0$$
$$\textit{with } Y_o'(0) = 1 \textit{ and } Y_o(\infty) = 0$$

where Pr is the Prandtl number, ν is the kinematic viscosity, γ is the ratio of specific heats, and M is the Mach number. The numerical solution of these equations was computed and is tabulated in appendix 5.

Note that one particular solution of these equations (with $M=0$ and $T_w = T_r$) is the Blasius boundary layer.

Differentiation of the equation for the streamwise component of velocity with respect to x eventually leads to,

$$\frac{\partial U}{\partial x}(\eta) = -\frac{U_\infty f'''(\eta)}{8} \frac{\left[\eta + \frac{\gamma - 1}{2} M_\infty^2 \bar{r}(\eta) + \frac{T_w - T_r}{T_\infty} \overline{Y_o}(\eta)\right]}{\left[1 + \frac{\gamma - 1}{2} M_\infty^2 r(\eta) + \frac{T_w - T_r}{T_\infty} Y_o(\eta)\right]}$$

Note that $U \sim f'$ and $\partial U/\partial x \sim f'' * \eta$. For the Blasius boundary layer, $y \sim \eta$. For $M > 0$ or $T \neq T_r$, the profiles as a function of y are slightly stretched variations of the profiles as a function of η. The shapes of the velocity and deceleration profiles are plotted below as functions of η:

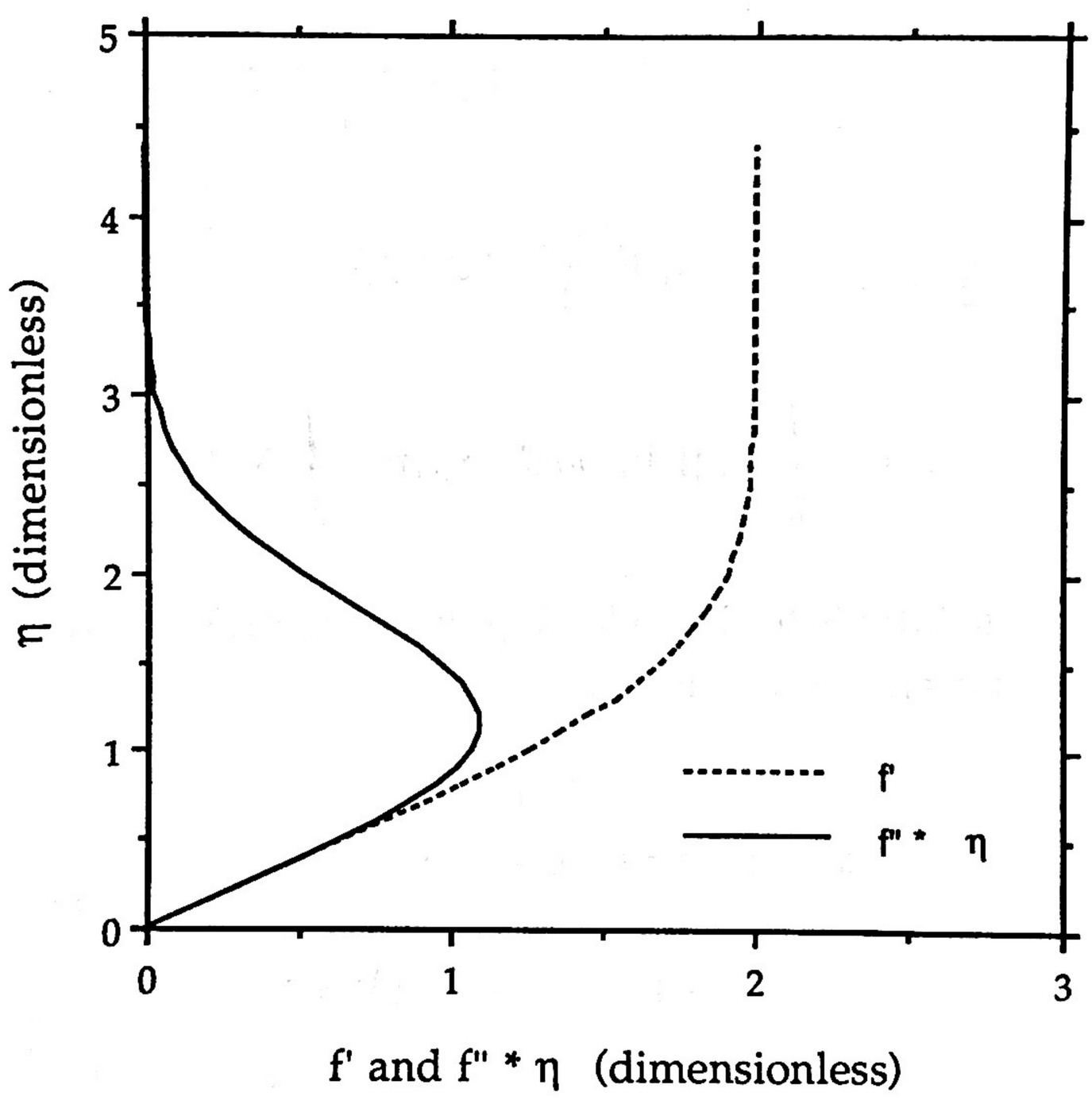


Figure 15: Comparison of velocity (~ f′) and deceleration (~ f″η) profiles for the Chapman & Rubesin boundary layer.

The level of maximum deceleration in the boundary layer is seen from figure 15 to be approximately one half the boundary layer thickness. The ratio of the height of the point of maximum deceleration to the thickness of the boundary layer increases slightly with Mach number and wall temperature, as can be seen by applying numerical solutions of the variables f, r, and Y_o to the equations above. This level of maximum deceleration was found to precisely coincide with the level of maximum signal splitting shown in figure 14c. It follows that the flow seeding consisted of two sizes of particles: single polystyrene spheres and large conglomerations of spheres or droplets of water.

Each velocity histogram must be analyzed individually to pick out the peak corresponding to the smallest particles in order to make the most accurate evaluation of the measurements. This is easy in the double peaked case shown above for a non-interacting boundary layer; the boundary layer is always decelerating so the correct peak is the one corresponding to the lower velocity. However, when such peaks overlap, when the lower velocity peak is not distinct, and in the interaction region where a complicated flow pattern exists, it is not always possible to make such a straight-forward analysis. With these limitations in mind, calculated profiles of the first velocity survey (before several of the modifications shown in figure 12) using this technique are shown below.

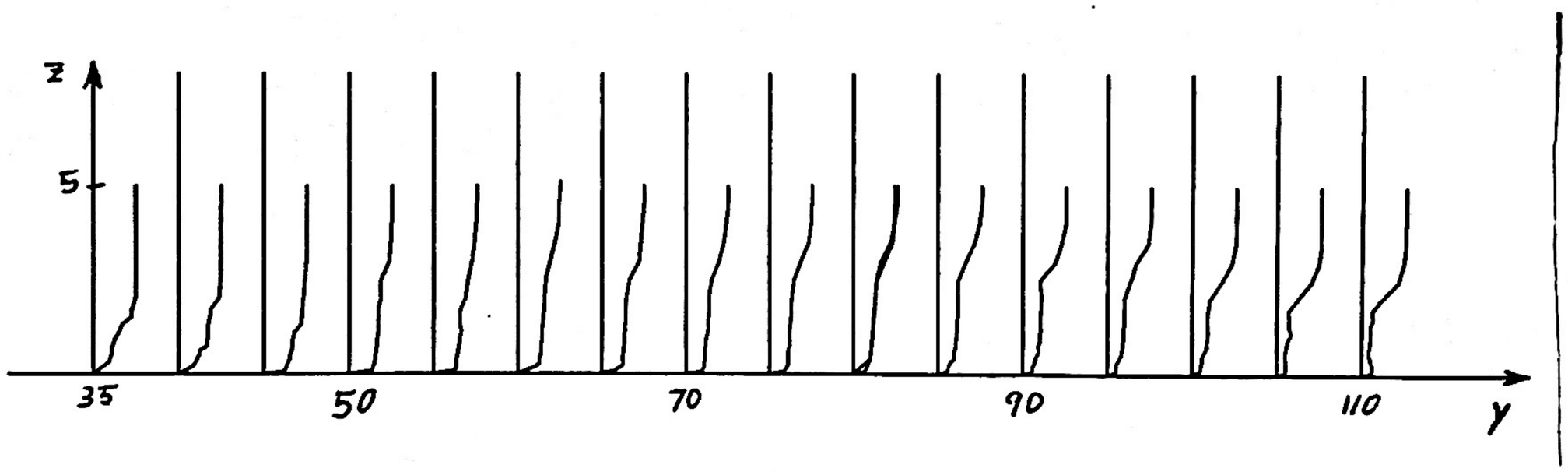


Figure 16: Streamwise boundary layer velocity profiles obtained by analysis of histograms obtained in the cross flow plane at x=109 mm for α=10°, θ=60°.

A much easier method of analyzing distribution of particle sizes is by measuring LDV signals behind a shock, through which the velocity makes a step in magnitude and direction. Of course, the analysis would be most straight forward by examining a normal shock. However, it is very difficult to set up a stable normal shock in a wind tunnel. The change of velocity direction through an oblique shock presents only a slight complication. An analysis of the effect of an oblique shock on a velocity of the LDV particles is made in Ref. [29].

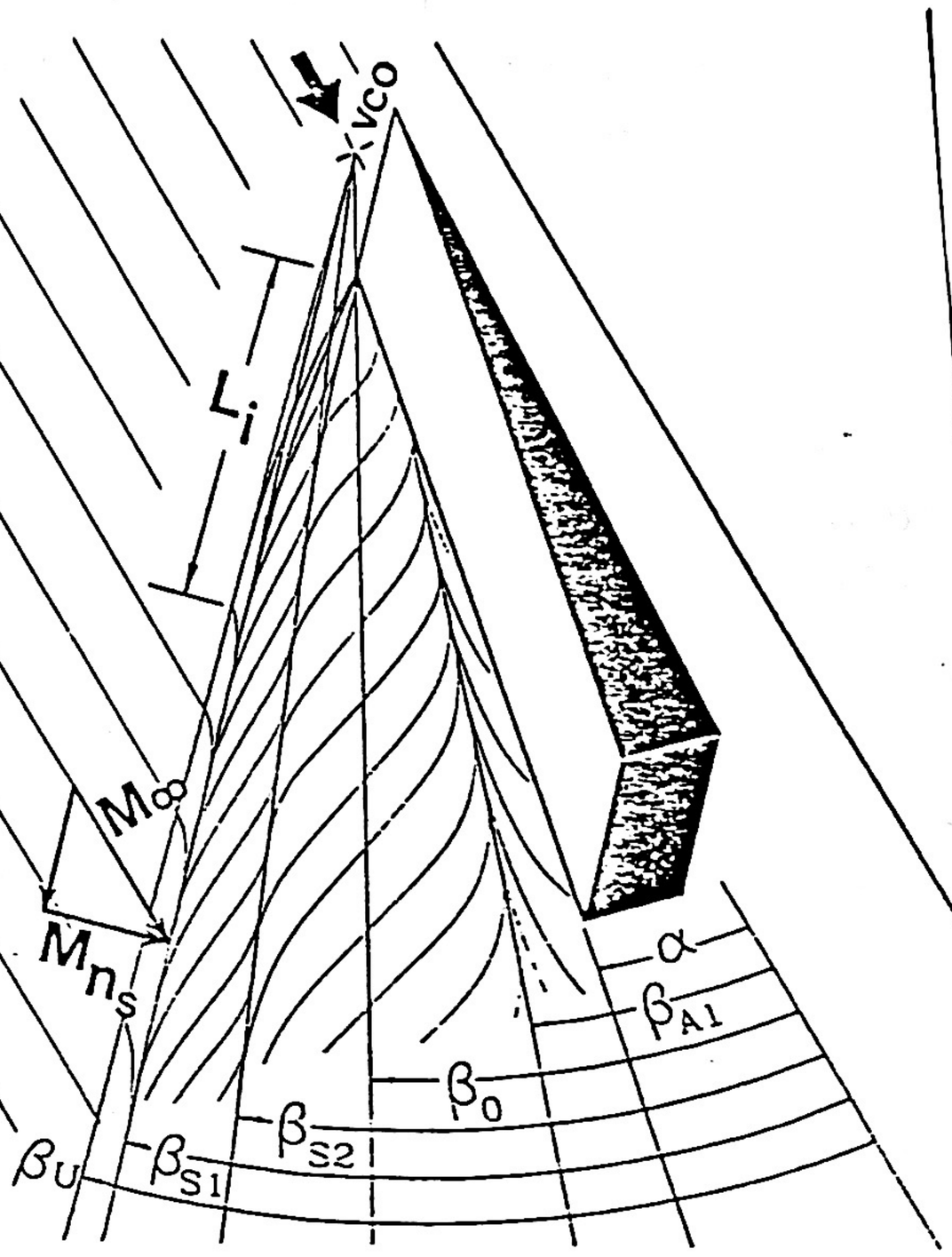


Fig. 17a. Sketch of proposed symmetry model for interaction footprint

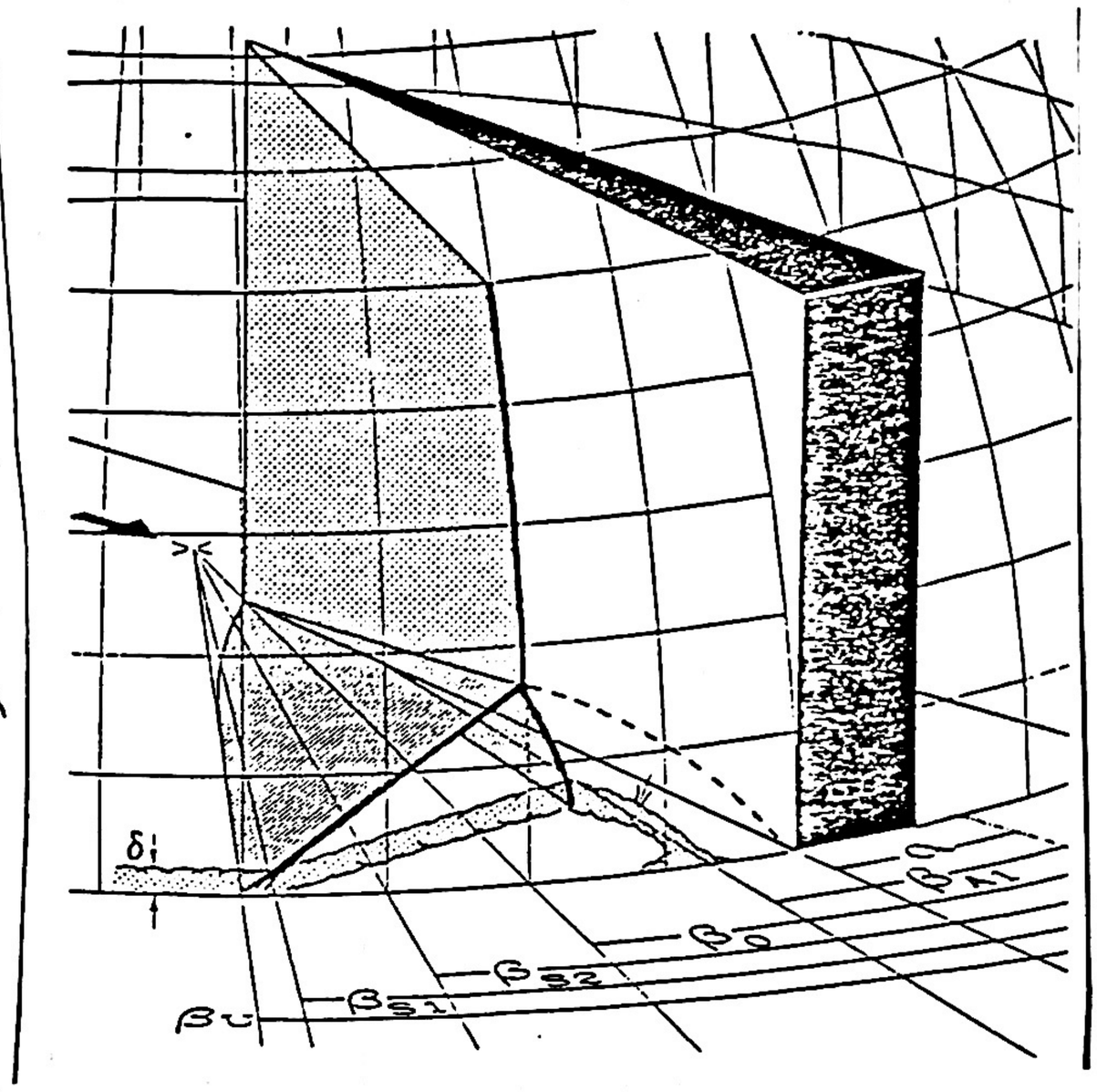


Fig. 17b. Three dimensional representation of figures 17a and 17d

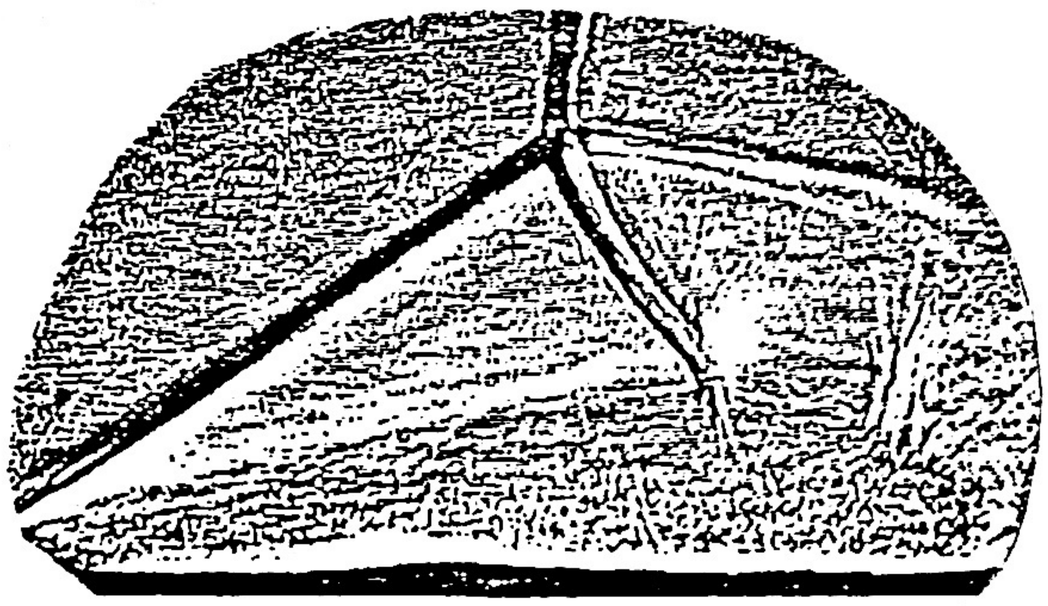


Fig. 17c. Conical shadowgram of Mach 3, α=20° interaction flowfield

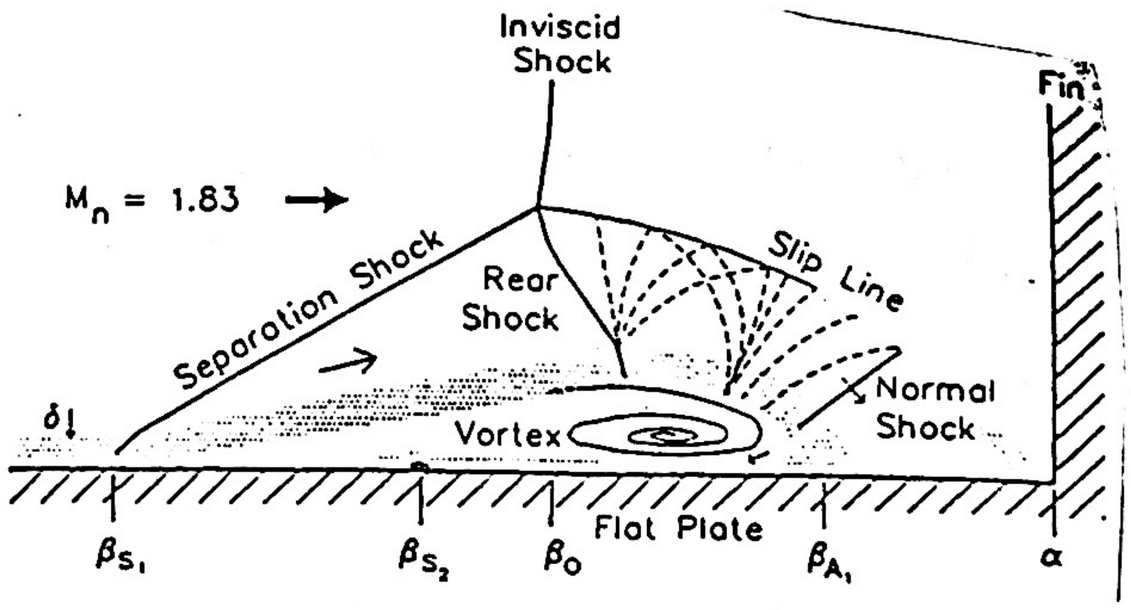


Fig. 17d. Diagram of flowfield structure of figure 17c

Figure 17: Model of three dimensional structure of the normal fin induced shock wave/turbulent boundary layer interaction proposed by Settles et. al.[7]

Results from figure 16 look qualitatively quite good. The model is to the left, and the calculated location of the inviscid shock is y ≈ 70 mm. This location corresponds approximately with the maximum thickness of the separation region. A surprising result is the extent of the interaction outside of the shock (to the right). Comparison to results from the study of the interaction with a turbulent boundary layer[7], which should be similar, was made. A large separation shock was expected from this comparison (figure 17), but since accurate surface flow visualizations were not available, the extent of the separation was estimated. Clearly, the separation region extends further to the right than the last profile measured. Also surprising is the clarity of definition of the separation shock (see figure 17d) in this region. It is rather disappointing that the streamwise component of the velocity is not a sensitive enough parameter to distinguish the characteristics of the flow in the "vortex" region predicted in figure 17d.

Note that two profiles (from two separate sets of histograms, taken on different days) at location y=80 mm almost exactly overlap, indicating excellent repeatability of the measurements. Although the velocity histograms themselves are repeatable, the value of the velocity given by analysis of these histograms is quite sensitive to the method of analysis. A modification of the set-up used for these tests is required before measurements of benchmark quality can be claimed. It is hoped that the improvements shown in figure 12 will provide this quality of result. This disclaimer is further reinforced by the two profiles shown below at stations y=95 and y=100. At each station, both profiles were made from the same histogram; one used the method of analysis of the double peaks described above, the other used straight averaging of all signals corresponding to velocities between 0 and 550 m/s. Significant deviation is seen in the regions of large flow deceleration.

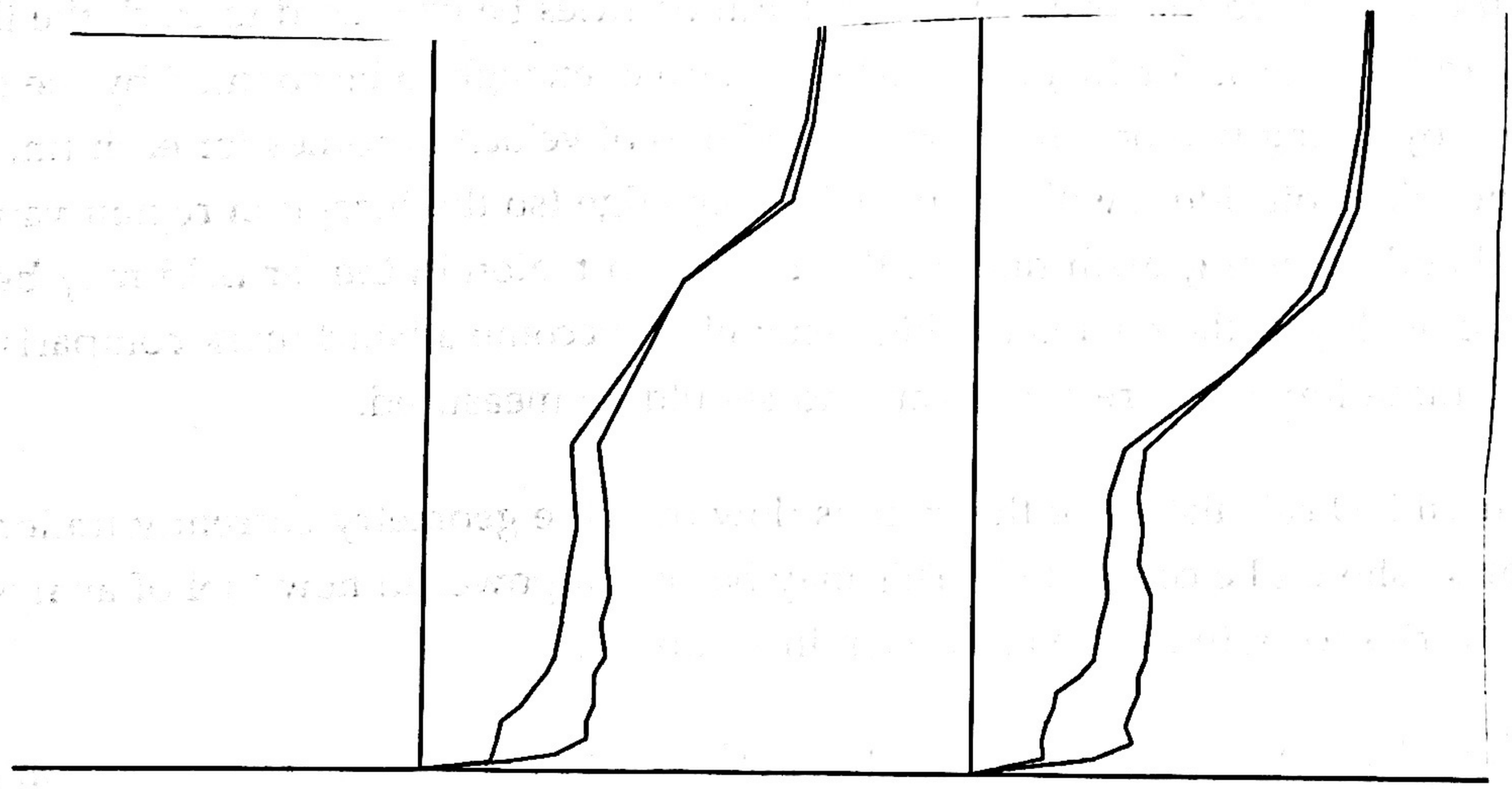


Figure 18: Comparison of methods for evaluating velocity histograms.

Chapter 5 - Conclusions and Future Projects

At this point, an equation relating the influence of parameters 1 - 3 discussed on page 1 still can not be formulated. However, significant progress has been made in that direction.

Important features of the inviscid flow over swept fins and compression corners have been thoroughly studied both analytically and numerically. A powerful numerical grid generation technique has been developed for the study of this problem and many others. A parametric set of models have been designed and constructed for the study of the problem in question. A new seeding system has been developed for S-1. A new surface flow visualization technique has been developed with excellent results, confirming undisturbed two-dimensionality of the flow over the flat plate in S-1. Preliminary LDV results have shown that the current set-up has the resolution to at least reveal the growth rate of the separation region in the horizontal and vertical directions. (For a more complete list of items addressed in this report, see Chapter 1.)

The following activities should be completed in near future:

1.) A series of oil flow visualizations using injection models in S-1 should be completed. By centering the model on the plate to be injected and comparing the flow pattern on each side, ill effects due to model injection should be easily quantified.

2.) Velocity surveys with the new particle seeding system shown in figure 12 should be made. Low settings of the amplitude limiter function on the signal processor should be attempted. Further, it is suggested that even smaller, 0.6 μm particles be produced to track the flow better as it appears the signals for 1.0 μm particles are strong enough to be counted by the signal processor. By taking two or three cross-flow planes of velocity profiles for each fin, with the fin leading edge coincident with the plate leading edge (so the inception region vanishes), the horizontal and vertical growth rates of the interaction region in the far field may be found. Even if the quality of the data is not high enough to become a benchmark comparison for numerics, these important relations can and should be measured.

3.) A conical 2-D calculation of the viscous flow over the geometry currently under investigation should be completed. This may become a powerful new tool of analysis if it is found to work successfully (see discussion in section 2.3).

4.) A fully 3-D, laminar, viscous computation should be made that extends well into the far field over the geometry currently under investigation. The final results of the current LDV

measurements should provide an excellent benchmark for this calculation. From there, the symmetry of the interaction should become evident. It is suggested that a grid with conical symmetry in the far field be used, which will solve the inviscid flow there quite accurately. The present grid, scaled with the height of the model at a series of downstream locations, should serve this purpose quite nicely.

It is of critical importance to know how interactions scale with distance, because the experiments done in any lab are on a much smaller scale than the actual flight conditions seen, for example, by a re-entry vehicle. In order to extrapolate the far field results of a turbulent test to the expected conditions 32 times farther away from the leading edge (a very useful thing to be able to do), a linear interaction growth rate approximation overestimates the magnitude of the interaction region given by an $x^{4/5}$ growth rate by a factor of 2. The effect is even more pronounced in the laminar case: at this distance, the linear interaction grown rate overestimates the magnitude of the interaction region given an $x^{1/2}$ growth rate by a factor of 6. More important effects, such as heat transfer, can also be expected to be off by a similar amount if the wrong approximation is used. Therefore, it is imperative that these interaction growth rates be determined correctly.

Appendix 1 - Conical Formulations of the Euler Equations

The steady conservative forms of the Euler equations (conservation of mass, x-momentum, y-momentum, z-momentum, and energy) in Cartesian coordinates are:

$$\frac{\partial}{\partial x}(\rho v_x) + \frac{\partial}{\partial y}(\rho v_y) + \frac{\partial}{\partial z}(\rho v_z) = 0$$

$$\rho\left(v_x \frac{\partial v_x}{\partial x} + v_y \frac{\partial v_x}{\partial y} + v_z \frac{\partial v_x}{\partial z}\right) = -\frac{\partial p}{\partial x}$$

$$\rho\left(v_x \frac{\partial v_y}{\partial x} + v_y \frac{\partial v_y}{\partial y} + v_z \frac{\partial v_y}{\partial z}\right) = -\frac{\partial p}{\partial y}$$

$$\rho\left(v_x \frac{\partial v_z}{\partial x} + v_y \frac{\partial v_z}{\partial y} + v_z \frac{\partial v_z}{\partial z}\right) = -\frac{\partial p}{\partial z}$$

$$\left(\frac{2\gamma}{\gamma - 1}\right)\frac{p}{\rho} + v_x^2 + v_y^2 + v_z^2 = \text{const}$$

The conservative forms of the Euler equations in spherical coordinates are:

$$\frac{1}{r^2}\frac{\partial}{\partial r}(\rho r^2 v_r) + \frac{1}{r \sin\theta}\frac{\partial}{\partial \theta}(\rho v_\theta \sin\theta) + \frac{1}{r \sin\theta}\frac{\partial}{\partial \phi}(\rho v_\phi) = 0$$

$$\rho\left(v_r \frac{\partial v_r}{\partial r} + \frac{v_\theta}{r}\frac{\partial v_r}{\partial \theta} + \frac{v_\phi}{r \sin\theta}\frac{\partial v_r}{\partial \phi} - \frac{v_\theta^2 + v_\phi^2}{r}\right) = -\frac{\partial p}{\partial r}$$

$$\rho\left(v_r \frac{\partial v_\theta}{\partial r} + \frac{v_\theta}{r}\frac{\partial v_\theta}{\partial \theta} + \frac{v_\phi}{r \sin\theta}\frac{\partial v_\theta}{\partial \phi} + \frac{v_r v_\theta}{r} - \frac{v_\phi^2 \cot\theta}{r}\right) = -\frac{1}{r}\frac{\partial p}{\partial \theta}$$

$$\rho\left(v_r \frac{\partial v_\phi}{\partial r} + \frac{v_\theta}{r}\frac{\partial v_\phi}{\partial \theta} + \frac{v_\phi}{r \sin\theta}\frac{\partial v_\phi}{\partial \phi} + \frac{v_\phi v_r}{r} - \frac{v_\theta v_\phi \cot\theta}{r}\right) = -\frac{1}{r \sin\theta}\frac{\partial p}{\partial \phi}$$

$$\left(\frac{2\gamma}{\gamma - 1}\right)\frac{p}{\rho} + v_\theta^2 + v_\phi^2 + v_r^2 = \text{const}$$

The conical-flow condition that all derivatives with respect to **r** must vanish leads to, in spherical coordinates,

$$\frac{\partial}{\partial\theta}(\rho v_\theta \sin\theta) + \frac{\partial}{\partial\phi}(\rho v_\phi) = 0$$

$$v_\theta \frac{\partial v_r}{\partial\theta} + \frac{v_\phi}{\sin\theta}\frac{\partial v_r}{\partial\phi} - v_\theta^2 + v_\phi^2 = 0$$

$$v_\theta \frac{\partial v_\theta}{\partial\theta} + \frac{v_\phi}{\sin\theta}\frac{\partial v_\theta}{\partial\phi} + v_r v_\theta - v_\phi^2 \cot\theta = -\frac{1}{\rho}\frac{\partial p}{\partial\theta}$$

$$v_\theta \frac{\partial v_\phi}{\partial\theta} + \frac{v_\phi}{\sin\theta}\frac{\partial v_\phi}{\partial\phi} + v_\phi v_r - v_\theta v_\phi \cot\theta = -\frac{1}{\rho\sin\theta}\frac{\partial p}{\partial\phi}$$

$$\left(\frac{2\gamma}{\gamma-1}\right)\frac{p}{\rho} + v_\theta^2 + v_\phi^2 + v_r^2 = \text{const}$$

By applying the condition derived in section 2.3, the conical formulation of the Euler equations in Cartesian coordinates are:

$$\frac{\partial}{\partial y}(\rho v_y) - y\frac{\partial}{\partial y}(\rho v_x) + \frac{\partial}{\partial z}(\rho v_z) - z\frac{\partial}{\partial z}(\rho v_x) = 0$$

$$\rho\left[v_x\left(-y\frac{\partial v_x}{\partial y} - z\frac{\partial v_x}{\partial z}\right) + v_y\frac{\partial v_x}{\partial y} + v_z\frac{\partial v_x}{\partial z}\right] = y\frac{\partial p}{\partial y} + z\frac{\partial p}{\partial z}$$

$$\rho\left[v_x\left(-y\frac{\partial v_y}{\partial y} - z\frac{\partial v_y}{\partial z}\right) + v_y\frac{\partial v_y}{\partial y} + v_z\frac{\partial v_y}{\partial z}\right] = -\frac{\partial p}{\partial y}$$

$$\rho\left[v_x\left(-y\frac{\partial v_z}{\partial y} - z\frac{\partial v_z}{\partial z}\right) + v_y\frac{\partial v_z}{\partial y} + v_z\frac{\partial v_z}{\partial z}\right] = -\frac{\partial p}{\partial z}$$

$$\left(\frac{2\gamma}{\gamma-1}\right)\frac{p}{\rho} + v_x^2 + v_y^2 + v_z^2 = \text{const}$$

Appendix 2 - Plots of Computations of Conical Flows

This appendix contains several plots resulting from the parametric computational study described in section 2.5.

Once the solutions were found, velocities could be plotted using 2-D plotting routines in two different ways: 1) by plotting the velocities in the cross flow directions directly, or 2) by plotting the velocities in the θ and ϕ directions at each point, or the velocity on the surface of a sphere projected onto the cross flow plane. Method 1 illustrates zero cross flow velocity in the free stream, where method 2 illustrates zero velocity through the surface of the fin. Both are required to get a complete picture of the velocity flow field, as illustrated in figure 19.

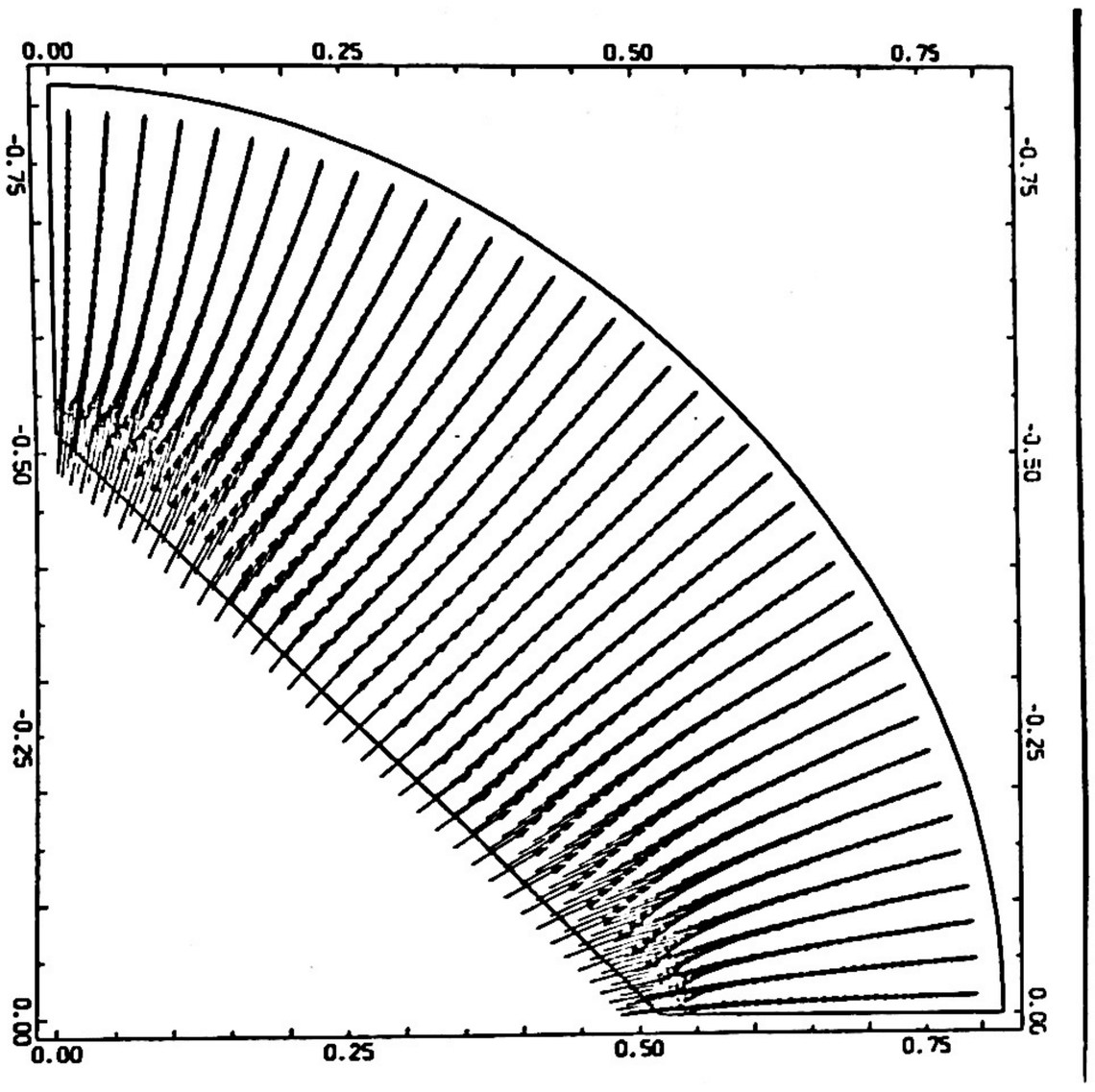


Fig. 19a. Velocity in x and y directions.

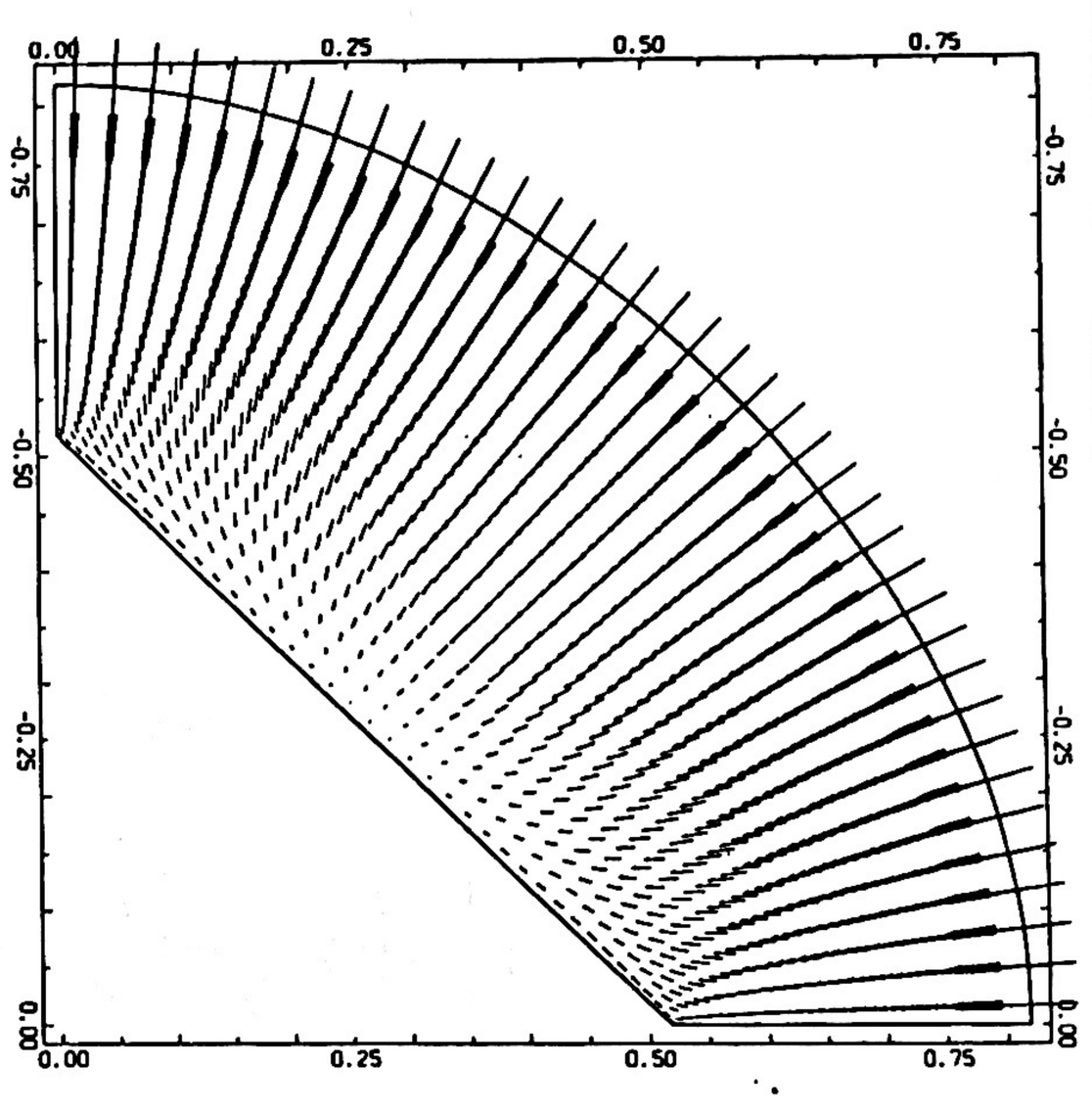


Fig. 19b. Velocity in θ and ϕ directions.

Figure 19: Velocity vectors plotted in a cross-flow plane.

An example of the grid used for these calculations is given in figure 20.

Isolines of constant pressure for various configurations are shown in figures 21a-21hh and figures 22a-22b.

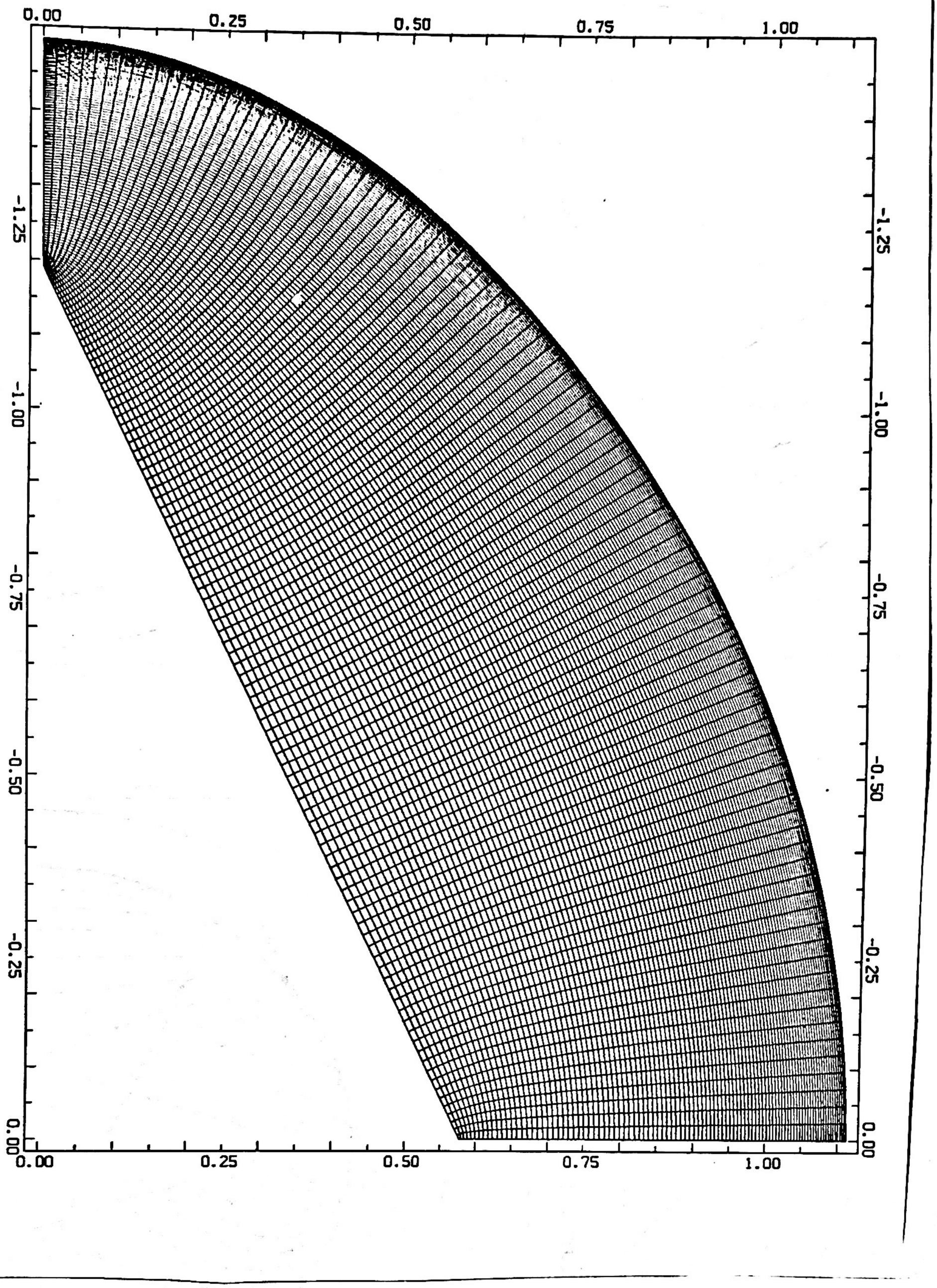


Figure 20: Example of grid used for numerical computations.

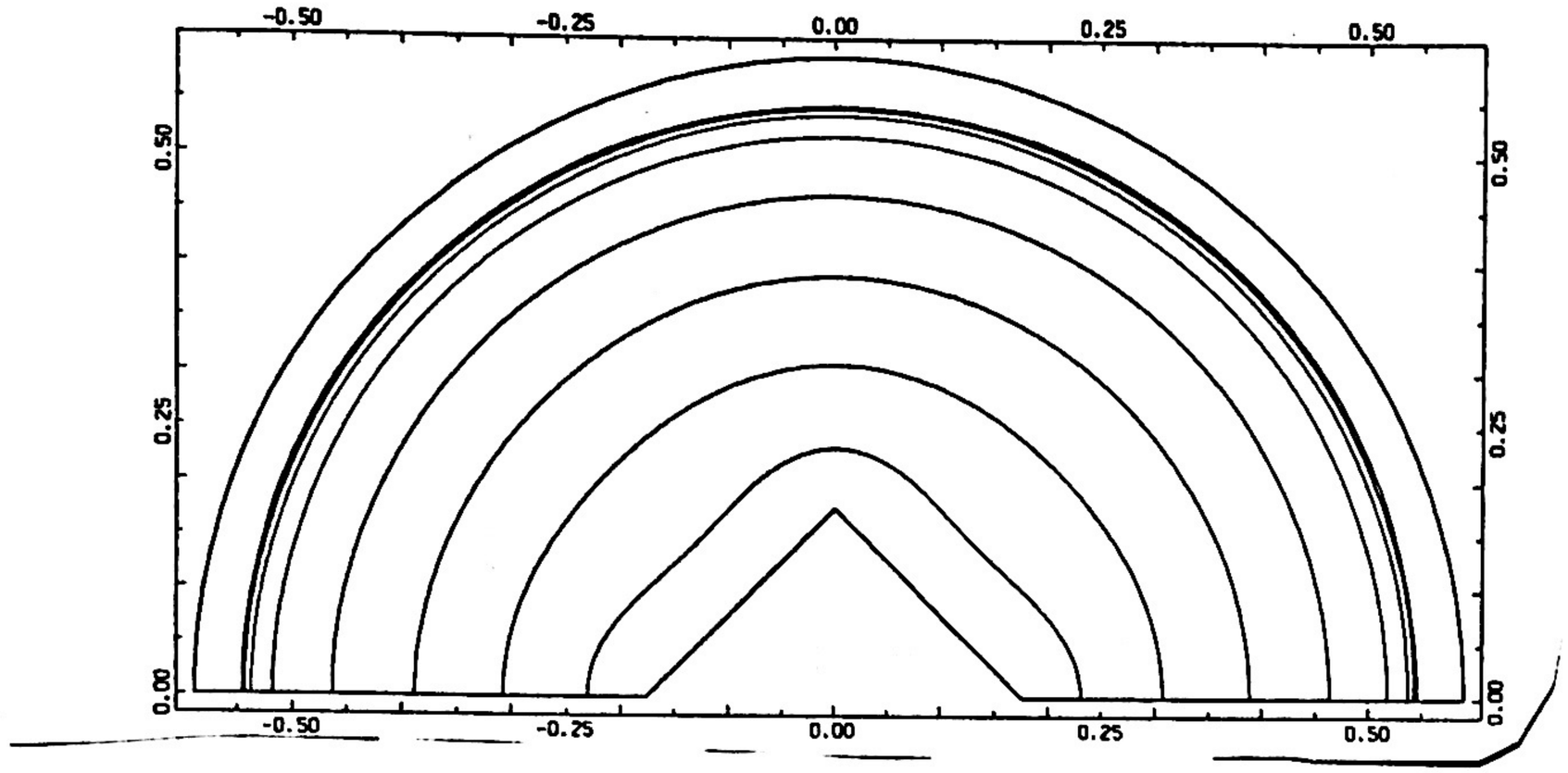


Figure 21a: α=10°, θ=10°

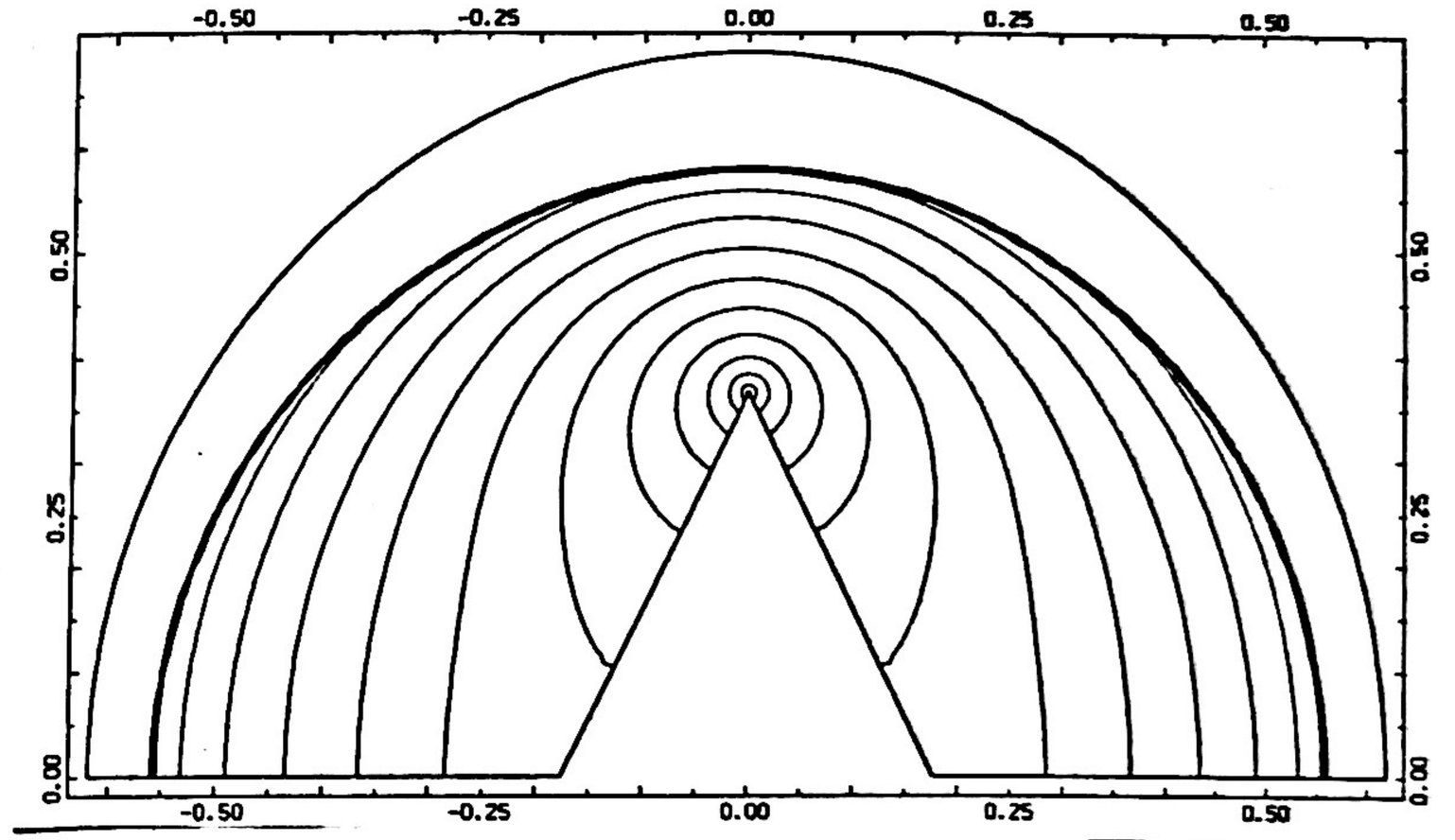


Figure 21b: α=10°, θ=20°

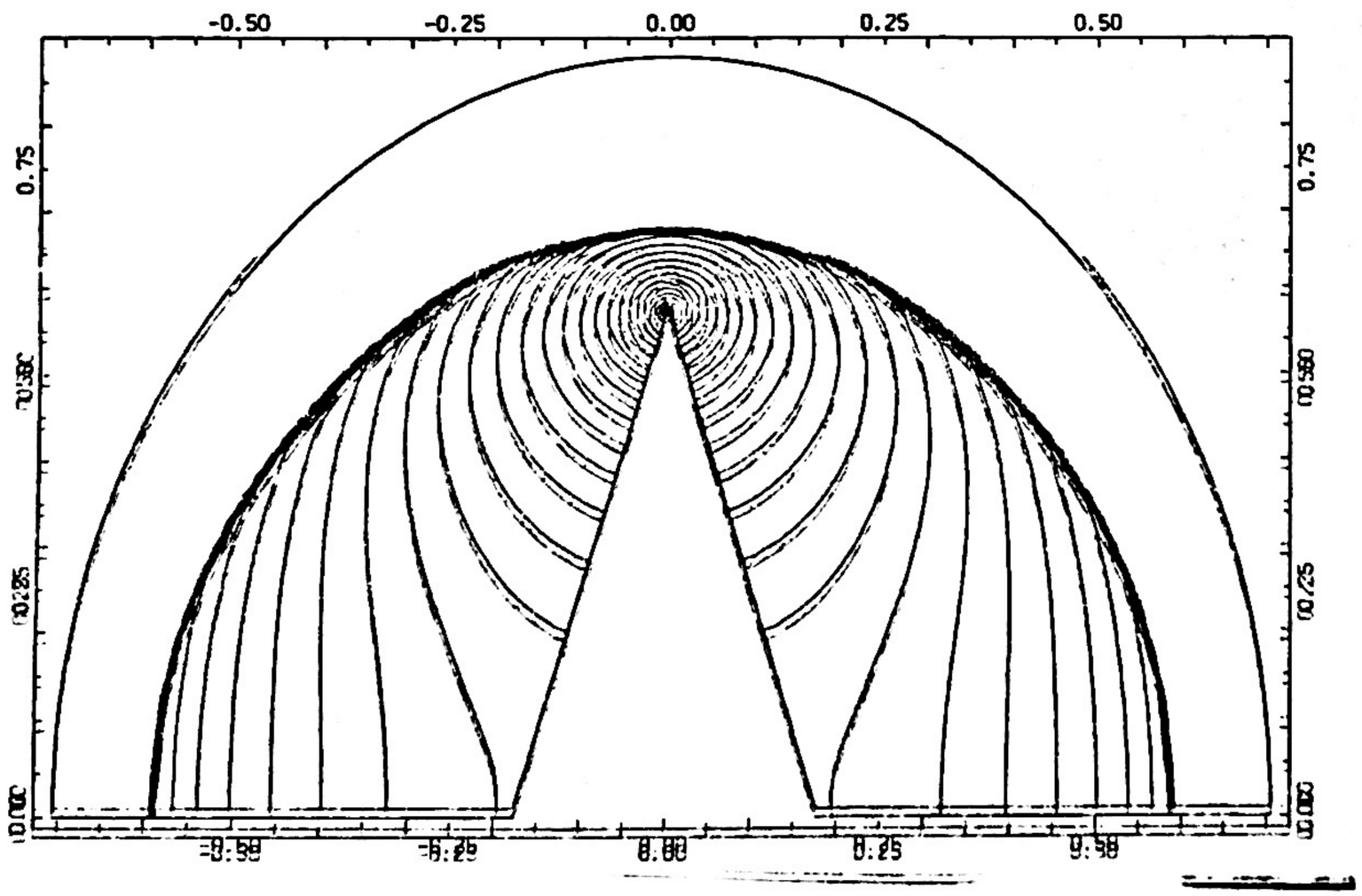


Figure 21c: α=10°, θ=30°

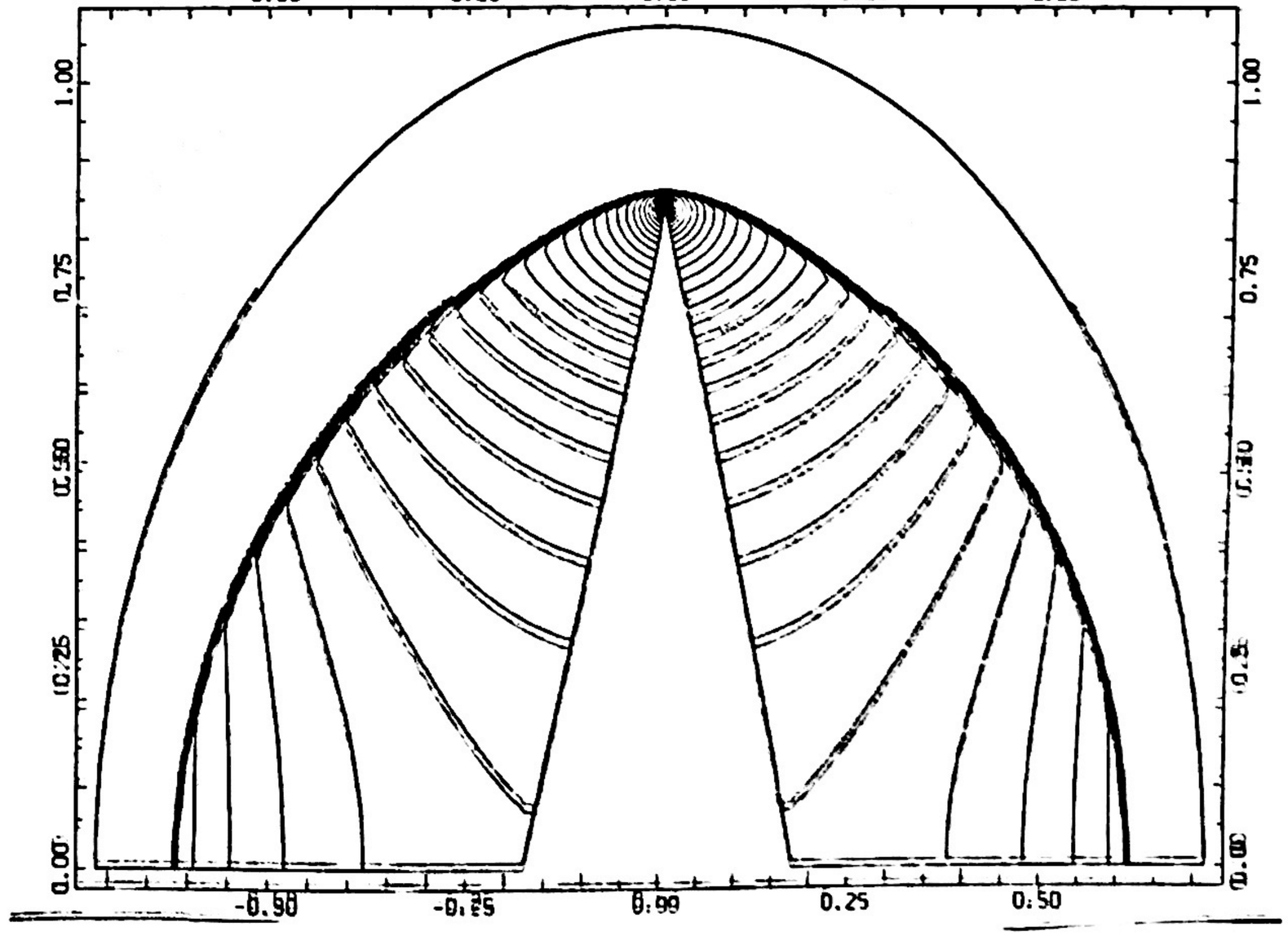


Figure 21d: α=10°, θ=40°

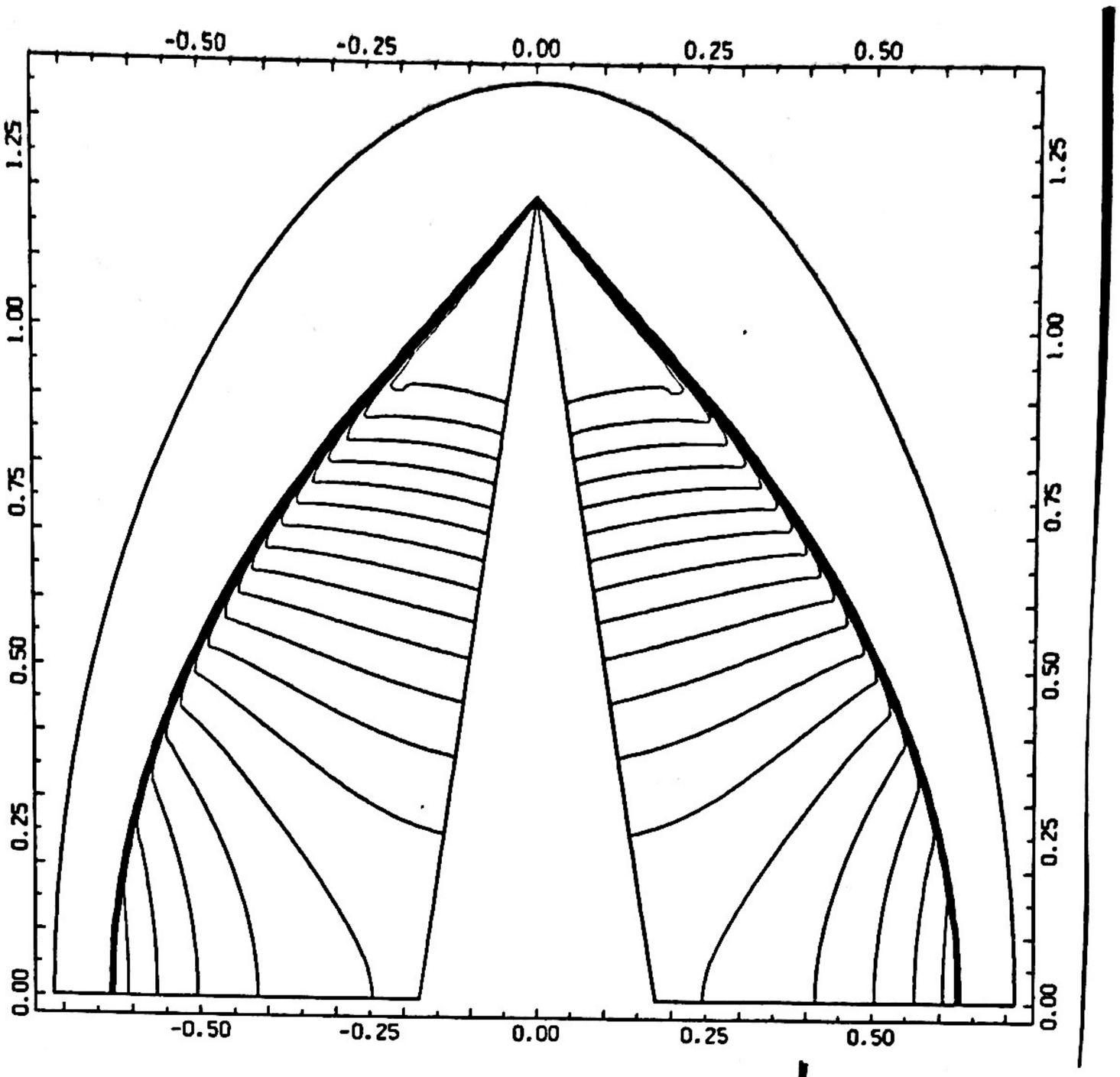


Figure 21e: $\alpha=10°$, $\theta=50°$

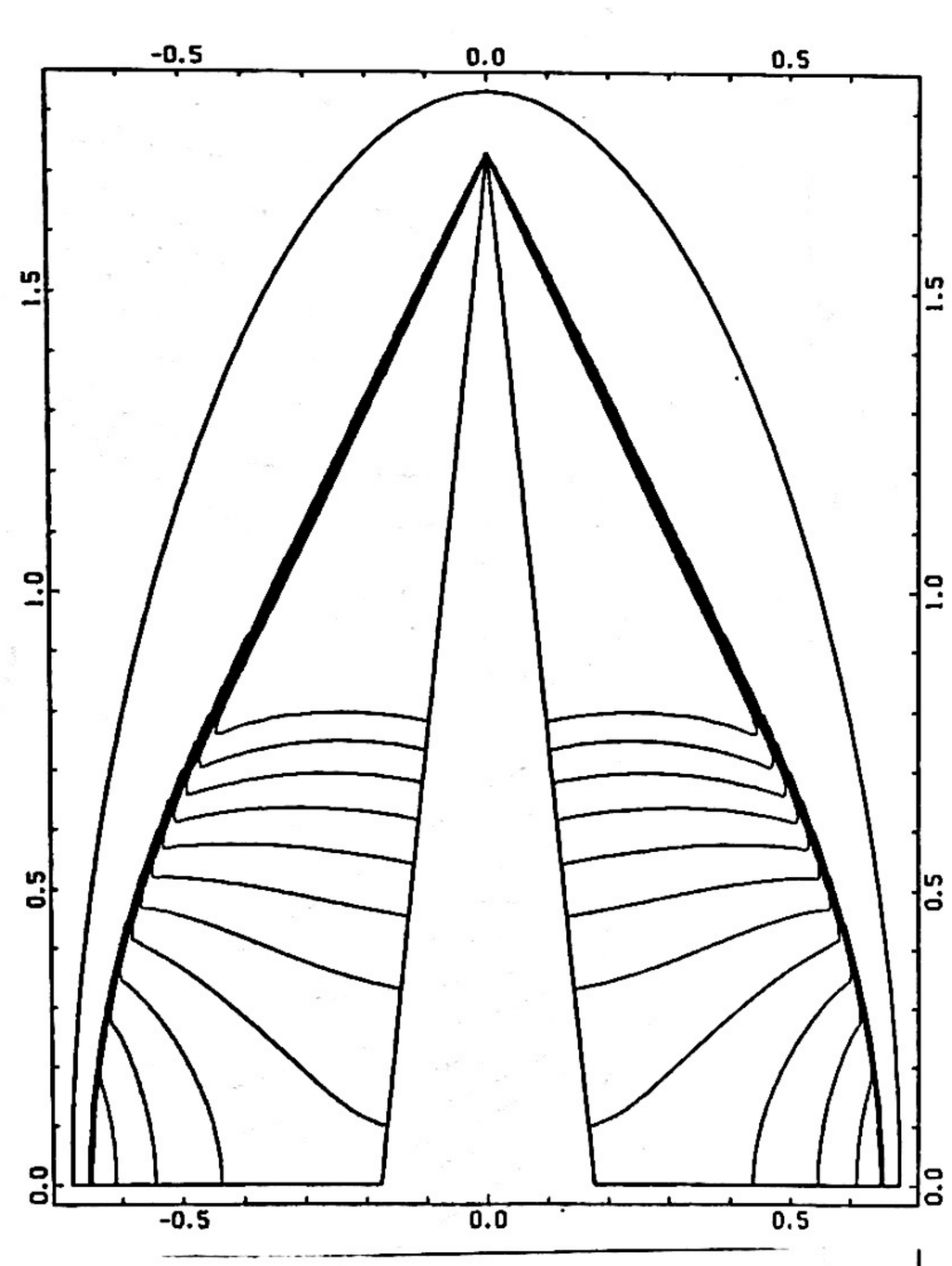


Figure 21f: $\alpha=10°$, $\theta=60°$

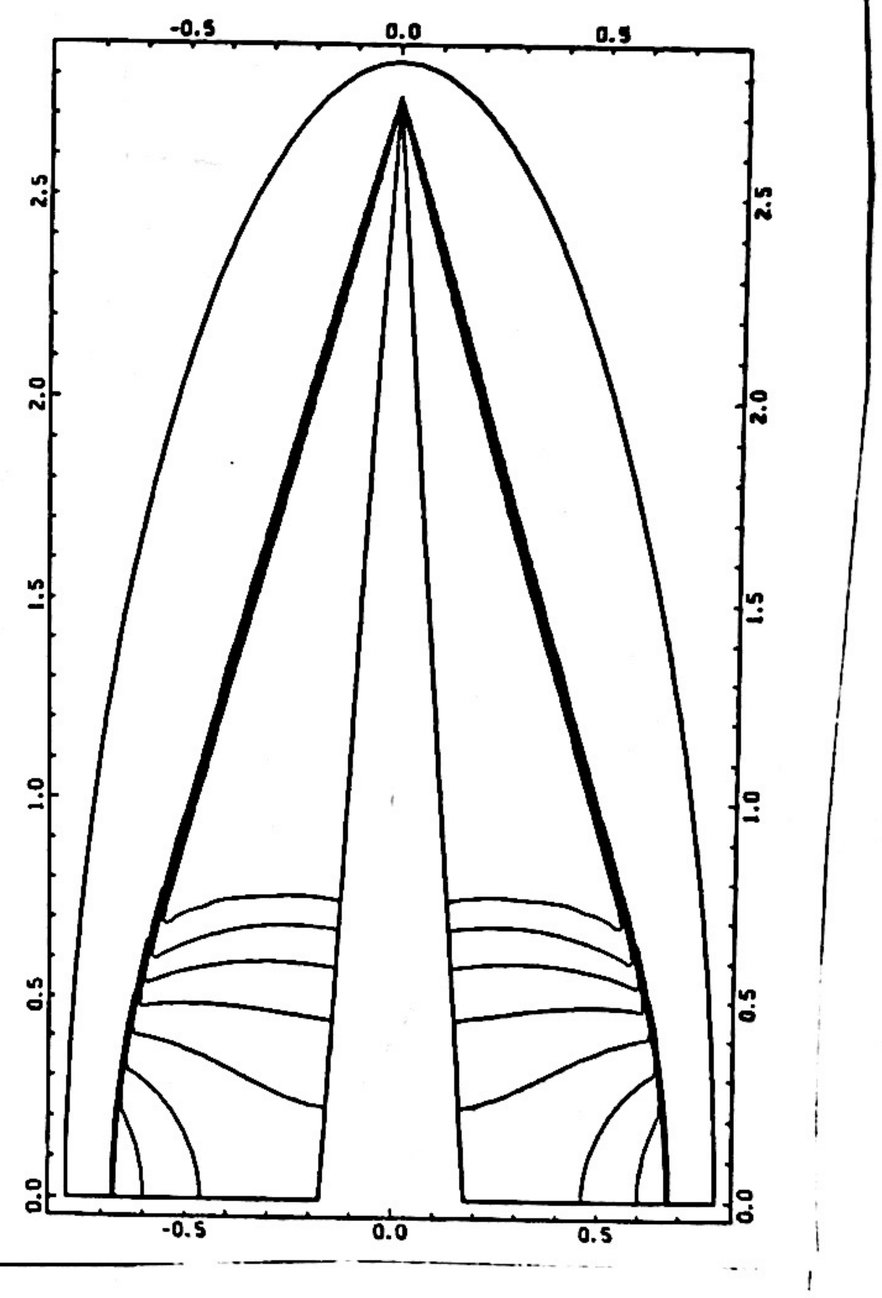


Figure 21g: $\alpha=10°$, $\theta=70°$

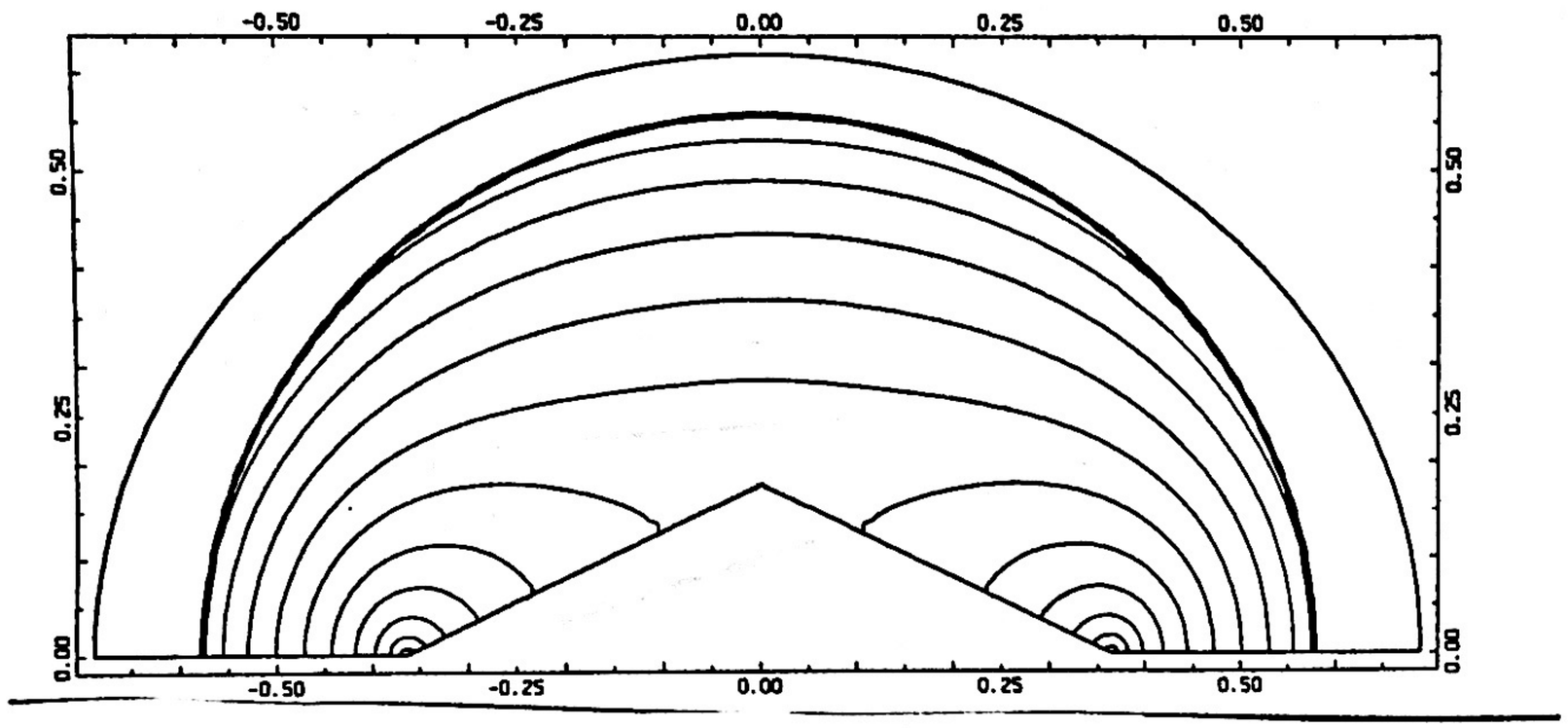


Figure 21h: α=20°, θ=10°

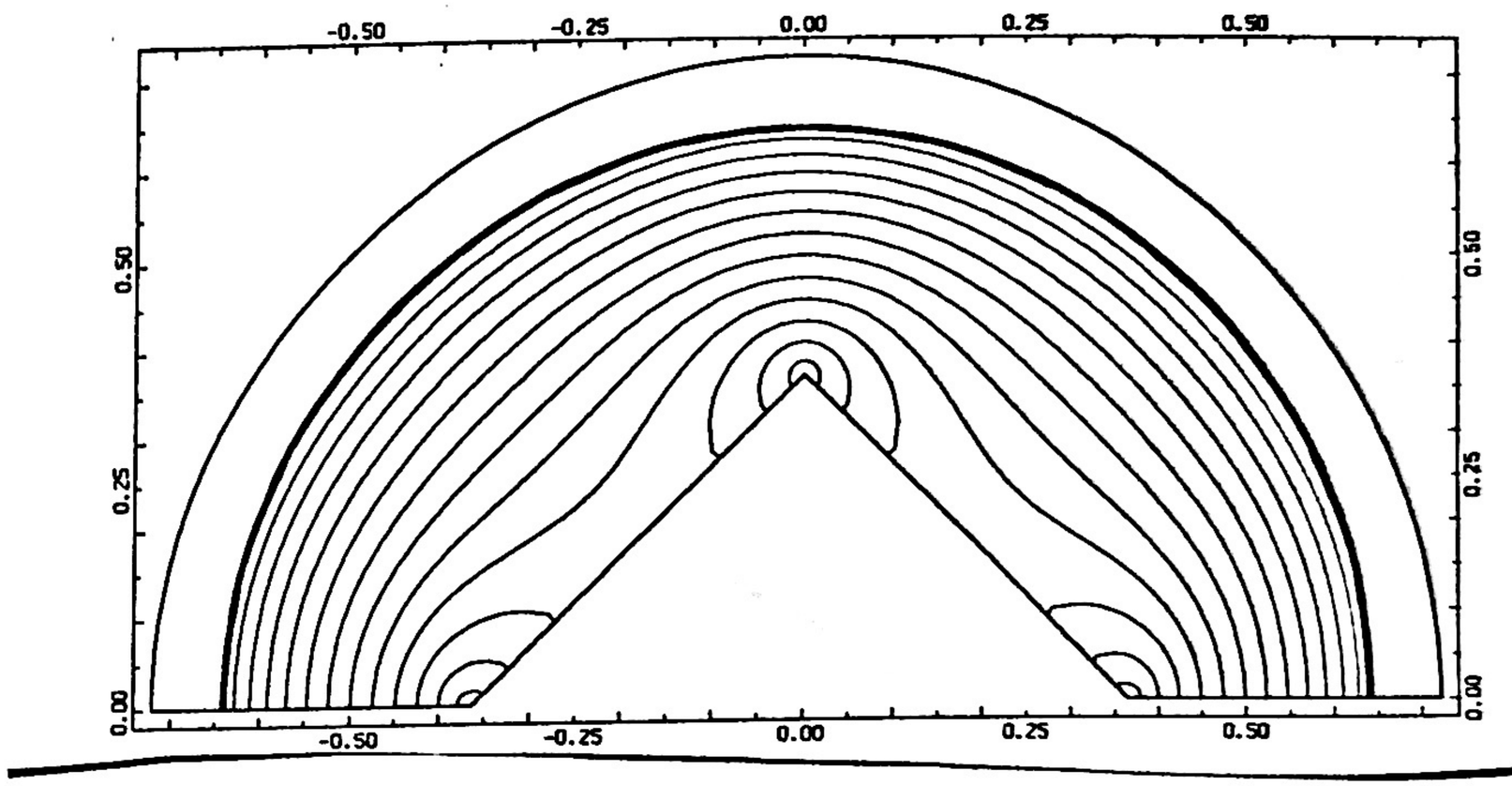


Figure 21i: α=20°, θ=20°

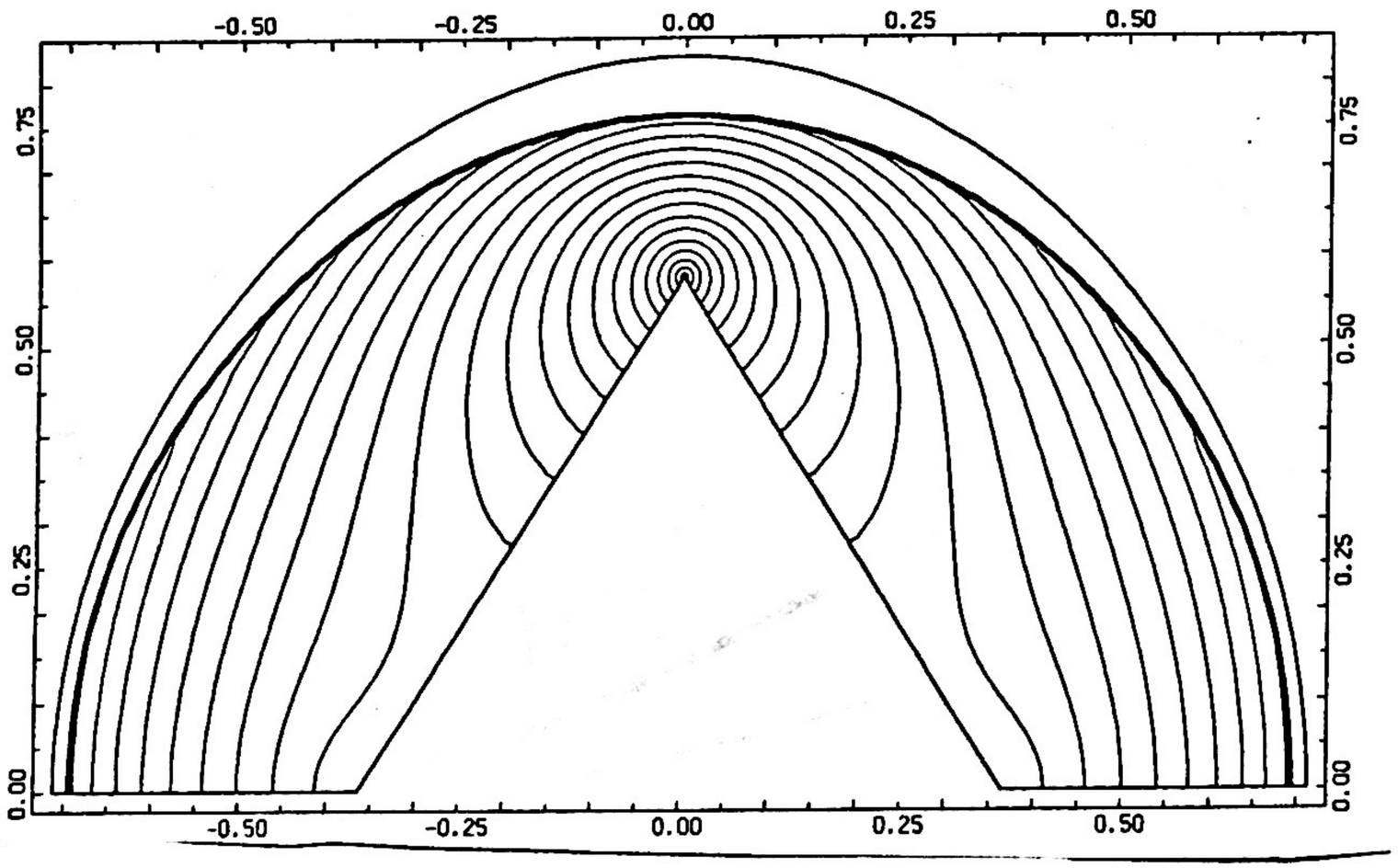


Figure 21j: α=20°, θ=30°

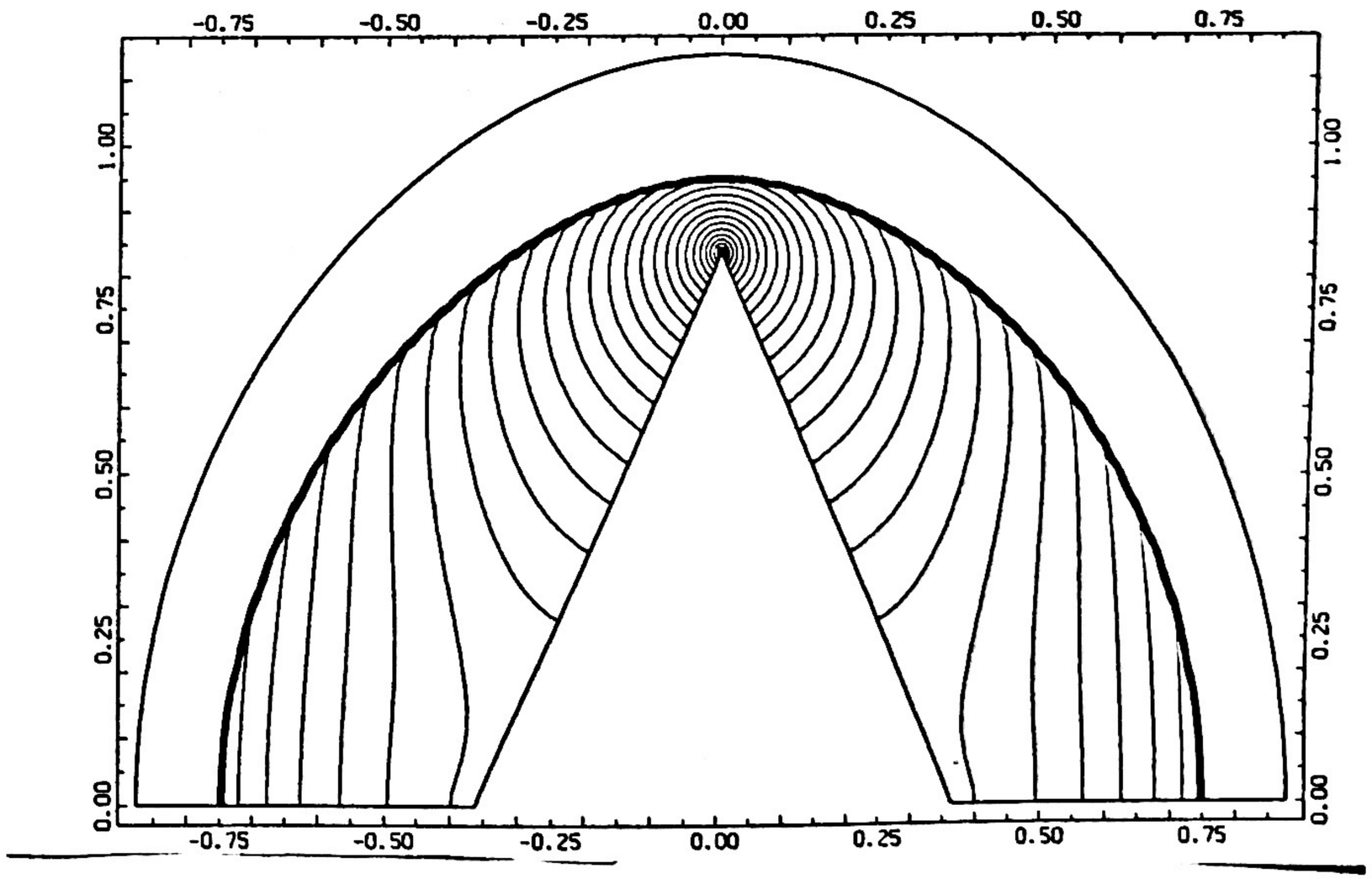


Figure 21k: α=20°, θ=40°

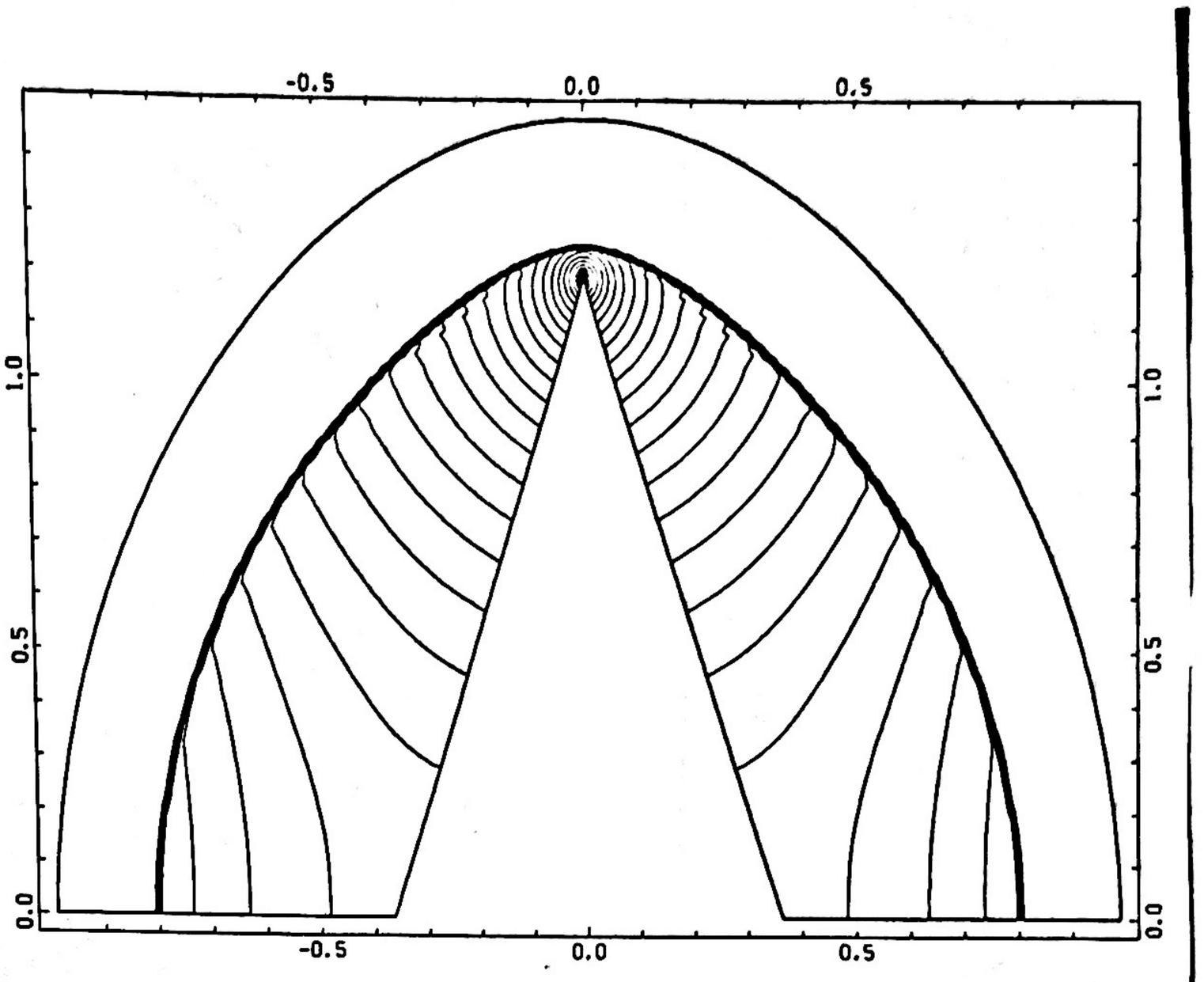


Figure 21l: $\alpha=20°$, $\theta=50°$

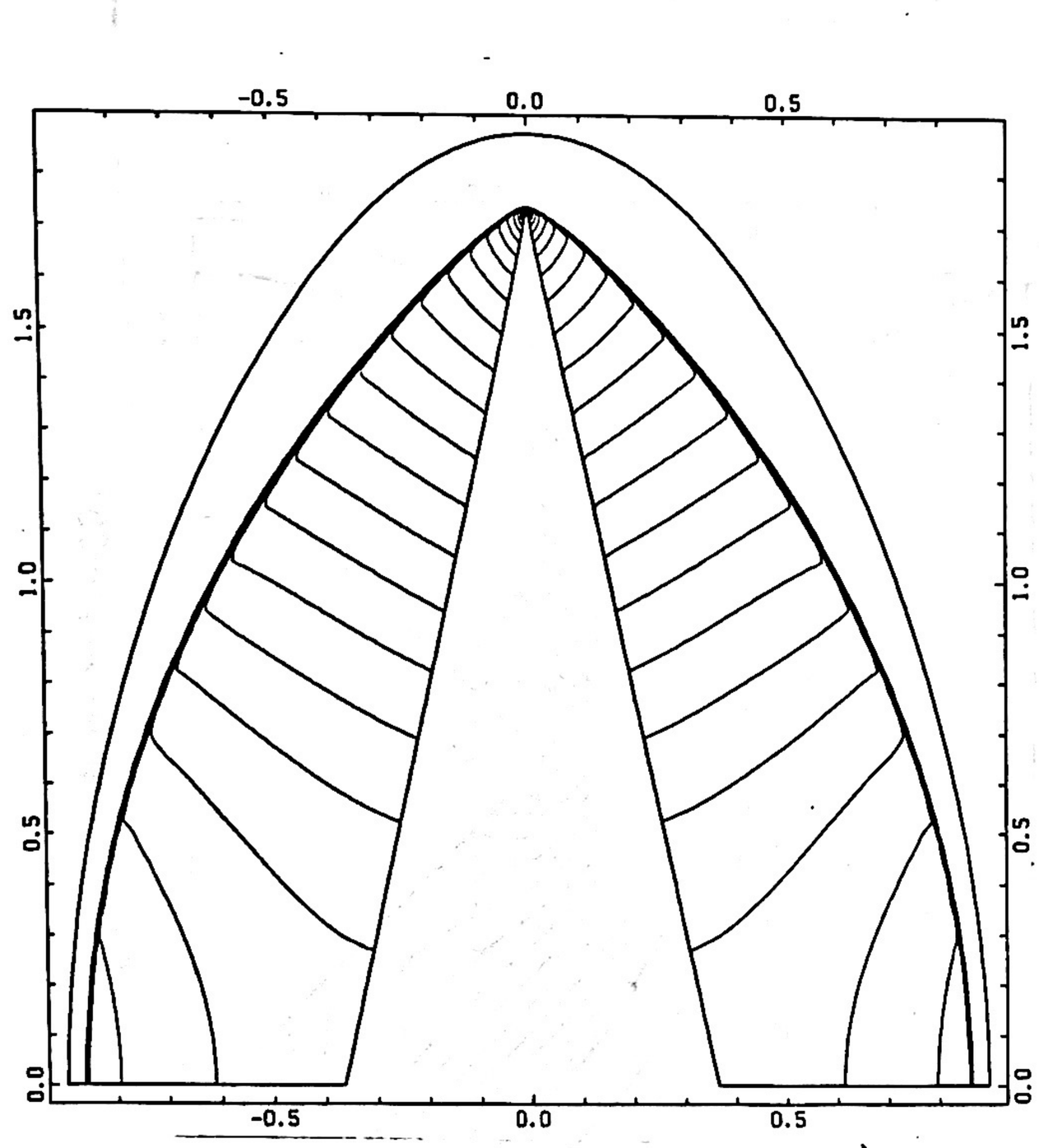


Figure 21m: $\alpha=20°$, $\theta=60°$

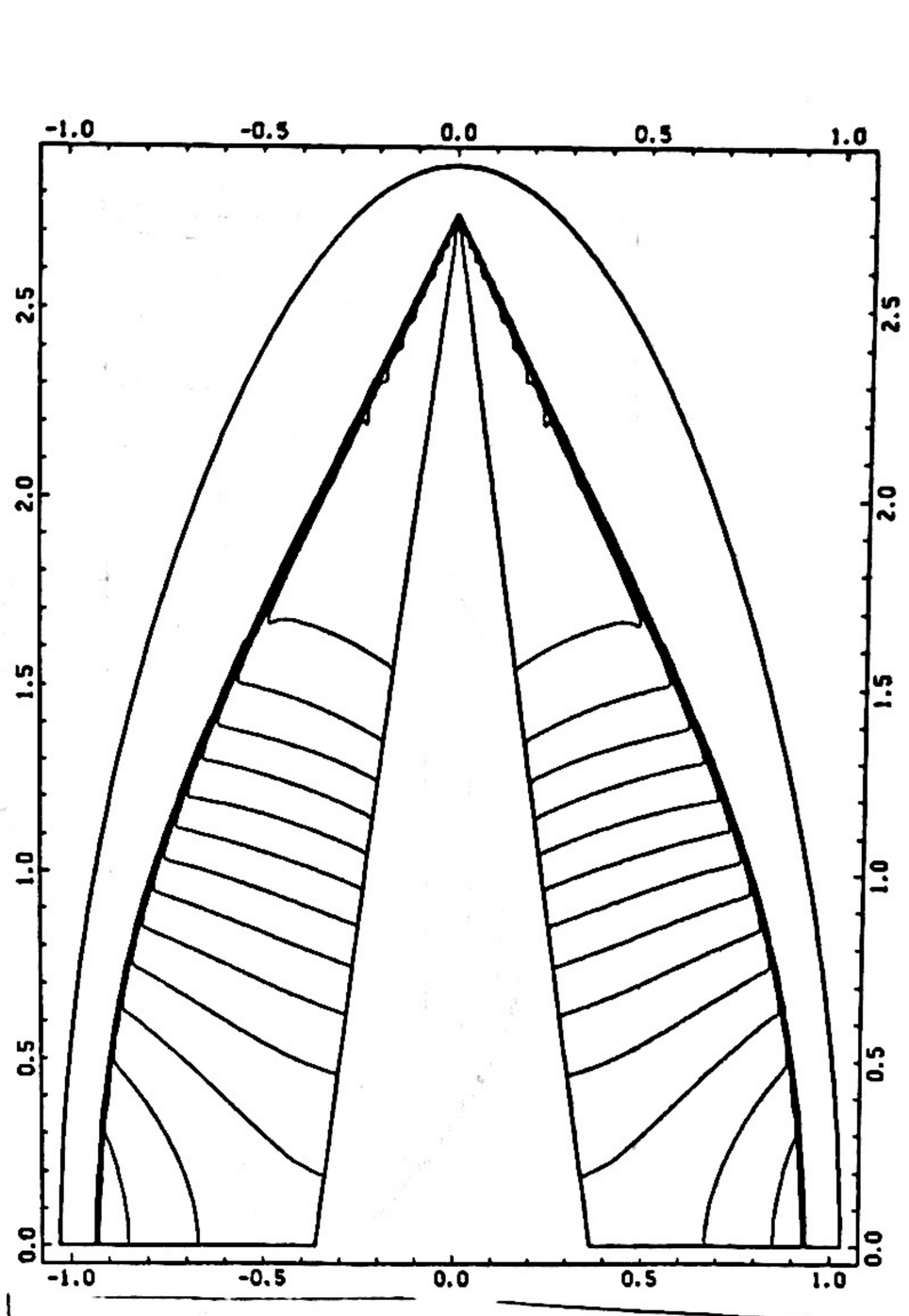


Figure 21n: $\alpha=20°$, $\theta=70°$

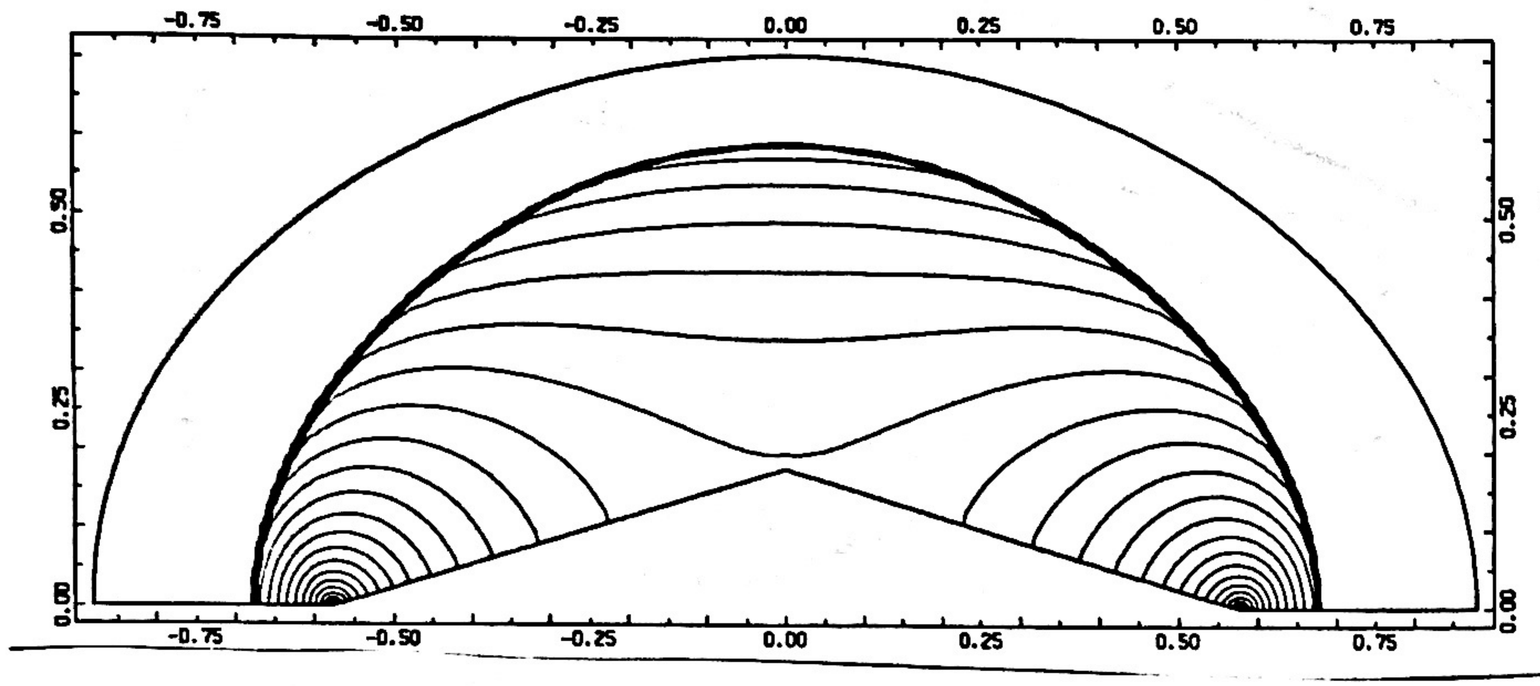


Figure 21o: α=30°, θ=10°

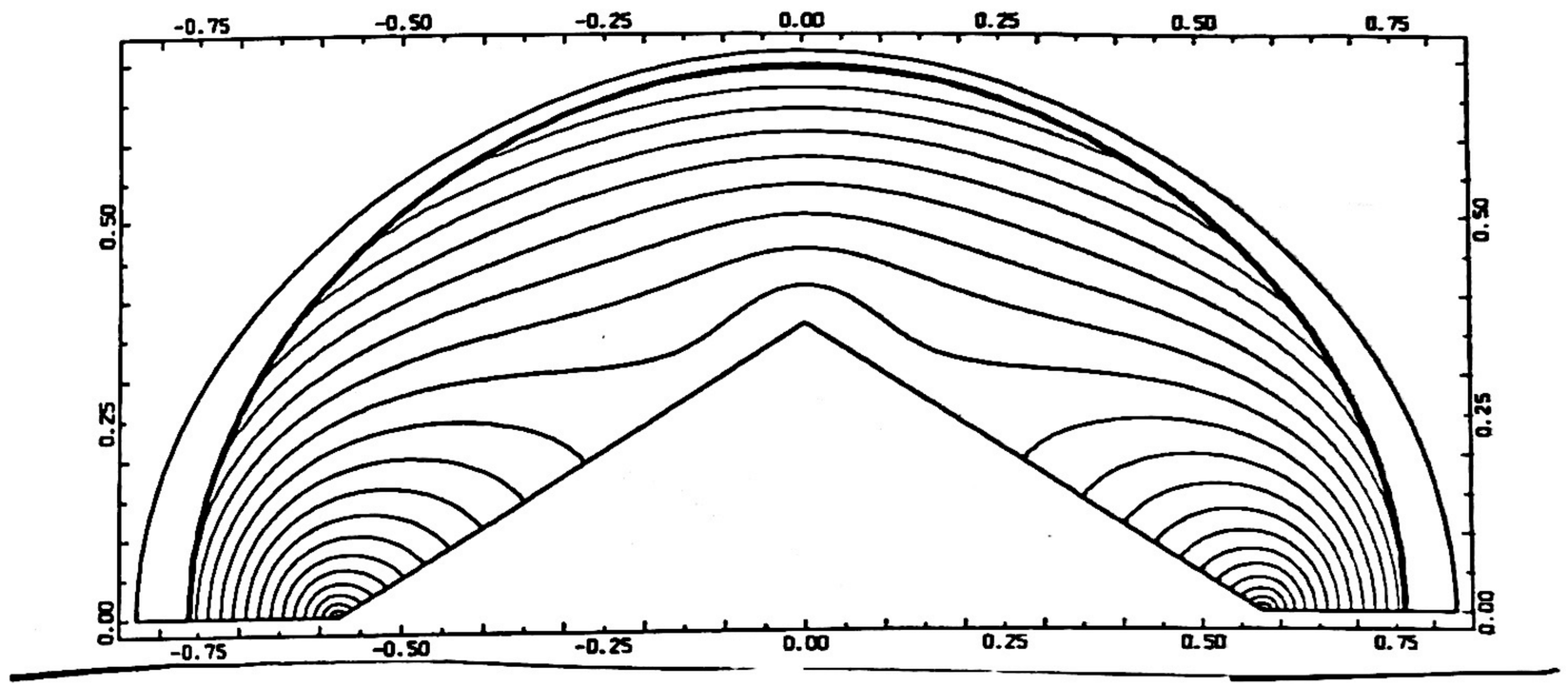


Figure 21p: α=30°, θ=20°

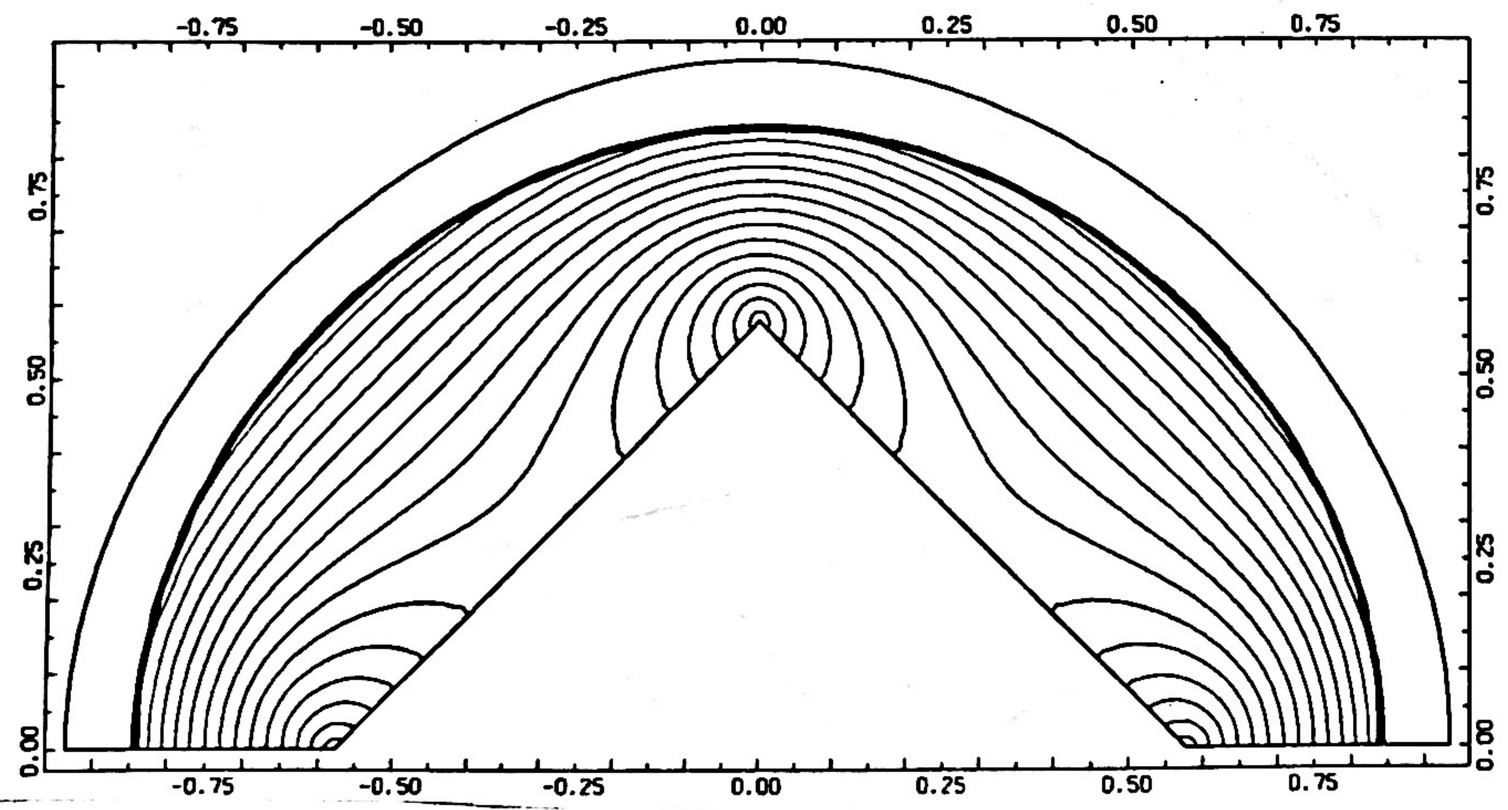


Figure 21q: α=30°, θ=30°

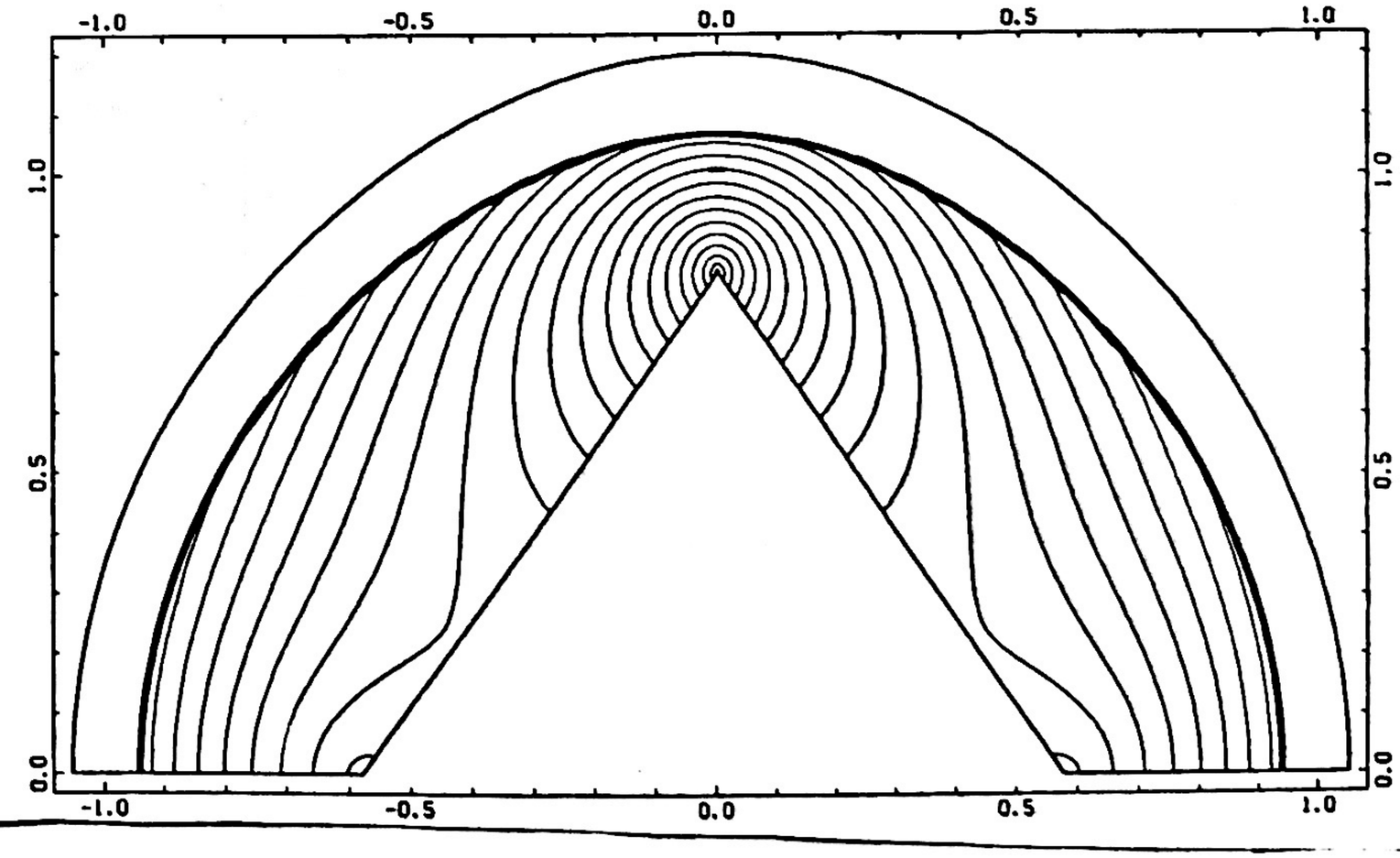


Figure 21r: α=30°, θ=40°

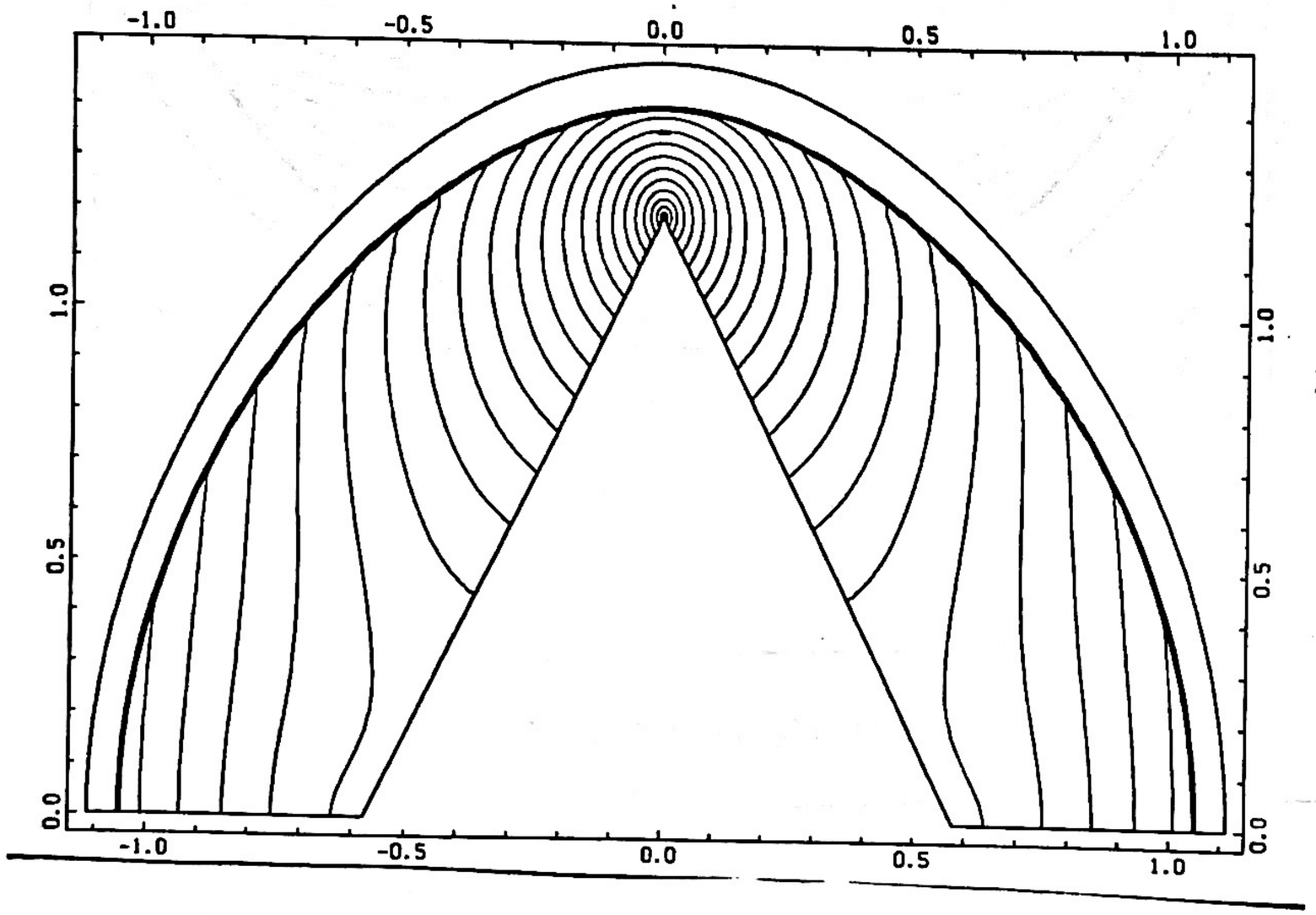


Figure 21s: α=30°, θ=50°

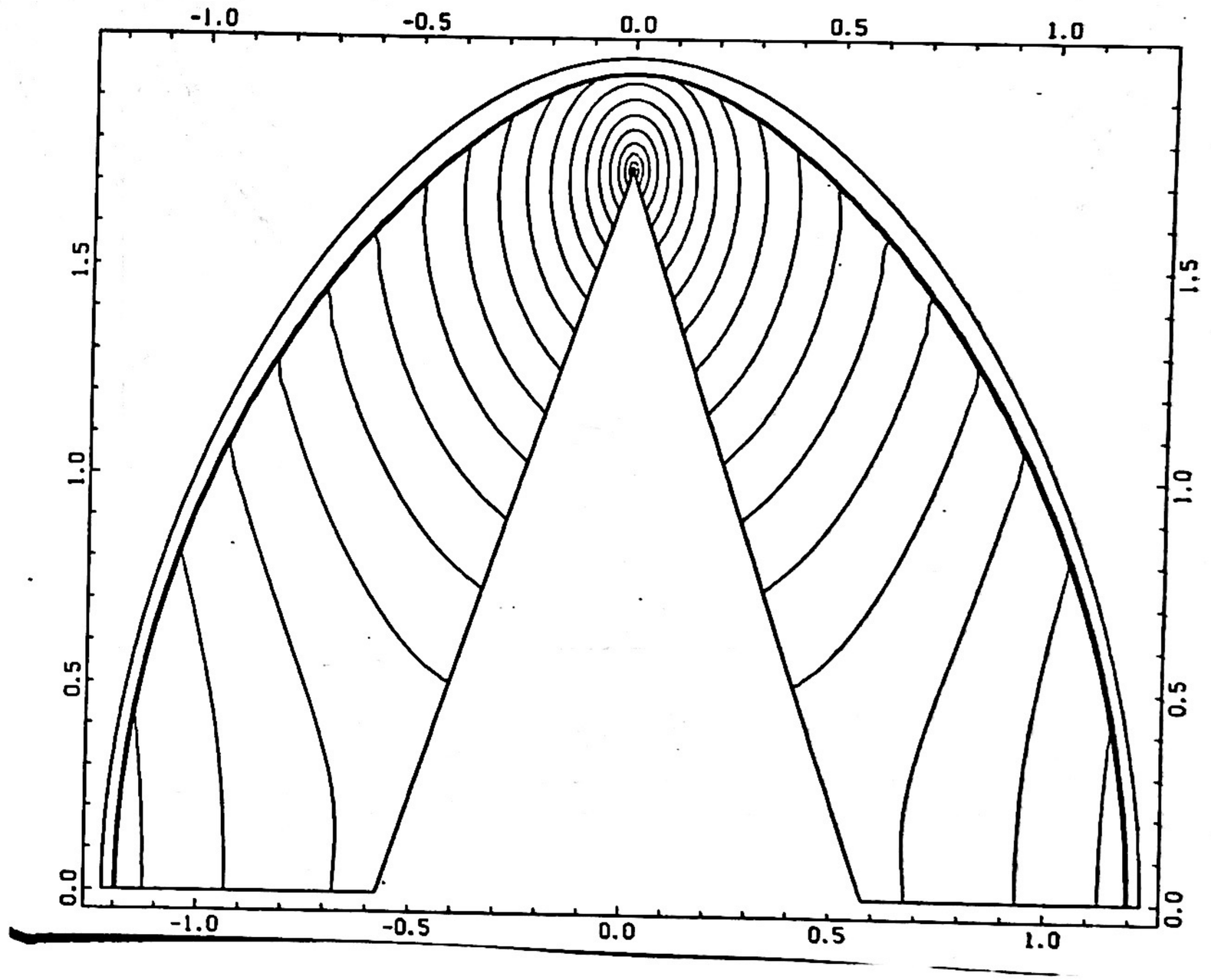


Figure 21t: α=30°, θ=60°

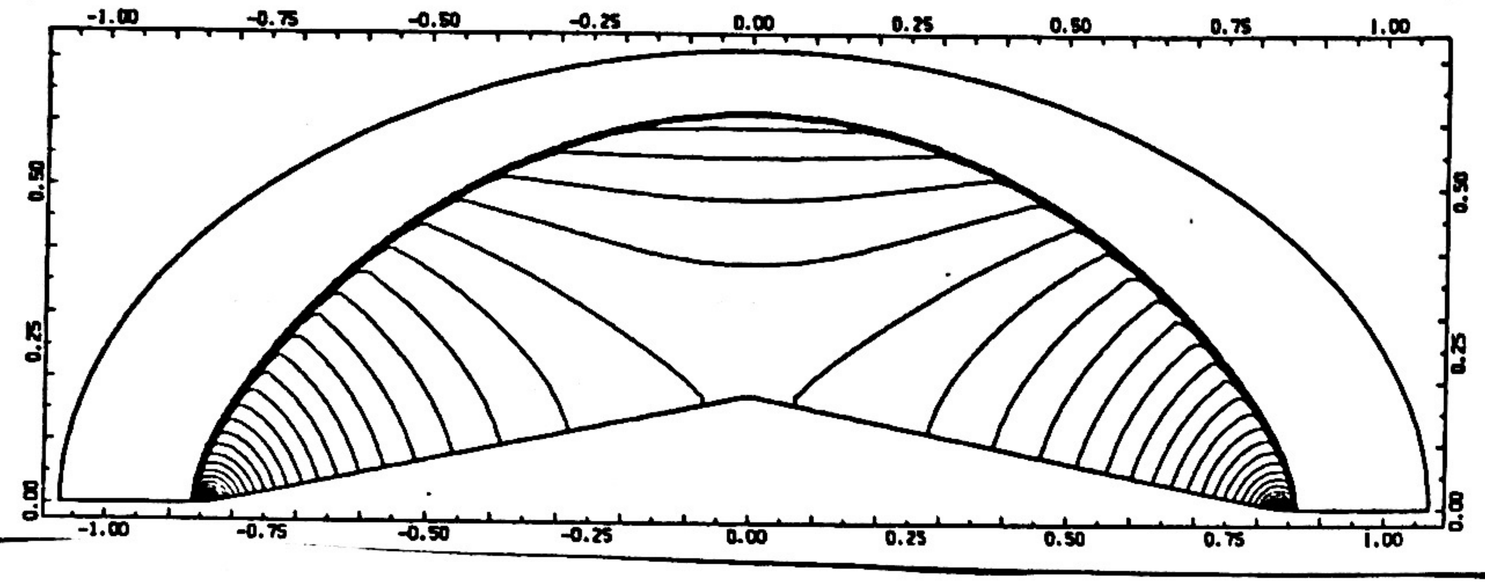


Figure 21u: α=40°, θ=10°

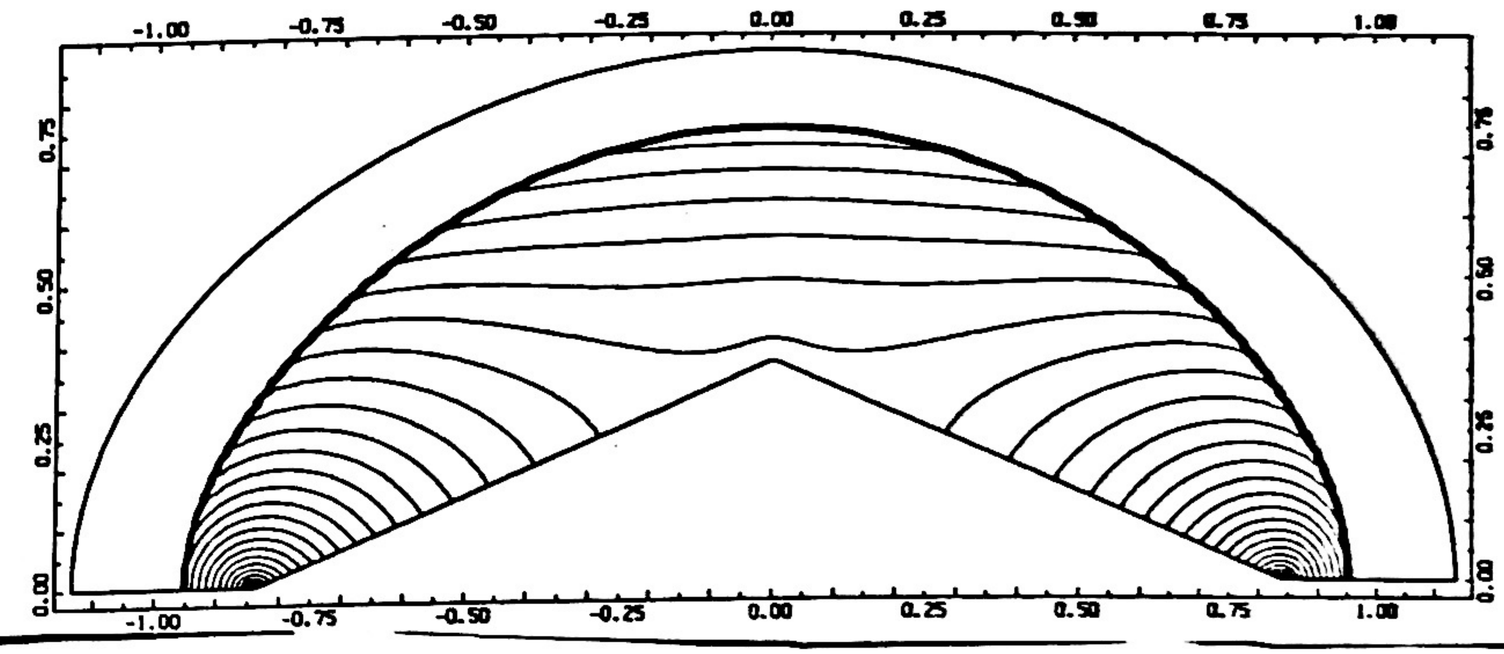


Figure 21v: α=40°, θ=20°

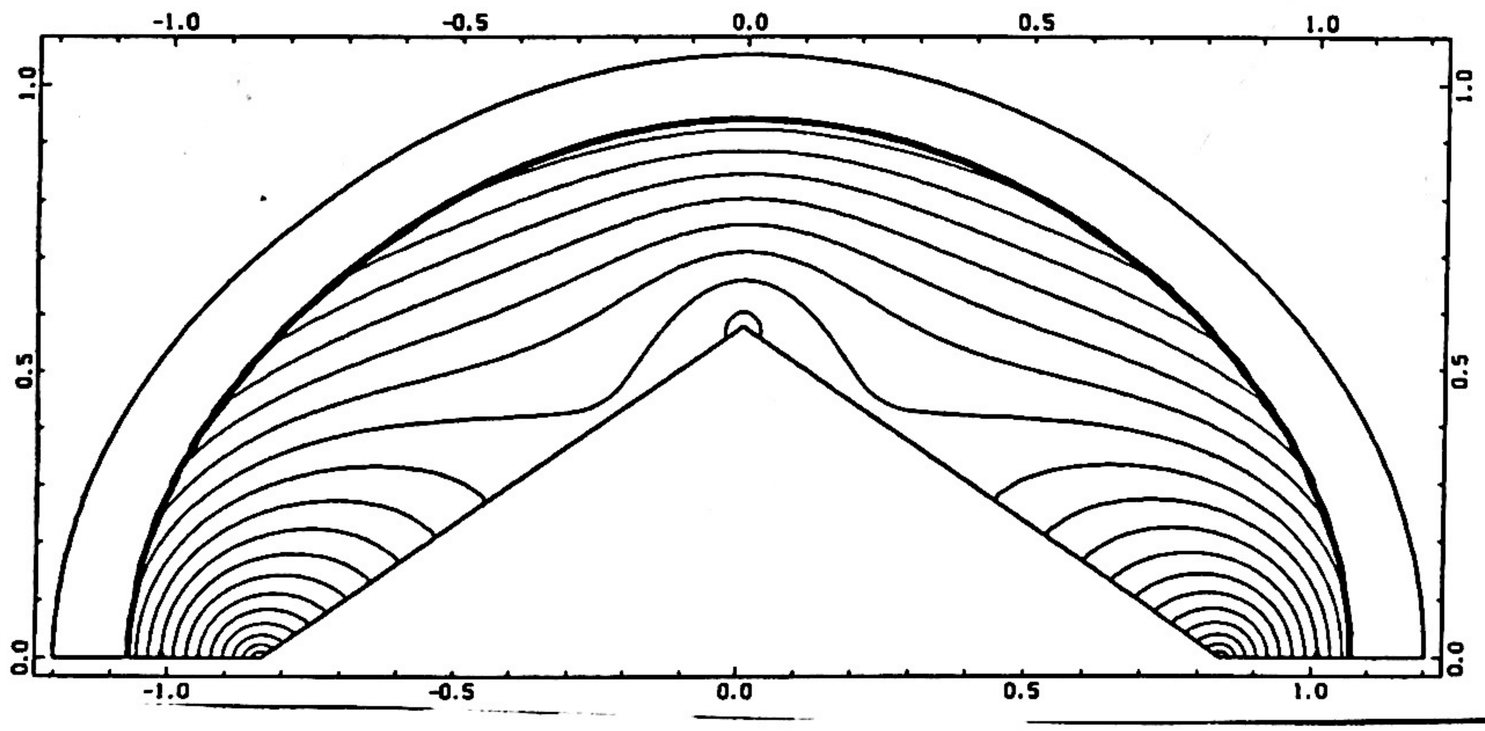


Figure 21w: α=40°, θ=30°

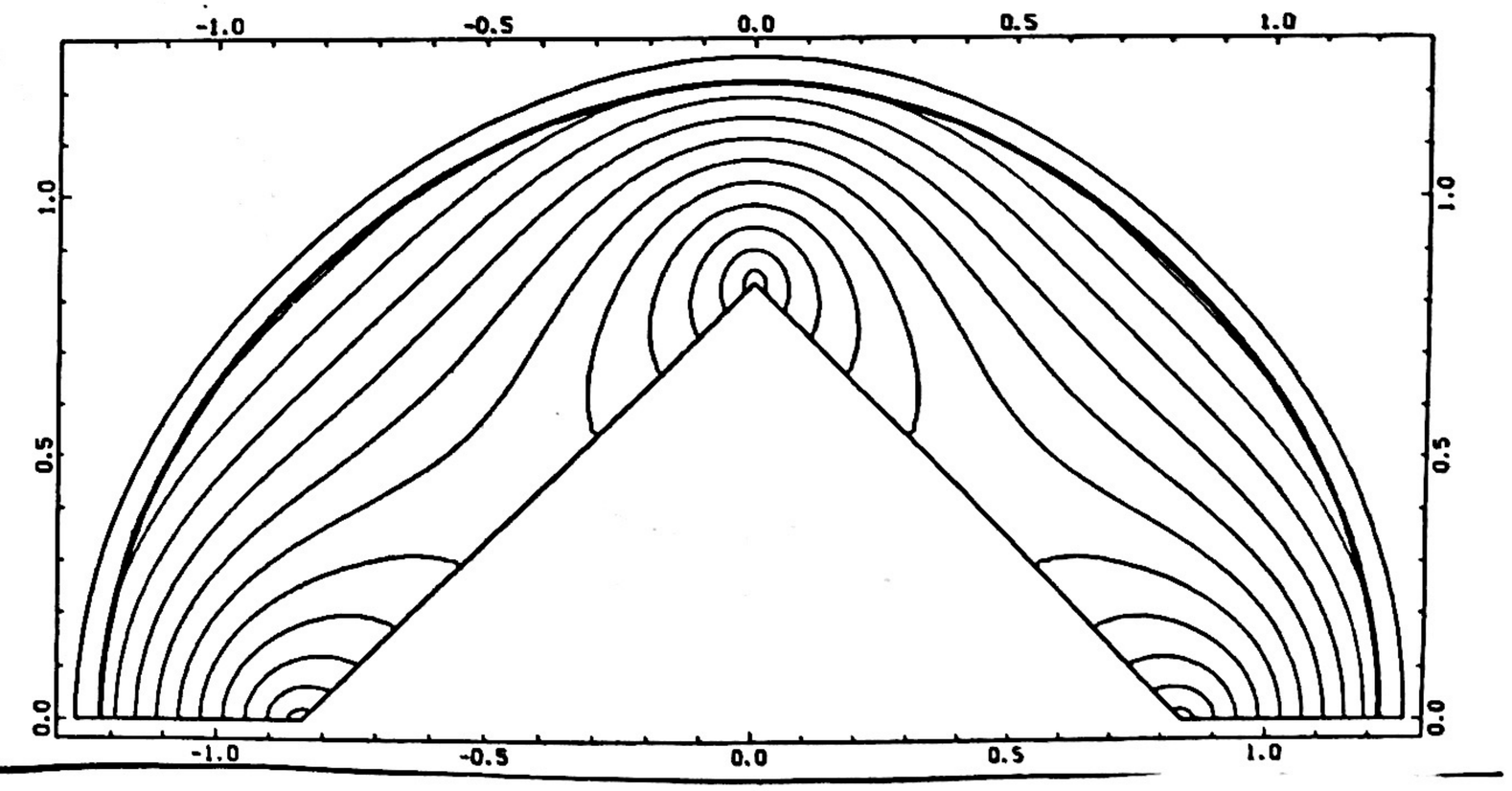


Figure 21x: α=40°, θ=40°

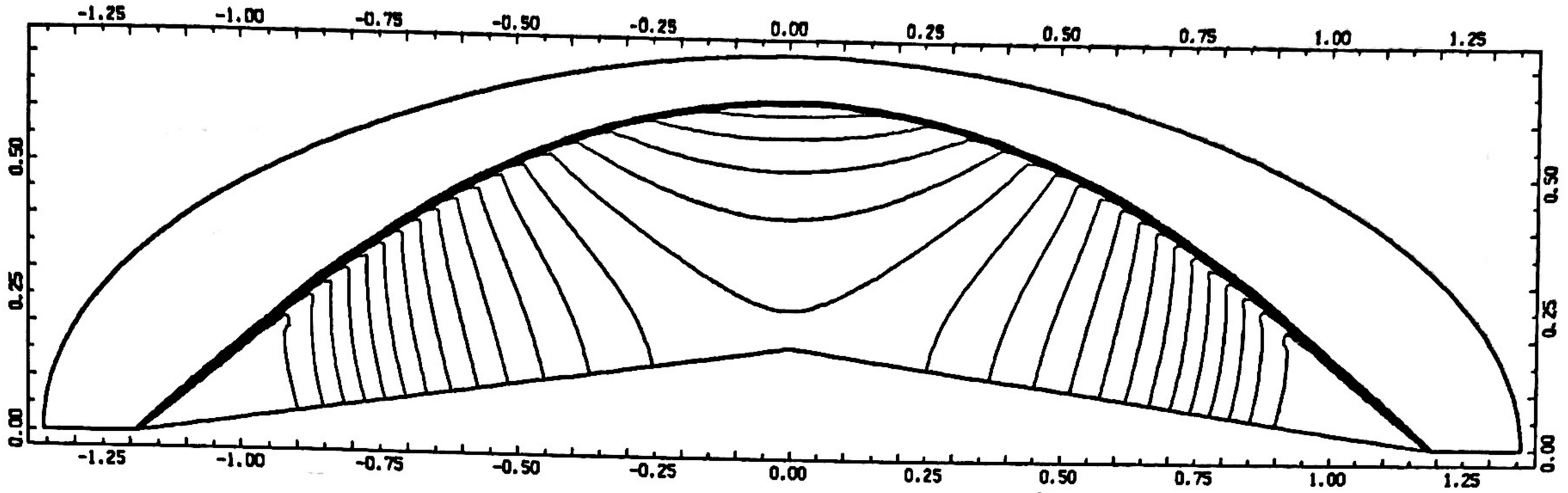


Figure 21y: α=50°, θ=10°

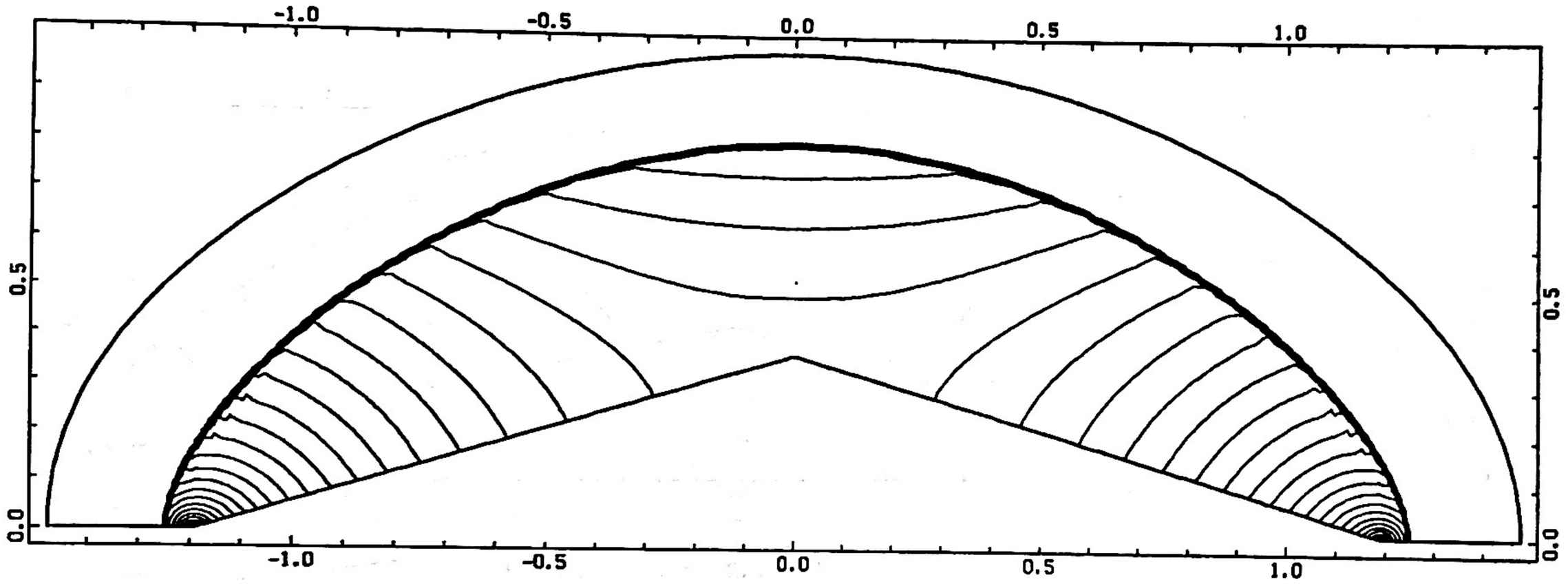


Figure 21z: α=50°, θ=20°

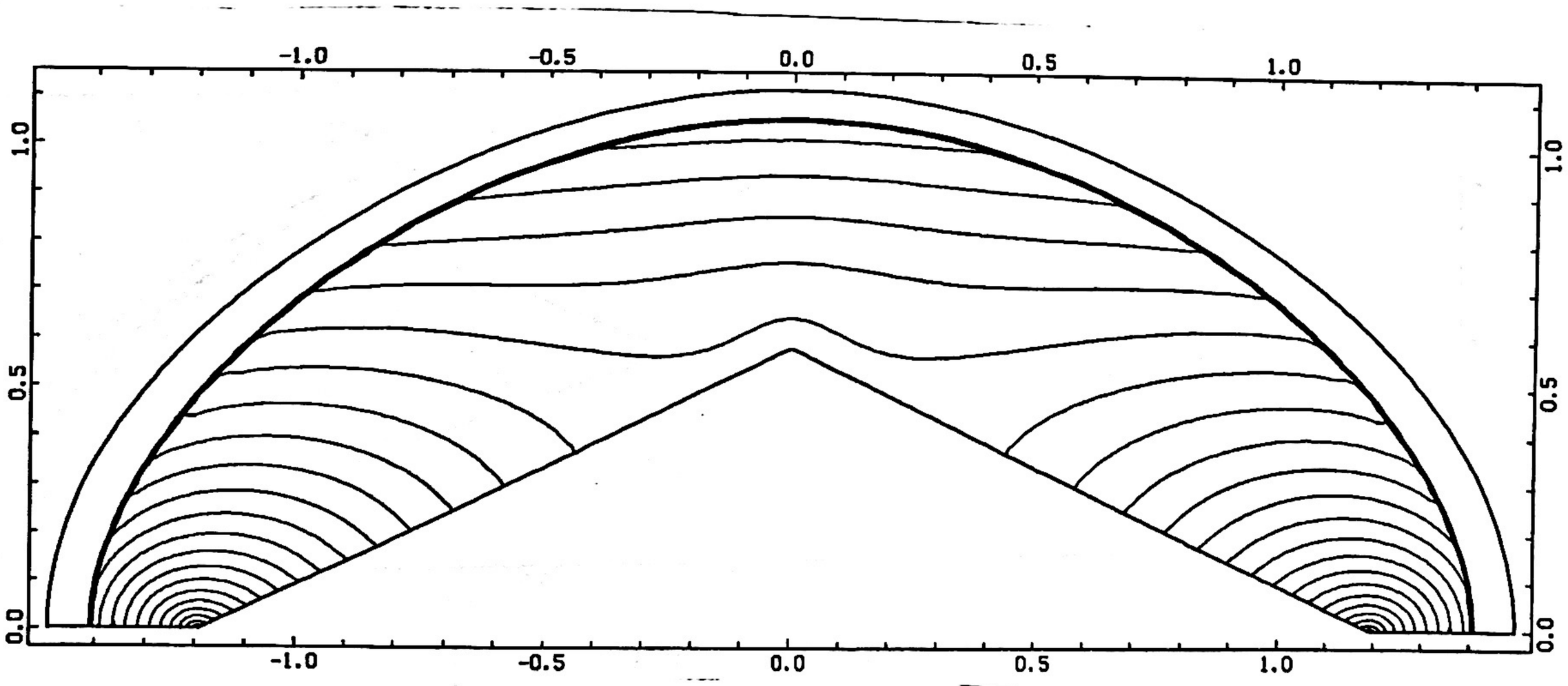


Figure 21aa: α=50°, θ=30°

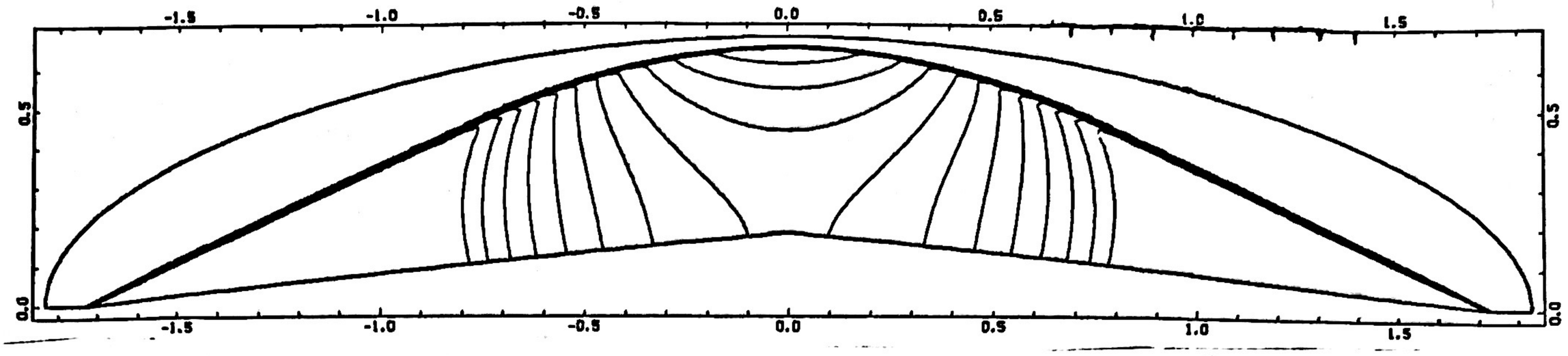


Figure 21bb: α=60°, θ=10°

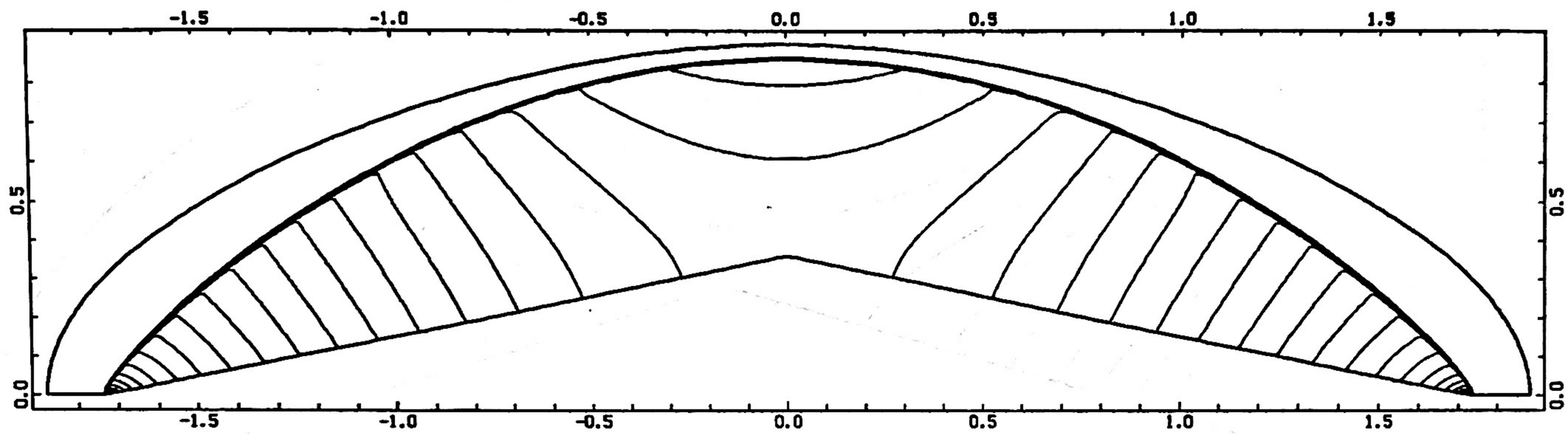


Figure 21cc: α=60°, θ=20°

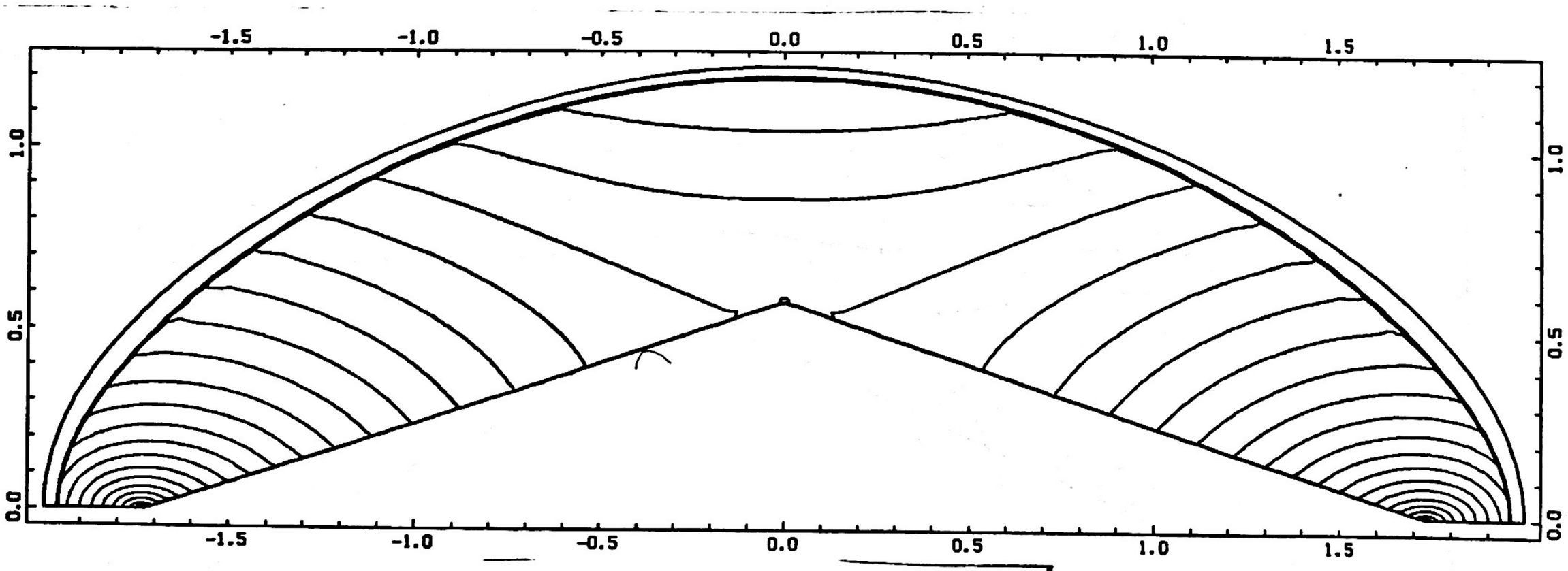


Figure 21dd: α=60°, θ=30°

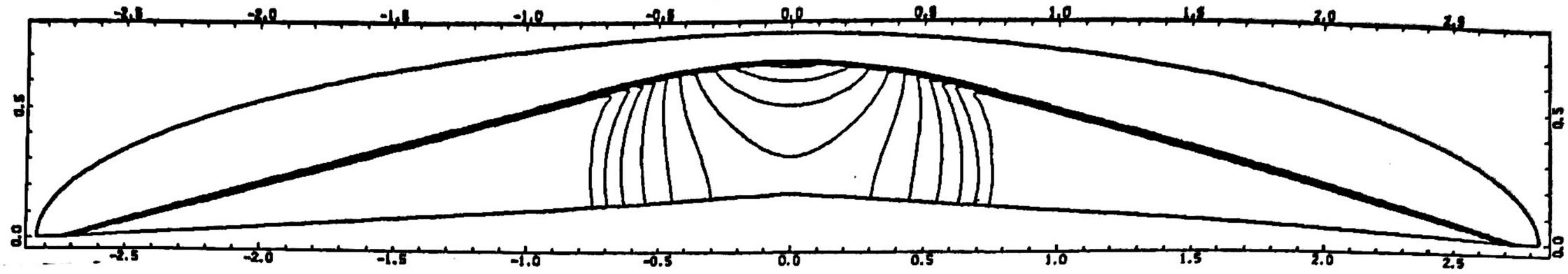


Figure 21ee: α=70°, θ=10°

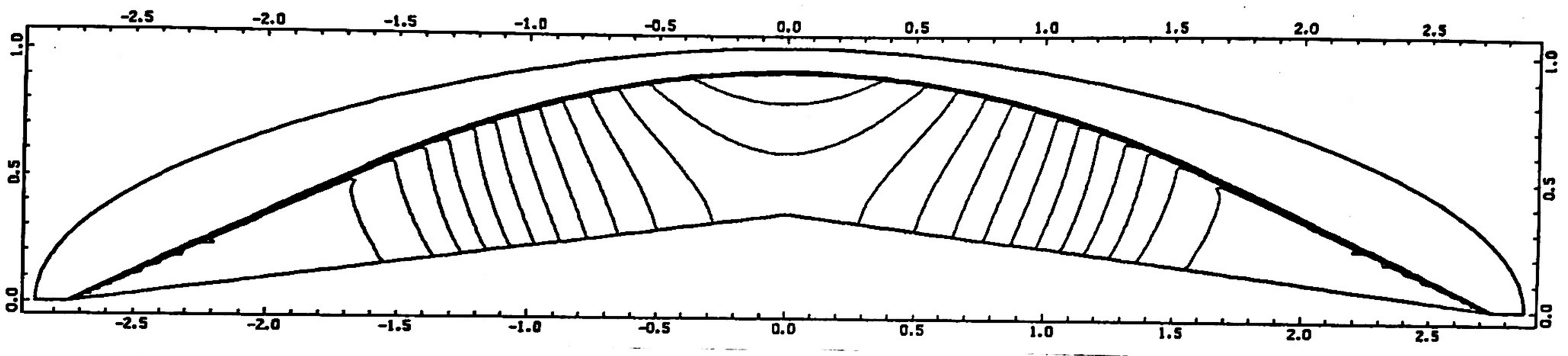


Figure 21ff: α=70°, θ=20°

Figure 21: Pressure isolines for Euler flow at Mach 2 over various fins. in the cross-flow plane.

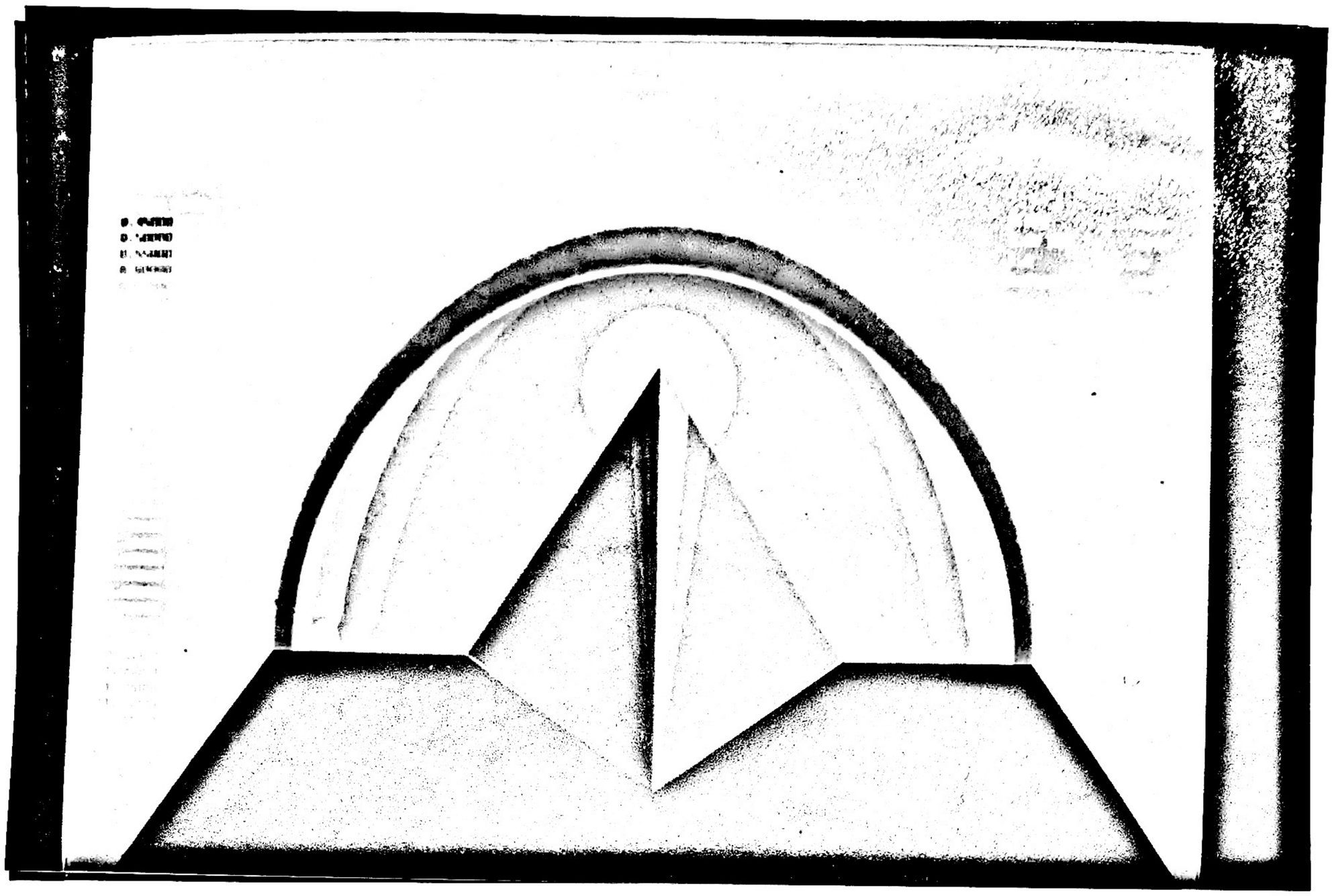


Fig. 22a. Density contours (green corresponds to free stream).

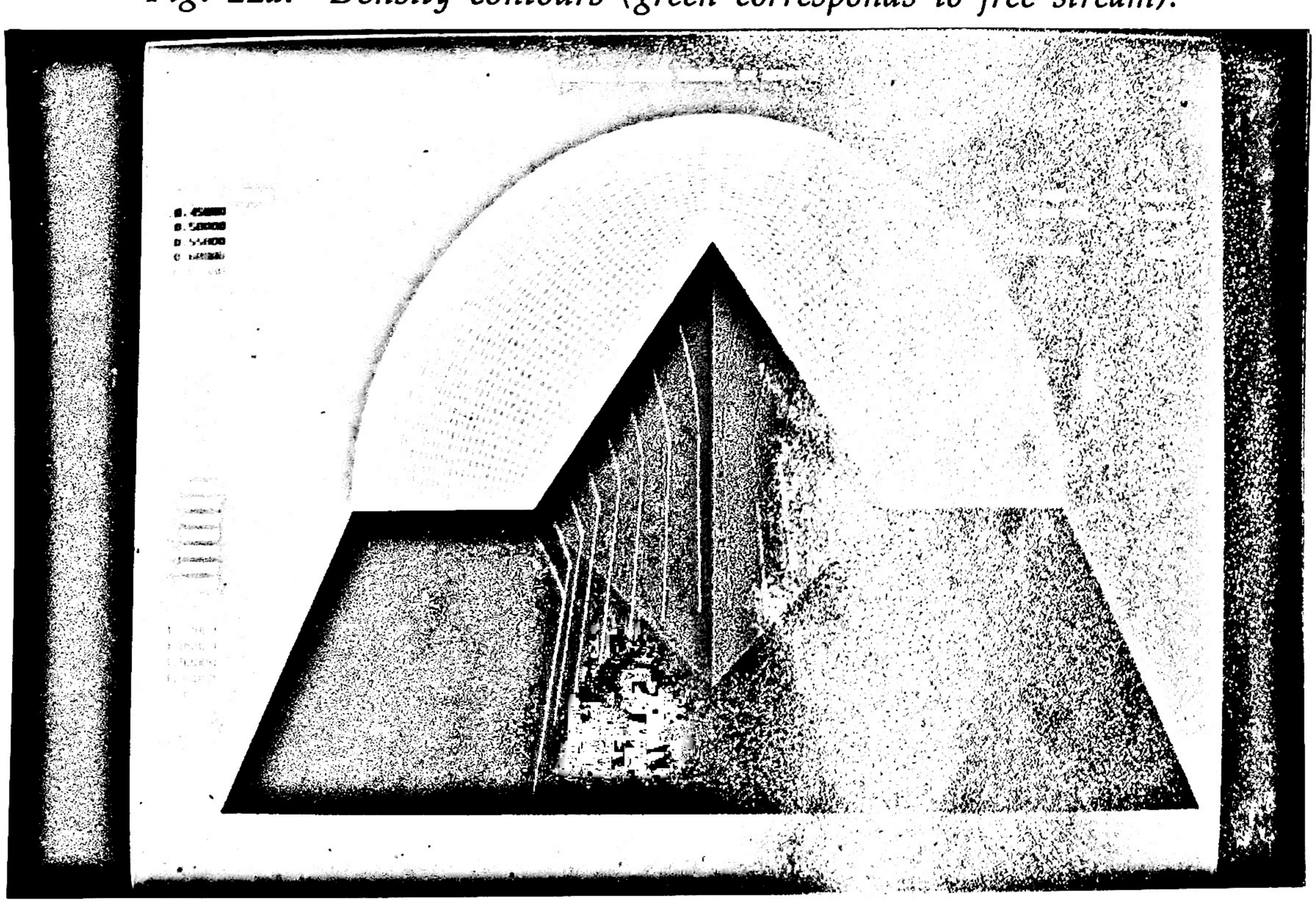
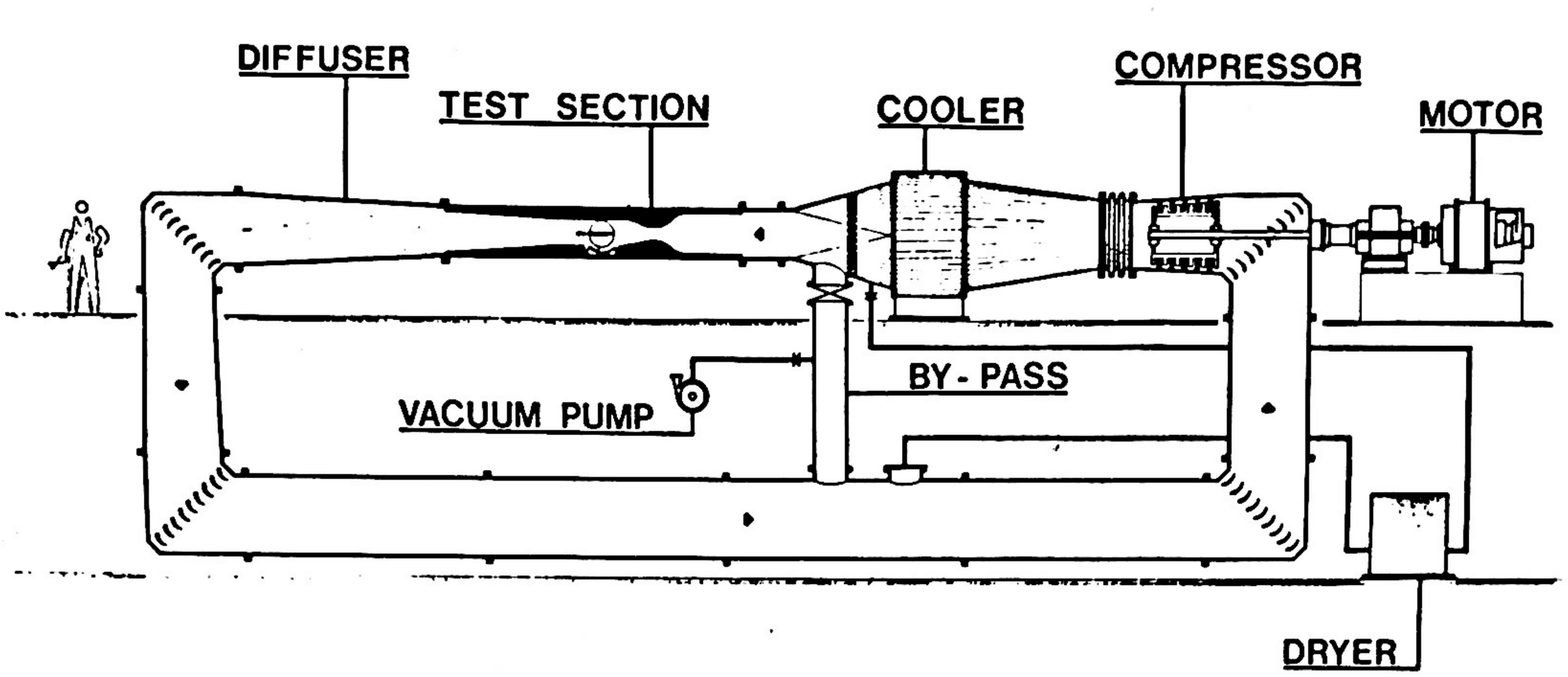


Fig. 22b. Particle traces colored by density of fluid.

Figure 22: Numerical solution of α=30°, θ=10° fin plotted on IRIS workstation using PLOT3D, illustrating conical nature of flow and location of grid.

Appendix 3 - The VKI S-1 Supersonic Tunnel

The VKI S-1 supersonic/transonic facility with a the flat plate currently being used is shown below.



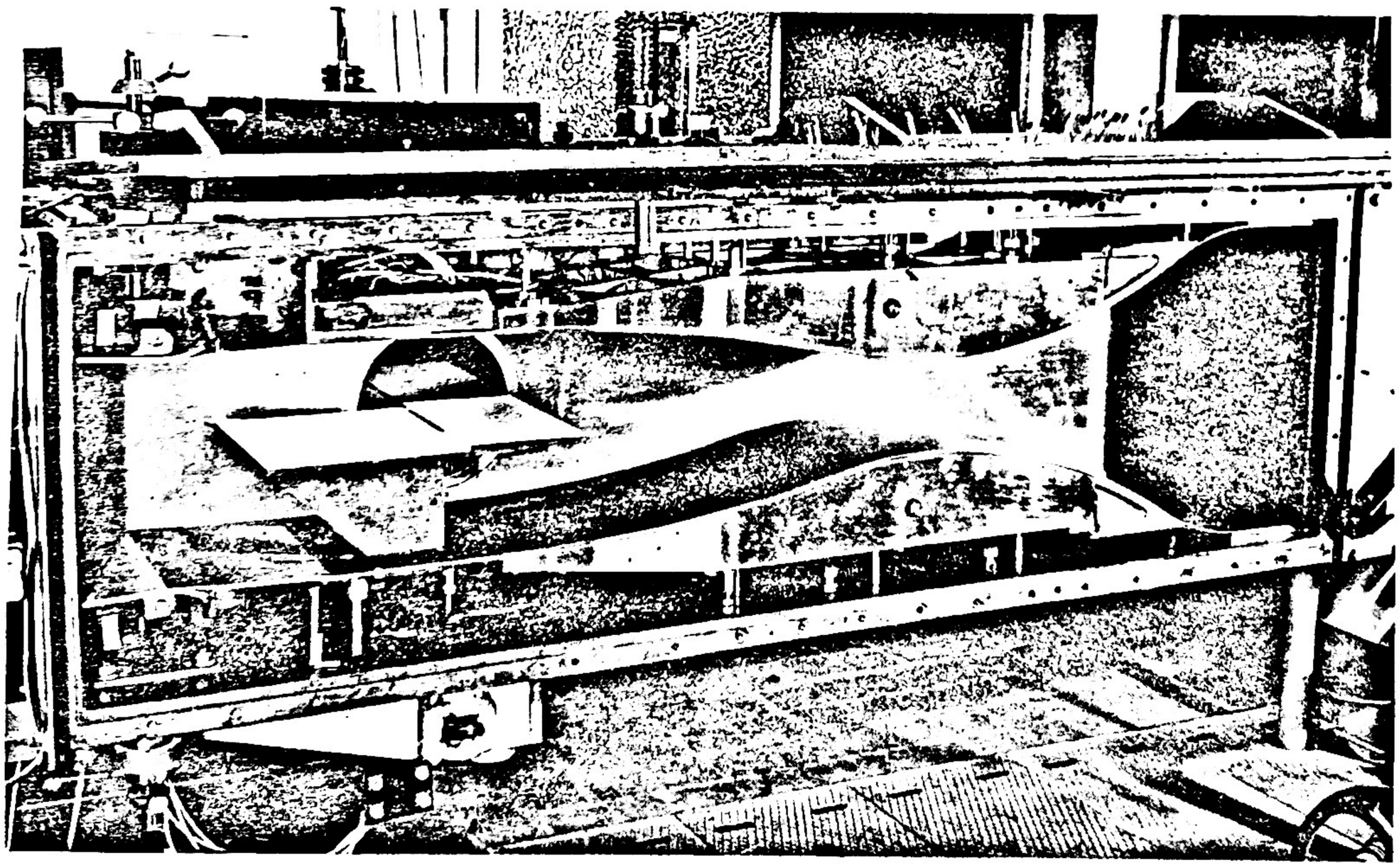


Figure 23: S-1.

Total conditions of T_t=296°K, P_t=100 mm Hg give a value of a unit Reynolds number in the test section of 2.0×10^6 per meter. It is known that transition starts at a free stream turbulence of 0.5% occurs at $Re > 3.5 \times 10^5$, and at $Re > 3 \times 10^6$ for smooth external flow[2]. These values imply the region of the boundary layer under consideration during this test was laminar.

Appendix 4 - The Laser Doppler Velocimeter

↑*if this bothers you, we can have it removed...*

The LDV measurements made in this test are intended to be of "benchmark" quality. It is hoped that they can be used for accurate validation of viscous 3-D numerical codes. To understand the limitations of the measurements made, a discussion is included here which describes how these measurements were taken.

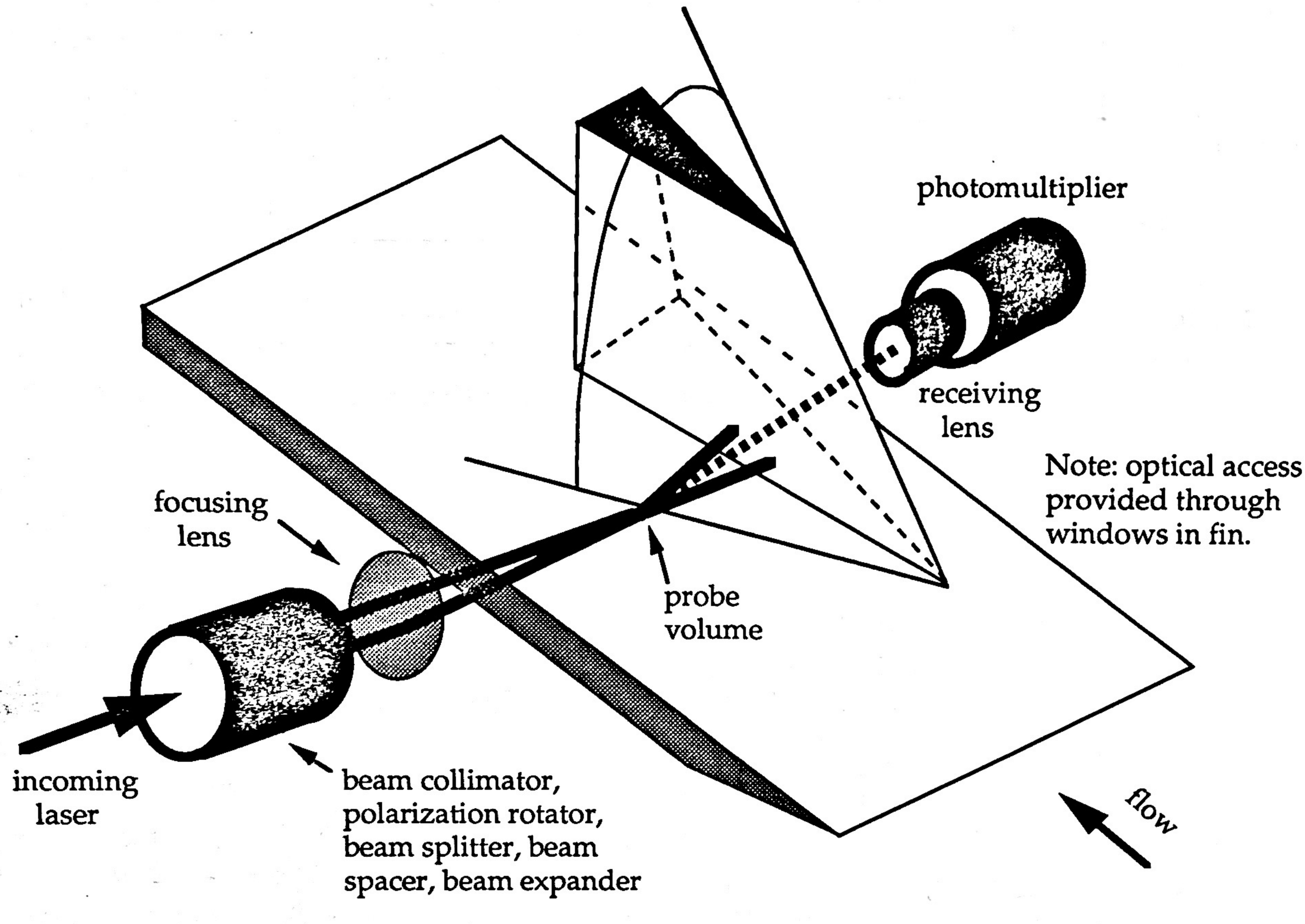


Figure 24: LDV system, oblique view.

The transmitting optics used are described below:

1. Beam collimator (TSI model 9108): A set of lenses which may be adjusted to minimize divergence of the beam with distance. A well-collimated beam is important so that the beams to reach a waist at the probe volume. If the beams do not reach a waist at the probe volume, the fringe spacing will be non-uniform, causing spreading of the Doppler signals, and the

probe volume will be bigger. Although the front end of the laser cavity is a planar partially silvered mirror, the opposite end is usually spherical, with a radius of curvature of a few meters, to aid the lasing process. Although correction lenses are used inside the laser cavity, the laser beam The collimator may be adjusted by reflecting the beam off a mirror placed on a far away wall back to a flat surface near the laser. Focusing of the collimator may be achieved by pulling (for coarse adjustment) and twisting (for fine adjustment) A schematic of a beam collimator is given in figure 25.

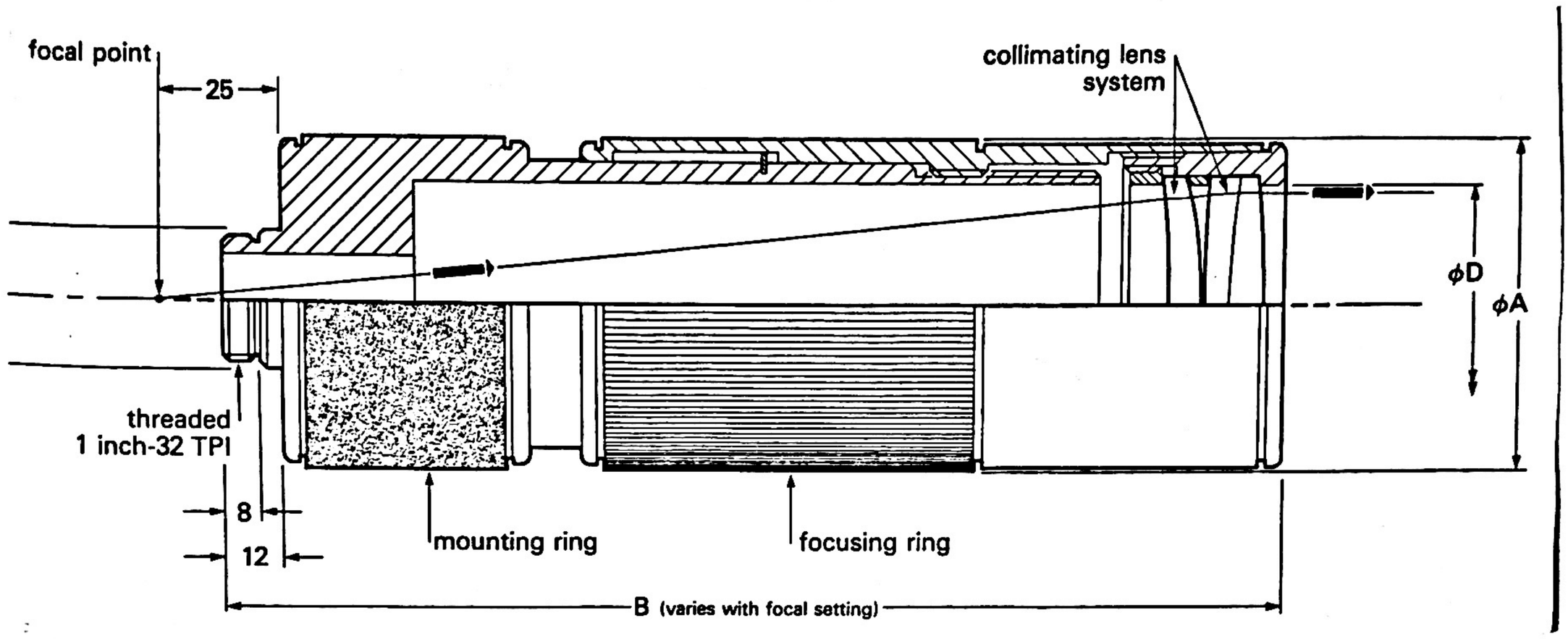


Figure 25: Schematic of beam collimator.

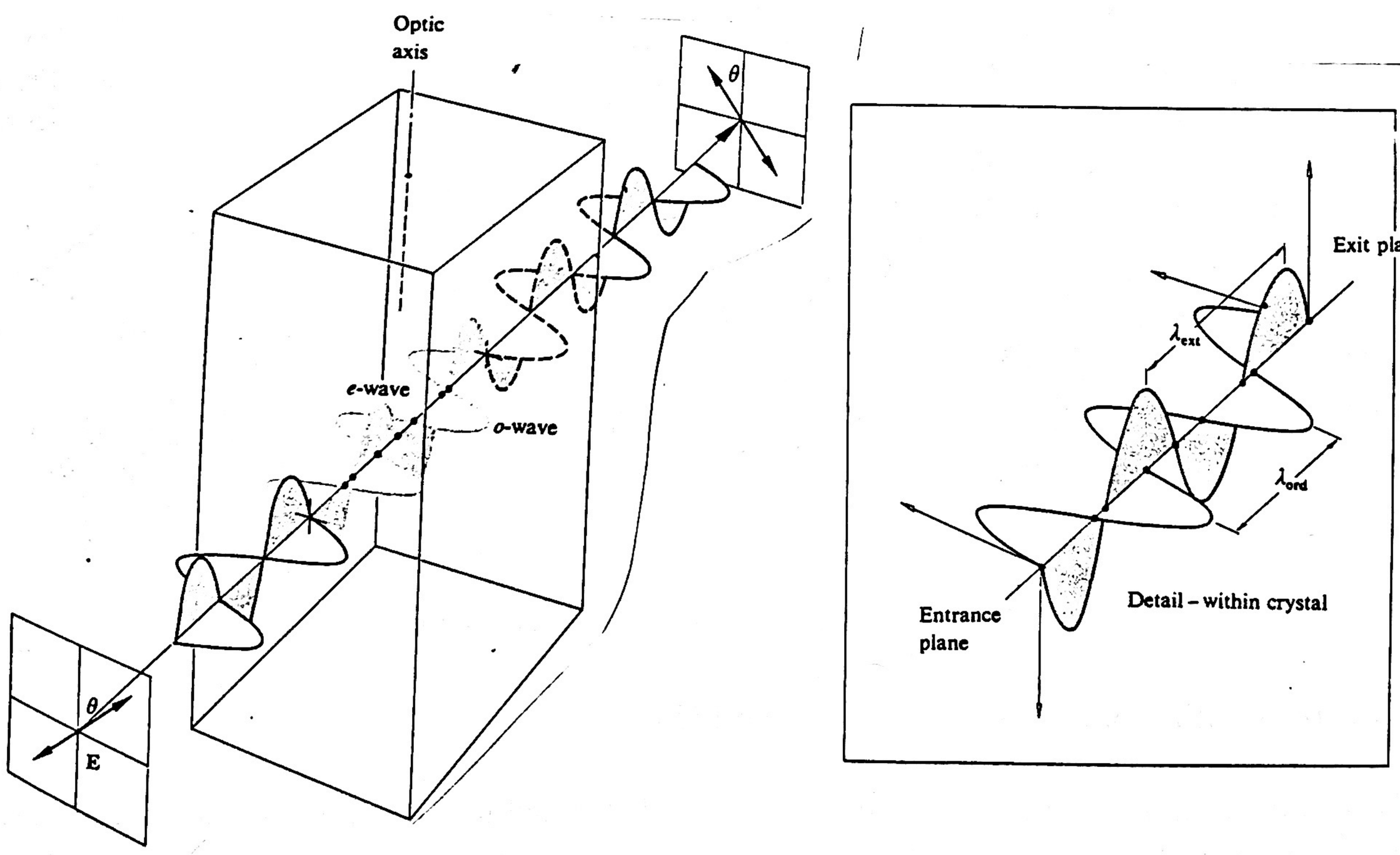


Figure 26: Operation of polarization rotator.

2. Polarization rotator: This is simply a half-wave plate that can be rotated. The material used is usually biaxial crystal mica. This material has a "fast axis" and a "slow axis", allowing light of one polarization to pass through faster. This has the effect of rotating the effective polarization of the incoming beam. Rotating the mica changes the amount of rotation produced on the polarization of the outgoing beam. This effect is illustrated in figure 26.

3. Beam splitter: This unit contains a partially silvered mirror and other mirrors which split the beam into two parallel beams spaced at 50 mm. The amount of power diverted into each beam depends on the polarization of the incoming beam. Thus, the polarization rotator is used to equalize the intensity of the beams leaving the beam splitter in order to produce the sharpest fringes at the probe volume.

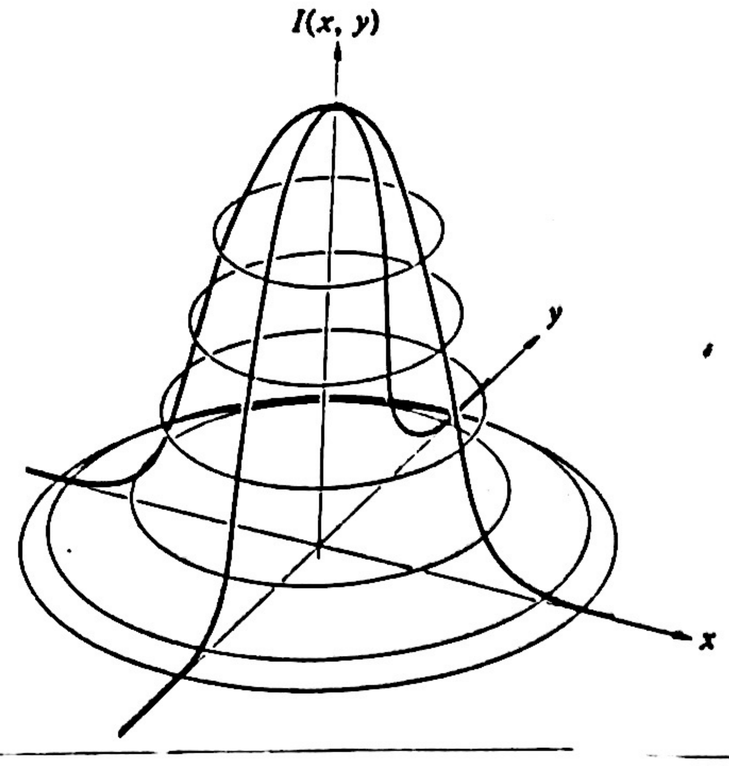
4. Beam spacer: four mirrors set to reduce the spacing of the beams to 22 mm to facilitate the use of the beam expander.

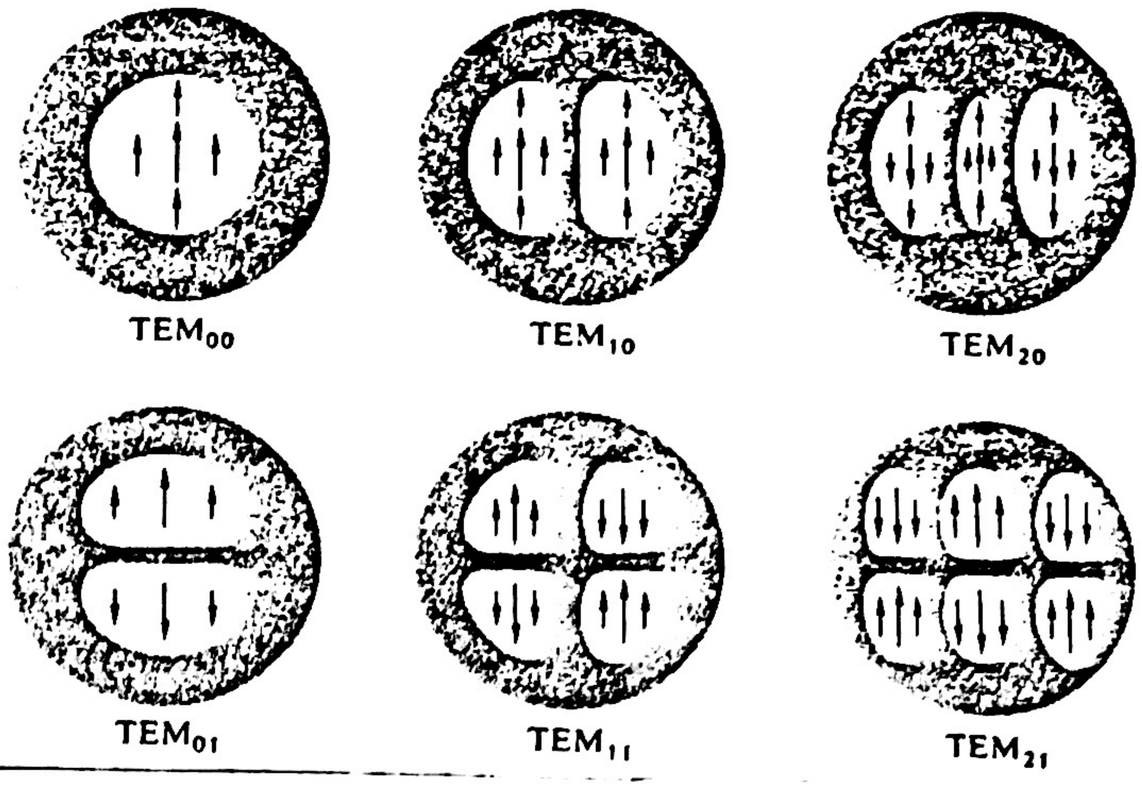
5. Beam expander (TSI Model 9188): A set of lenses which expands a collimated pair of incoming beams at 22 mm and results in a (still collimated) pair of beams at 50 mm at 2.27 times the cross-sectional area. The width of the probe volume is decreased significantly by this increased beam diameter.

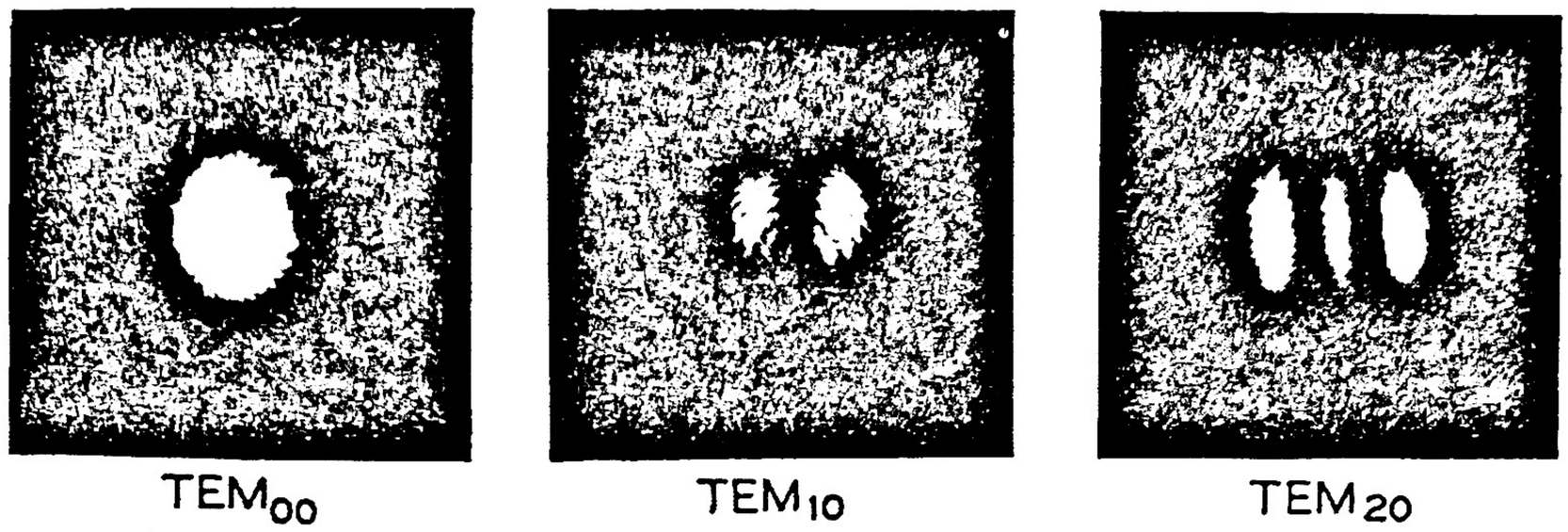
6. Focusing lens: A lens of focal length f=500 mm used to focus the parallel, expanded beams onto the probe volume.

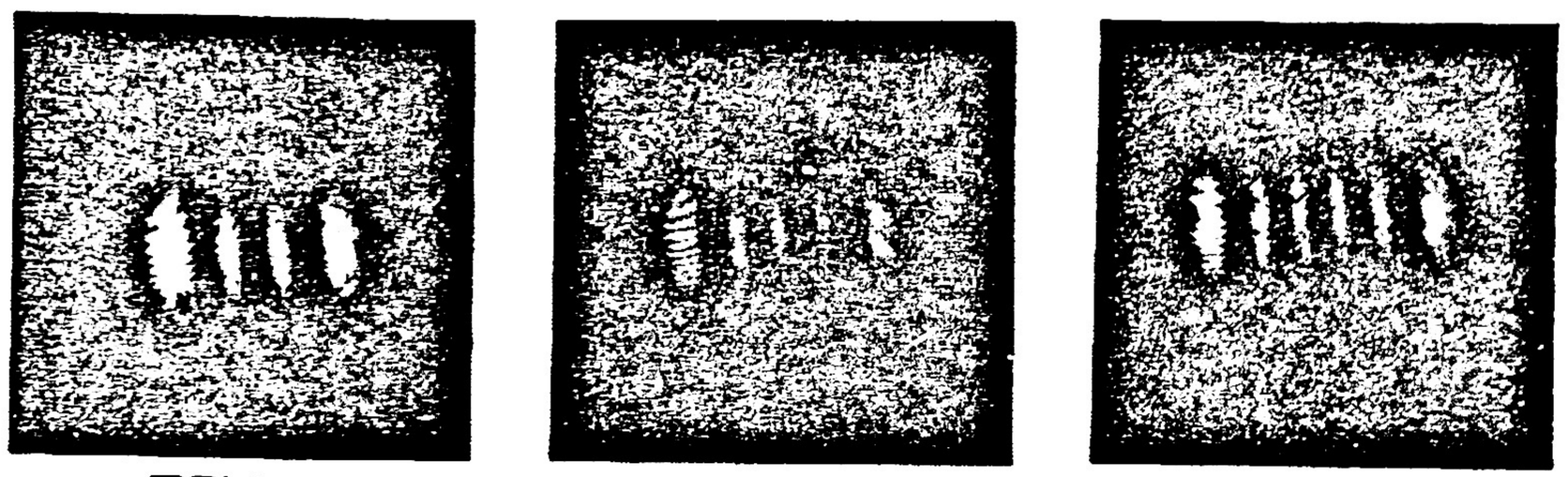
All optical surfaces must be kept quite clean, especially when operating at high laser powers when dirt on the optics can cause heating and pitting of the glass itself. Optics designed for use at high laser powers must be used.

Care must be taken that the laser operates in the TEM_{00} mode. This mode refers to the transverse electric and magnetic mode of oscillation in the laser cavity. The presence of longitudinal modes causes the the output of the laser to appear like spots (shown below) and destroys the spatial coherence of the laser critical to the formation of a proper fringe pattern at the probe volume. Ion lasers sometimes oscillate in complex longitudinal modes when their optical surfaces become soiled (due to normal operation) and must be cleaned and properly adjusted for best performance of the LDV system.









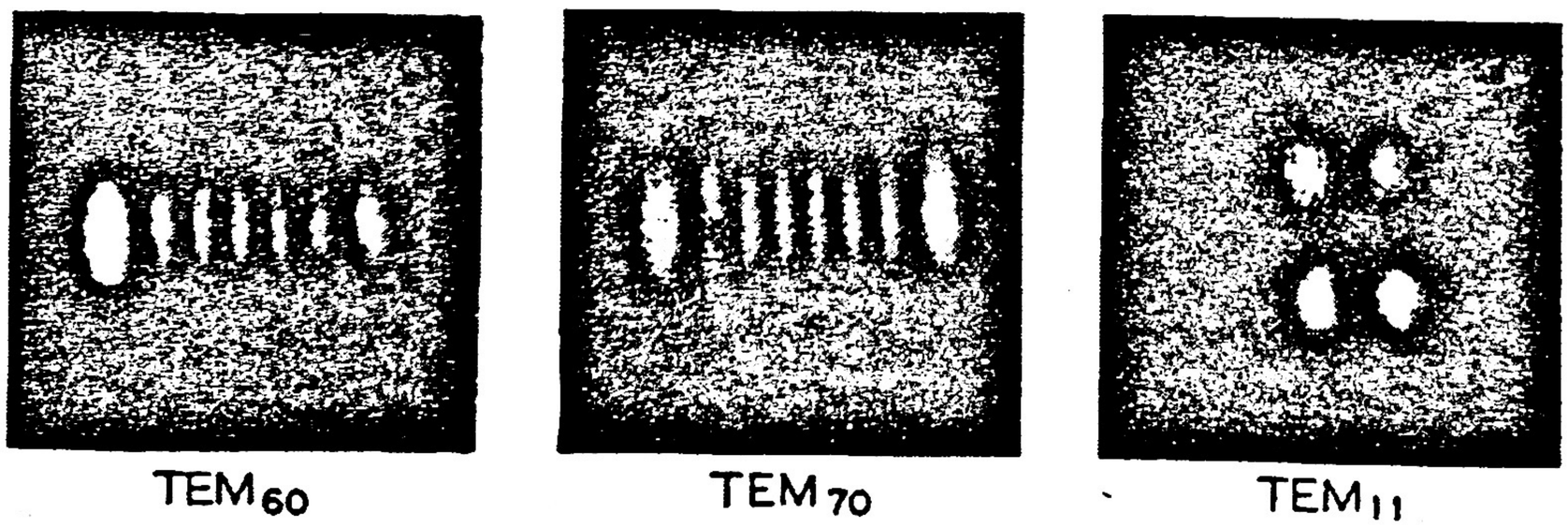


Figure 27: Operation of a laser in various TEM_{XX} modes.

The important equations governing the the LDV set up are:

$$d = \text{probe volume width} = \frac{4 f_1 \lambda}{\pi d_0}$$

$$l = \text{probe volume length} = \frac{d}{\tan \frac{\theta}{2}} = \frac{2 d f_1}{\delta}$$

$$h = \text{probe volume height} = d \cos \frac{\theta}{2} \approx d$$

$$d_f = \text{fringe spacing} = \frac{\lambda}{2 \sin \frac{\theta}{2}} = \frac{\lambda}{2 \sin\left(\arctan \frac{\delta}{2 f_1} \right)}$$

$$N_f = \text{Number of fringes in probe volume} = \frac{d}{d_f}$$

$$\nu \text{ (Hz)} = \text{output frequency} = \frac{\text{particle velocity}}{d_f}$$

The following quantities are known: $\lambda = 510\text{nm}$, $\delta = 50$ mm, $d_0 = 1.1$ mm. The angle θ, found both by projecting the beams through the probe volume onto a wall to measure the beam divergence and by calculating the convergence angle from the spacing and the focal length, was found to be 5.9°. By the above equations, the following quantities can be derived:

$f_1 = 498$ mm	$d_f = 4.91$ μm	$N_f = 17$
$d = 0.294$ mm	$l = 5.8$ mm	$h = 0.294$ mm

The laser beams were pointed down at the plate at a glancing angle of about 1°. This was done so that the zero point could be determined by watching where the beams finally hit the surface of the plate, and moving down until the measurement volume itself was on the wall. At this point, no measurements could be made, because the fringe pattern caused by the intersecting beams was disrupted by reflections from the surface. Slightly above this point, the measurement volume has an actual height (measured <u>normal</u> to the surface) of $h_{actual} = l \sin \alpha + d \cos \alpha$. The glancing angle was minimized for maximum sensitivity of the zero point determination method and minimum height increase of the measurement volume.

The shape of the probe volume itself is quite complex. It can be best visualized by taking two cardboard tubes (representing the extent of the Gaussian beams out to a certain intensity), cutting them with planar cuts at the proper angle, and fitting them together. This exercise

illustrates that the probe volume is elliptical in cross section looking from upstream, circular in cross section looking from the laser, and diamond in cross section looking from above. Figure 28 illustrates the intensity of the fringes in a horizontal plane of the probe volume.

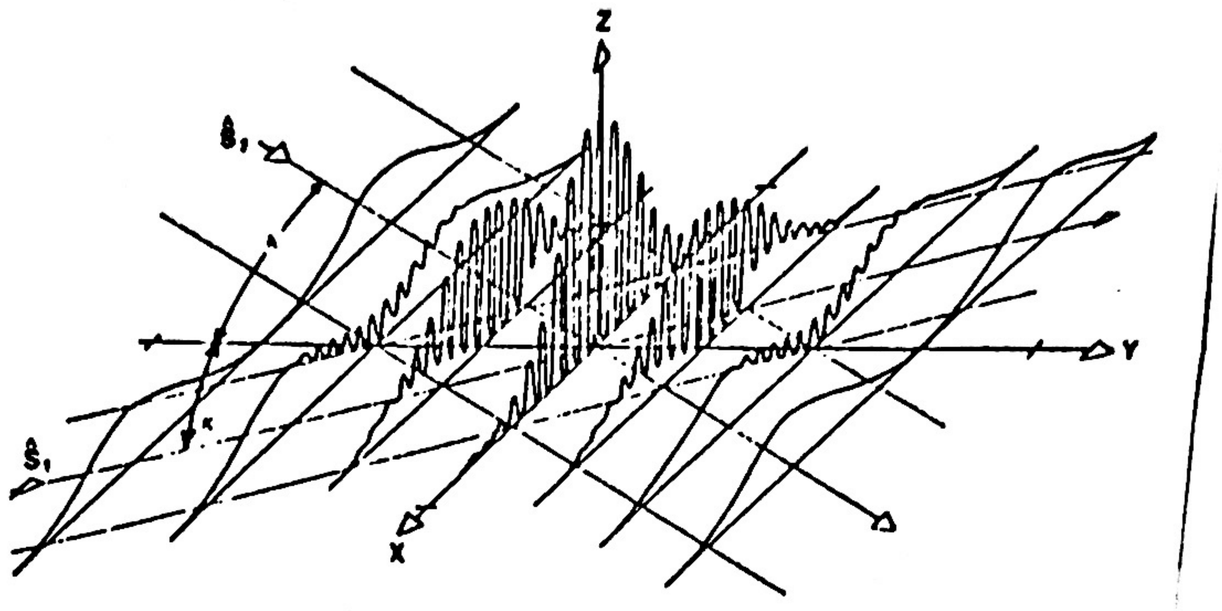


Figure 28: Probe Volume Fringes.

The most important effect of the finite size of the probe volume when measuring streamwise velocities in a boundary layer is the averaging over its height. The exact shape of the probe volume described above must carefully be taken into account in the analysis of the effective averaging. To simplify, use the "cardboard tube" analysis described above - the region in which both beams are strong enough to together produce a sharp enough fringe for detection defines the extent of the probe volume. The fact that a minimum number of these fringes must be counted for a valid measurement further decreases the"effective" probe volume size. Note that in the boundary layer all velocities are approximately parallel to the wall.

It is usually assumed that the effective seeding is uniform over the entire boundary layer and that the electronics are equally sensitive to all frequencies. This is certainly an idealization; the accuracy of such an assumption would be an interesting topic of investigation.

The zero point determination was made with the tunnel off. Turning the tunnel on changed the pressure by about 1 atmosphere, which changed the index of refraction of the air in the tunnel from **n=1.000293** to **n≈1.0**. At a glancing angle of 1° and a distance from window to the measurement volume of 30 cm from the window, this causes a change in height of the measurement volume of 2 μm. This is insignificant. However, the index of refraction of the glass windows, which are about 1 cm thick, is about **n≈1.6**. Closing the windows after the zero point determination is made changes the angle that the beams pass through the glass and causes a significant deflection of the beams. Thus, all zero point calibrations must be made with the windows closed.

The receiving optics used a camera lens to focus the image of the probe volume on a pinhole placed directly in front of the photomultiplier. To properly shield unwanted light from the

photomultiplier, a pinhole was selected whose image diameter in the plane of the probe volume d_w is approximately equal to the diameter of the probe volume d itself. Let: p = the distance from the probe volume to the receiving lens, q = the distance from the receiving lens to the pinhole, d_p = the diameter of the pinhole, and f = the focal length of the receiving lens. The governing equations for selection of the pinhole size are:

$$\frac{1}{p}+\frac{1}{q}=\frac{1}{f}$$

$$d_w = d_p \cdot \frac{p}{q} = d_p \cdot \left(\frac{p}{f} - 1\right)$$

The zoom lens used in the receiving optics was set to a focal length of $f = 90$ mm. A spacer had to be used between the lens and the photomultiplier to facilitate the short focusing distance. A pinhole was selected with a diameter $d_p = 100$ μm. The focusing distance was approximately $p = 300$ mm. This gives an image diameter of the pinhole in the plane of the probe volume of $d_w = 0.23$ mm. Thus the selected pinhole satisfies the criterion mentioned previously. It was found that very careful alignment of the image of the probe volume on the pinhole was the most critical and the most difficult adjustment of the LDV system.

A high frequency oscilloscope (20 ns per division at its highest sweep speed) was required to view the Doppler bursts. Quite clean images could be obtained when triggering on the filtered output of the signal processor. 50 ohm terminators were required at the end of all BNC cables connected to the oscilloscope to prevent reflections of the signal off the terminal back to the signal processor. Such reflections can be significant when working at very high frequencies.

A bandpass filter was used to reduce the extraneous signals sent to the LDV processor. The shoulder of the high pass filter should be set to less than half of the lowest frequency (corresponding to the lowest velocity one expects to measure in the boundary layer - this may have to be changed during the test as one approaches the wall). The shoulder of the low pass filter should be set to about twice the highest frequency (corresponding to velocity of the free stream). By exceeding these limits, one might simply be processing narrowly filtered noise which looks significant but is actually bogus.

The TSI model 1990 Laser Doppler Counter was used in this test. The bandpass filter was set to pass frequencies between 5 MHz and 200 MHz; the free stream velocity of 500 m/s gave an expected frequency of 100 MHz. The amplitude limiter was set to 20 to eliminate the unwanted strong signals caused by the unavoidable presence of conglomerated particles and drops of water formed by condensation on the sides of the injection probe. This limiter should be set as low as possible while maintaining a sufficient data rate to eliminate these spurious signals.

Appendix 5 - Solution of the Chapman and Rubesin Variables

The undisturbed laminar boundary layer considered in this project is described quite well by the Chapman and Rubesin boundary layer equations given in Section 4.3.4. The following program was written to solve the variables in these equations. It uses a relaxation method (described in Ref. [30]) to solve the ordinary differential equations with two boundary value points to find f, r, and Y. Some subroutines, taken directly from Ref. [30], are omitted for clarity.

Following the code is a table of values of the variables in the Chapman and Rubesin equations as found by this program.

```
PROGRAM ChapmanRubesin(Input,output);

USES  MemTypes, QuickDraw, OSIntF, ToolIntf;

LABEL 99;

CONST  nemax=3;  mmax=401;  ncimax=3; ncjmax=3;  nckmax=402;
       nsimax=3;  nsjmax=7;  Pr=0.72;

TYPE
   glyarray = ARRAY [1..nemax,1..mmax] OF real;
   glcarray = ARRAY [1..ncimax,1..ncjmax,1..nckmax] OF real;
   glsarray = ARRAY [1..nsimax,1..nsjmax] OF real;
   glscalv = ARRAY [1..nemax] OF real;
   VariableRec = record
      x,f,df,d2f,r,dr,y,dy :real;
      end;

VAR
   i,j,k,itmax,m                          : integer;
   h,a                                    : real;
   conv,deriv,fac1,fac2                   : real;
   q1,slowc                               : real;
   scalv                                  : glscalv;
   f                                      : ARRAY [1..3,1..mmax] OF real;
   r,y                                    : ARRAY [1..2,1..mmax] OF real;
   c                                      : glcarray;
   s                                      : glsarray;
   x                                      : ARRAY [1..mmax] OF real;
   ne,nb,nsi,nyj,nyk,nci,ncj,
   nck,nsj,dvar                           : integer;
   Variable                               : VariableRec;
   VariableFile                           : file of VariableRec;

PROCEDURE writescreen;
VAR i,j:integer;
BEGIN
   writeln;
   writeln('i':3,'f':9,'f''':8,'f"':8,
           'r':9,'r''':9,'y':9,'y''':9);
```

```
    FOR j := 0 to 5 DO BEGIN
        i := (j*(m-1) div 5) +1;
        WRITELN(j:3,f[1,i]:9:5,f[2,i]:8:5,f[3,i]:8:5,
                    r[2,i]:9:5,r[1,i]:9:5,y[1,i]:9:5,y[2,i]:9:5);
        END;
END;

PROCEDURE writefile;
VAR i,j:integer;
BEGIN
    Rewrite(VariableFile,'ChapmanRubesin.out');
    FOR j := 0 to 50 DO BEGIN
        i := (j*(m-1) div 50) +1;
        Variable.x:=(i-1)/80;
        Variable.f:=f[1,i];
        Variable.df:=f[2,i];
        Variable.d2f:=f[3,i];
        Variable.r:=r[2,i];
        Variable.dr:=r[1,i];
        Variable.y:=y[1,i];
        Variable.dy:=y[2,i];
        write(VariableFile,Variable);
        END;
    Close(VariableFile);
END;

PROCEDURE red(iz1,iz2,jz1,jz2,jm1,jm2,jmf,ic1,jc1,jcf,kc: integer;
          c: glcarray; nci,ncj,nck: integer;
          VAR s: glsarray; nsi,nsj: integer);
...Taken directly from Numerical Recipes.

PROCEDURE pinvs(ie1,ie2,je1,jsf,jc1,k: integer; VAR c: glcarray;
        nci,ncj,nck: integer; VAR s: glsarray; nsi,nsj: integer);
...Taken directly from Numerical Recipes.

PROCEDURE bksub(ne,nb,jf,k1,k2: integer; VAR c: glcarray;
        nci,ncj,nck: integer);
...Taken directly from Numerical Recipes.

PROCEDURE difeq(k,k1,k2,jsf,is1,isf,dvar: integer;
        ne: integer; VAR s: glsarray; nsi,nsj: integer);
VAR     temp,temp1: real;
BEGIN
    IF (dvar = 1) THEN BEGIN
        IF (k = k1) THEN BEGIN
            s[2,4] := 1.0;
        s[2,5] := 0.0;
        s[2,6] := 0.0;
        s[2,jsf] := f[1,1];
        s[3,4] := 0.0;
        s[3,5] := 1.0;
        s[3,6] := 0.0;
        s[3,jsf] := f[2,1]
        END
ELSE IF (k > k2) THEN BEGIN
    s[1,4] := 0.0;
    s[1,5] := 1.0;
    s[1,6] := 0.0;
```

```
      s[1,jsf] := f[2,M]-2
      END
   ELSE BEGIN
      s[1,1] := -1.0;
      s[1,2] := -0.5*h;
      s[1,3] := 0.0;
      s[1,4] := 1.0;
      s[1,5] := -0.5*h;
      s[1,6] := 0.0;
      s[2,1] := 0.0;
      s[2,2] := -1.0;
      s[2,3] := -0.5*h;
      s[2,4] := 0.0;
      s[2,5] := 1.0;
      s[2,6] := -0.5*h;
      s[3,1] := 0.25*h*(f[3,k]+f[3,k-1]);
      s[3,2] := 0.0;
      s[3,3] := 0.25*h*(f[1,k]+f[1,k-1])-1;
      s[3,4] := s[3,1];
      s[3,5] := 0.0;
      s[3,6] := s[3,3]+2;
      s[1,jsf] := f[1,k]-f[1,k-1]-0.5*h*(f[2,k]+f[2,k-1]);
      s[2,jsf] := f[2,k]-f[2,k-1]-0.5*h*(f[3,k]+f[3,k-1]);
      s[3,jsf] := f[3,k]-f[3,k-1]+
                  0.25*h*(f[3,k]+f[3,k-1])*(f[1,k]+f[1,k-1])
      END
   END
ELSE IF (dvar = 2) THEN BEGIN
   IF (k = k1) THEN BEGIN
      s[2,3] := 1.0;
      s[2,4] := 0.0;
      s[2,jsf] := r[1,1]
      END
   ELSE IF (k > k2) THEN BEGIN
      s[1,3] := 0.0;
      s[1,4] := 1.0;
      s[1,jsf] := r[2,M]
      END
   ELSE BEGIN
      s[1,1] := -0.5*h;
      s[1,2] := -1.0;
      s[1,3] := -0.5*h;
      s[1,4] := 1.0;
      temp:=(f[1,k-1]+f[1,k])*0.5+(f[2,k-1]-f[2,k])*0.25*h;
      temp1:=(f[3,k-1]+f[3,k])*0.5;
      s[2,1] := -1.0+Pr*0.5*h*temp;
      s[2,2] := 0.0;
      s[2,3] := s[2,1]+2.0;
      s[2,4] := 0.0;
      s[1,jsf] := r[2,k]-r[2,k-1]-0.5*h*(r[1,k]+r[1,k-1]);
      s[2,jsf] := r[1,k]-r[1,k-1]+
                  Pr*0.5*h*(temp*(r[1,k]+r[1,k-1])+temp1*temp1)
      END
   END
ELSE BEGIN
   IF (k = k1) THEN BEGIN
      s[2,3] := 1.0;
      s[2,4] := 0.0;
```

```
    s[2,jsf] := y[1,1]-1
    END
ELSE IF (k > k2) THEN BEGIN
    s[1,3] := 1.0;
    s[1,4] := 0.0;
    s[1,jsf] := y[1,M]
    END
ELSE BEGIN
    s[1,1] := -1.0;
    s[1,2] := -0.5*h;
    s[1,3] := 1.0;
    s[1,4] := -0.5*h;
    temp:=(f[1,k-1]+f[1,k])*0.5+(f[2,k-1]-f[2,k])*0.25*h;
    s[2,1] := 0.0;
    s[2,2] := -1.0+Pr*0.5*h*temp;
    s[2,3] := 0.0;
    s[2,4] := s[2,2]+2.0;
    s[1,jsf] := y[1,k]-y[1,k-1]-0.5*h*(y[2,k]+y[2,k-1]);
    s[2,jsf] := y[2,k]-y[2,k-1]+
                Pr*0.5*h*temp*(y[2,k]+y[2,k-1])
    END
  END
END;

PROCEDURE solvde(itmax: integer; conv,slowc: real; scalv: glscalv;
        dvar,ne,nb,m: integer; nyj,nyk: integer; VAR c: glcarray;
        nci,ncj,nck: integer; VAR s: glsarray; nsi,nsj: integer);
...Taken directly from Numerical Recipes.

BEGIN     { main program }

{ initialize all variables here }
   m:=51;
   h := 5.0 / (m-1);
   FOR i := 1 to m DO BEGIN
      f[1,i]:=0.0;
      f[2,i]:=0.0;
      f[3,i]:=0.0;
      r[1,i]:=0.0;
      r[2,i]:=0.0;
      y[1,i]:=0.0;
      y[2,i]:=0.0;
   END;
   scalv[1]:=1.0;
   scalv[2]:=1.0;
   scalv[3]:=1.0;
   itmax := 40;
   conv  := 5.0e-6;
   slowc := 1.0;
   FOR i:=1 to 2 DO BEGIN

{ relaxation for f }
      ne:=3;   nb:=2;   nsi:=ne;   nyj:=ne;   nyk:=m;   nci:=ne;
      ncj:=ne-nb+1;     nck:=m+1;     nsj:=2*ne+1;   dvar:=1;
      writescreen;
      solvde(itmax,conv,slowc,scalv,dvar,ne,nb,m,nyj,nyk,
         c,nci,ncj,nck,s,nsi,nsj);
```

```
{ relaxation for r }
      ne:=2;   nb:=1;   nsi:=ne;   nyj:=ne;   nci:=ne;
      ncj:=ne-nb+1;     nsj:=2*ne+1;   dvar:=2;
      writescreen;
      solvde(itmax,conv,slowc,scalv,dvar,ne,nb,m,nyj,nyk,
         c,nci,ncj,nck,s,nsi,nsj);

{ relaxation for Y }
      dvar:=3;
      writescreen;
      solvde(itmax,conv,slowc,scalv,dvar,ne,nb,m,nyj,nyk,
         c,nci,ncj,nck,s,nsi,nsj);
```

```
{ increase the density of the grid by factor of eight }
      IF (i = 1) THEN BEGIN
         writeln;  writeln('Performing grid refinement ...');
         FOR j:=m-1 downto 1 DO BEGIN
            FOR k:=8 downto 1 DO BEGIN
               f[1,(j-1)*8+k+1]:=(f[1,j]*(8-k)+f[1,j+1]*k)/8.0;
               f[2,(j-1)*8+k+1]:=(f[2,j]*(8-k)+f[2,j+1]*k)/8.0;
               f[3,(j-1)*8+k+1]:=(f[3,j]*(8-k)+f[3,j+1]*k)/8.0;
               r[1,(j-1)*8+k+1]:=(r[1,j]*(8-k)+r[1,j+1]*k)/8.0;
               r[2,(j-1)*8+k+1]:=(r[2,j]*(8-k)+r[2,j+1]*k)/8.0;
               y[1,(j-1)*8+k+1]:=(y[1,j]*(8-k)+y[1,j+1]*k)/8.0;
               y[2,(j-1)*8+k+1]:=(y[2,j]*(8-k)+y[2,j+1]*k)/8.0;
               END
            END;
         m:=(m-1)*8+1;
         h := 5.0 / (m-1);
         conv  := 1.0e-6;
         writeln;  writeln(' m = ',m:3,'     h = ',h:5:4);
         END
      END;

   writescreen;
   writefile;
   writeln('Finished.');        readln;
END.
```

x	f	f'	f"	r	r'	y	y'
0.0	0.00000	0.00000	1.32826	0.84772	0.00000	1.00000	-0.59126
0.1	0.00664	0.13282	1.32797	0.84455	-0.06350	0.94088	-0.59117
0.2	0.02656	0.26553	1.32591	0.83503	-0.12679	0.88178	-0.59051
0.3	0.05974	0.39788	1.32034	0.81921	-0.18936	0.82281	-0.58873
0.4	0.10611	0.52943	1.30958	0.79721	-0.25034	0.76409	-0.58527
0.5	0.16557	0.65957	1.29205	0.76924	-0.30859	0.70583	-0.57962
0.6	0.23795	0.78756	1.26637	0.73563	-0.36268	0.64826	-0.57131
0.7	0.32299	0.91254	1.23148	0.69689	-0.41110	0.59167	-0.55993
0.8	0.42033	1.03353	1.18667	0.65366	-0.45224	0.53639	-0.54519
0.9	0.52952	1.14953	1.13173	0.60674	-0.48466	0.48275	-0.52690
1.0	0.65003	1.25954	1.06701	0.55706	-0.50717	0.43113	-0.50503
1.1	0.78120	1.36263	0.99341	0.50566	-0.51898	0.38186	-0.47970
1.2	0.92230	1.45797	0.91237	0.45363	-0.51985	0.33530	-0.45119
1.3	1.07251	1.54492	0.82582	0.40205	-0.51008	0.29172	-0.41995
1.4	1.23098	1.62303	0.73602	0.35194	-0.49056	0.25138	-0.38654
1.5	1.39681	1.69210	0.64543	0.30422	-0.46266	0.21446	-0.35167
1.6	1.56910	1.75217	0.55650	0.25964	-0.42812	0.18107	-0.31607
1.7	1.74695	1.80353	0.47149	0.21875	-0.38889	0.15124	-0.28051
1.8	1.92953	1.84667	0.39233	0.18195	-0.34695	0.12494	-0.24574
1.9	2.11603	1.88224	0.32049	0.14939	-0.30416	0.10205	-0.21244
2.0	2.30575	1.91104	0.25692	0.12109	-0.26216	0.08239	-0.18118
2.1	2.49804	1.93392	0.20206	0.09689	-0.22225	0.06573	-0.15241
2.2	2.69236	1.95175	0.15587	0.07654	-0.18541	0.05181	-0.12643
2.3	2.88825	1.96537	0.11792	0.05968	-0.15227	0.04034	-0.10342
2.4	3.08532	1.97558	0.08747	0.04595	-0.12314	0.03103	-0.08341
2.5	3.28328	1.98309	0.06361	0.03492	-0.09809	0.02356	-0.06632
2.6	3.48187	1.98849	0.04536	0.02620	-0.07698	0.01767	-0.05198
2.7	3.68092	1.99231	0.03170	0.01940	-0.05953	0.01308	-0.04017
2.8	3.88029	1.99496	0.02172	0.01418	-0.04536	0.00956	-0.03059
2.9	4.07989	1.99675	0.01459	0.01023	-0.03407	0.00690	-0.02297
3.0	4.27962	1.99795	0.00960	0.00729	-0.02522	0.00491	-0.01700
3.1	4.47946	1.99873	0.00620	0.00512	-0.01840	0.00345	-0.01240
3.2	4.67936	1.99922	0.00392	0.00355	-0.01323	0.00239	-0.00892
3.3	4.87930	1.99954	0.00243	0.00243	-0.00938	0.00164	-0.00632
3.4	5.07926	1.99973	0.00148	0.00164	-0.00655	0.00111	-0.00442
3.5	5.27924	1.99984	0.00088	0.00109	-0.00451	0.00074	-0.00304
3.6	5.47923	1.99991	0.00051	0.00072	-0.00306	0.00048	-0.00206
3.7	5.67922	1.99995	0.00029	0.00047	-0.00205	0.00031	-0.00138
3.8	5.87922	1.99997	0.00016	0.00030	-0.00135	0.00020	-0.00091
3.9	6.07922	1.99999	0.00009	0.00019	-0.00088	0.00013	-0.00059
4.0	6.27922	1.99999	0.00005	0.00012	-0.00056	0.00008	-0.00038
4.1	6.47922	2.00000	0.00003	0.00007	-0.00036	0.00005	-0.00024
4.2	6.67922	2.00000	0.00001	0.00004	-0.00022	0.00003	-0.00015
4.3	6.87922	2.00000	0.00001	0.00003	-0.00014	0.00002	-0.00009
4.4	7.07922	2.00000	0.00000	0.00001	-0.00008	0.00001	-0.00006
4.5	7.27922	2.00000	0.00000	0.00001	-0.00005	0.00001	-0.00003
4.6	7.47922	2.00000	0.00000	0.00000	-0.00003	0.00000	-0.00002
4.7	7.67922	2.00000	0.00000	0.00000	-0.00002	0.00000	-0.00001
4.8	7.87922	2.00000	0.00000	0.00000	-0.00001	0.00000	-0.00001
4.9	8.07922	2.00000	0.00000	0.00000	-0.00001	0.00000	0.00000
5.0	8.27922	2.00000	0.00000	0.00000	0.00000	0.00000	0.00000

Table 2. Selected values of the Chapman and Rubesin variables

Appendix 6 - Error Propagation of a Linear Regression Fit

The following analysis was made in conjunction with a lab class at the VKI. Although it is not use in this report, it is a very important analysis and is thus included here as a reference.

Consider the problem of fitting N data points to the straight-line model y=a+bx. One merit function describing how well this data fits a straight line is the linear correlation coefficient, given by the formula:

$$r = \frac{\sum_{i=1}^{N} (x_i - \bar{x})(y_i - \bar{y})}{\sqrt{\sum_{i=1}^{N} (x_i - \bar{x})^2} \sqrt{\sum_{i=1}^{N} (y_i - \bar{y})^2}}$$

The value of r^2 is one for complete correlation (exactly linear) and near zero for a shotgun blast, and is a useful, standard way to describe the accuracy of a linear model.

Now, assume that the x_i are known exactly, and each of the values y_i has associated with it an uncertainty ω_i at a certain confidence level (2:1 for the standard deviation of a binormal probability, 10 to 20:1 for the description of experimental uncertainty used in the Kline and McClintock model.) Then, to solve for the straight line, it becomes useful to use the chi-squared merit function, given by:

$$\chi^2 (a,b) = \sum_{i=1}^{N} \left(\frac{y_i - a - b x_i}{\omega_i} \right)^2$$

It can be seen that the value of χ^2 is zero for a perfect fit of y=a+bx to the data, and greater than zero as points y_i deviate from this line, with the deviation weighted at each point by the reciprocal its associated uncertainty ω_i. To find the best fit, χ^2 is minimized. At its minimum, the derivatives of χ^2 with respect to a and b vanish - thus:

$$0 = \frac{\partial \chi^2}{\partial a} = -2 \sum_{i=1}^{N} \frac{y_i - a - b x_i}{\omega_i^2} \qquad 0 = \frac{\partial \chi^2}{\partial b} = -2 \sum_{i=1}^{N} \frac{x_i (y_i - a - b x_i)}{\omega_i^2}$$

It now becomes useful to make use of the new variables:

$$S \equiv \sum_{i=1}^{N} \frac{1}{\omega_i^2} \qquad S_x \equiv \sum_{i=1}^{N} \frac{x_i}{\omega_i^2} \qquad S_y \equiv \sum_{i=1}^{N} \frac{y_i}{\omega_i^2}$$

$$S_{xx} \equiv \sum_{i=1}^{N} \frac{x_i^2}{\omega_i^2} \qquad S_{xy} \equiv \sum_{i=1}^{N} \frac{x_i y_i}{\omega_i^2} \qquad \Delta \equiv S S_{xx} - (S_x)^2$$

The equations for the vanishing derivatives of χ^2 become

$$S_y - a S - b S_x = 0 \qquad S_{xy} - a S_x - b S_{xx} = 0$$

or, rearranged,

$$a = \frac{S_{xx} S_y - S_x S_{xy}}{\Delta} \qquad b = \frac{S S_{xy} - S_x S_y}{\Delta}$$

Finally, to see how the uncertainties ω_i propagate into the coefficients a and b, the derivatives of the computed values of a and b are computed with respect to each of the variables y_i:

$$\frac{\partial a}{\partial y_i} = \frac{S_{xx} - S_x x_i}{\omega_i^2 \Delta} \qquad \frac{\partial b}{\partial y_i} = \frac{S x_i - S_x}{\omega_i^2 \Delta}$$

and substituted into the error propagation equation quoted by Kline and McClintock:

$$(\omega_a)^2 = \sum_{i=1}^{N} (\omega_i)^2 \left(\frac{\partial a}{\partial y_i}\right)^2 \qquad (\omega_b)^2 = \sum_{i=1}^{N} (\omega_i)^2 \left(\frac{\partial b}{\partial y_i}\right)^2$$

Combining these expressions, summing over i, and again applying the definitions for the S expressions, it is easily seen that:

$$(\omega_a)^2 = S_{xx} / \Delta$$

$$(\omega_b)^2 = S / \Delta$$

These are the desired expressions for the uncertainties of the coefficients a and b of the linear regression fit.

Bibliography

(arranged in chronological order by subject)

Classical Boundary Layer Theory

[1]Chapman, D. R. and Rubesin, M. W., "Temperature and Velocity Profiles in the Compressible Laminar Boundary Layer with Arbitrary Distribution of Surface Temperature," *Journal of the Aeronautical Sciences*, Vol. 16, Sep., 1949.

[2]Schlicting, H., *Boundary Layer Theroy*, McGraw-Hill, New York, 1955.

[3]Ginoux, J. J., *Laminar Boundary Layers*, VKI CN 104, Dec., 1978.

Reviews of General Shock Wave / Boundary Layer Interaction Theory

[4]Lees, L., and Reeves, B. L., "Supersonic Separated and Reattaching Laminar Flows: I. General Theory and Application to Adiabatic Boundary-Layer/Shock-Wave Interactions," *AIAA Journal*, Vol. 2, Nov. 1964, pp. 1907-1920.

[5]Green, J. E., "Interactions Between Shock Waves and Turbulent Boundary Layers," *Progress in Aerospace Sciences*, Vol. 11, 1970, pp. 235-336.

[6]Settles, G. S. and Dolling, D. S., "Swept Shock Wave / Boundary Layer Interactions," *AIAA Progress in Astronautics and Aeronautics: Tactical Missile Aerodynamics*, edited by J. Nielsen and M. Hemsch, AIAA, New York, 1986.

[7]Settles, G. S. and Dolling, D. S., "Swept Shock / Boundary Layer Interactions - Tutorial and Update," AIAA Paper 90-0375, Reno, NV, Jan 1990.

Shock Wave / Laminar Boundary Layer Interactions

[8]Degrez, G., "Etude Theorique et Experimentale D'interactions bi- et tri- dimensionnelles entre ondes de choc et couches limites laminaires," Thèse de Doctorat, Université Libre de Bruxelles, 1984.

[9]Degrez, G. and Ginoux, J. J., "Surface Phenomena in a Three-Dimensional Skewed Shock Wave/Laminar Boundary-Layer Interaction," *AIAA Journal*, Vol. 22, Dec. 1984, pp. 1764-1769.

[10]Degrez, G, Boccadoro, C. H., and Wendt, J. F., "The interaction of an oblique shock wave with a laminar boundary layer revisited. An experimental and numerical study," *J. Fluid Mech.*, Vol. 177, 1987, pp. 247-263.

Shock Wave / Turbulent Boundary Layer Interactions

[11]Lewis, J. E., Kubota, T., and Lees, L., "Experimental Investigation of Supersonic Laminar, Two-Dimensional Boundary-Layer Separation in a Compression Corner with and without Cooling," *AIAA Journal*, Vol. 6, Jan. 1968, pp. 7-14.

[12]Oskam, B., Vas, I. E., and Bogdonoff, S. M., "Mach 3 Oblique Shock Wave/Turbulent Boundary Layer Interactions in Three Dimensions," AIAA Paper 76-336, San Diego, CA, July 1976.

[13]Modarress, D. and Johnson, D. A., "Investigation of Turbulent Boundary-Layer Separation Using Laser Velocimetry," *AIAA Journal*, Vol. 17, July 1979, pp. 747-752.

[14]Settles, G. S., Perkins, J. J., and Bogdonoff, S. M., "Investigation of Three-Dimensional Shock/Boundary Layer Interactions at Swept Compression Corners," *AIAA Journal*, Vol. 18, July 1980, pp. 779-785.

[15]Dolling, D. S., "Comparison of Sharp and Blunt Fin-Induced Shock Wave/Turbulent Boundary-Layer Interaction," *AIAA Journal*, Vol. 20, Oct. 1982, pp. 1385-1390.

[16]Settles, G. S. and Teng, H. Y., "Cylindrical and Conical Flow Regimes of Three-Dimensional Shock/Boundary-Layer Interactions," *AIAA Journal*, Vol. 22, Feb. 1984, pp. 194-200.

[17]Settles, G. S. and Lu, F. K., "Conical Similarity of Shock/Boundary-Layer Interactions Generated by Swept and Unswept Fins," *AIAA Journal*, Vol. 23, July 1985, pp. 1021-1027.

[18]Knight, D., Horstman, C., Shapey, B., and Bogdonoff, S., "The Flowfield Structure of the 3-D Shock Wave - Boundary Layer Interaction Generated by a 20 deg Sharp Fin at Mach 3," AIAA Paper 86-0343, Reno, NV, Jan 1986.

[19]Settles, G. S. and Kimmel, R. L., "Similarity of Qausiconical Shock Wave/Turbulent Boundary-Layer Interactions," *AIAA Journal*, Vol. 24, Jan. 1986, pp. 47-53.

[20]Zang, Y. and Knight, D., "Computation of Sharp Fin and Swept Compression Corner Shock/Turbulent Boundary Layer Interactions," AIAA Paper 89-1852, Buffalo, NY, June 1989.

[21]Chpoun, A., "Hypersonic Flow in a Compression Corner in 2-D and 3-D Configurations," AIAA Paper 89-1876, Buffalo, NY, June 1989.

[22]Alvi, F., and Settles, G., "Structure of Swept Shock Wave/Boundary-Layer Interactions Using Conical Shadowgraphy," AIAA Paper 90-1644, Seattle, WA, June, 1990.

Measurement Techniques

[23]Hecht, E. and Zajac, A., "Optics", Addison-Wesley, Reading, MA, 1974.

[24]Degrez, G. and Ginoux, J. J., "Velocity Measurements in a 3D Shock Wave Laminar Boundary Layer Interaction," AFOSR Final Scientific Report, AFOSR Grant 83-0273, July 1987.

[25]Settles, G. S. and Teng, H. Y., "Flow Visualization Methods for Separated Three-Dimensional Shock Wave/Turbulent Boundary-Layer Interactions," *AIAA Journal*, Vol. 21, March 1983, pp. 390-397.

[26]Nichols, C. E., Jr, "Preparation of Polystyrene Microspheres for Laser Velocimetry in Wind Tunnels," NASA TM 89-163, June 1987.

[27]Aso, S., Tan, A., and Hayashi, M., "The Structure of Aerodynamic Heating in Three-Dimensional Shock Wave/Turbulent Boundary Layer Interactions Induced by Sharp and Blunt Fins," AIAA Paper 89-1854, Buffalo, NY, June 1989.

[28]Gibertini, G., *Particle Size Effects in LDV Measurements of the Vortical Flow on a Delta Wing*, VKI PR 1988-19, June 1988.

[29]Calta, C. A., *LDV Measurements in a high speed boundary layer*, VKI PR 1986-18, June 1986.

Error Analysis

[30]Kline, S. J., and F. A. McClintock, "Describing Uncertainties in Single-Sample Experiments," *Mech. Eng.*, Jan. 1953, pp. 3-8.

[31]Press, W. H., B. P. Flannery, S. A. Teukolsky, and W. T. Vetterling, *Numerical Recipes, the Art of Scientific Computing*, Cambridge University Press, Cambridge, 1986, pp. 498-506.

Cone Flow Solutions

[32]Ames Research Staff, *Equations, Tables, and Charts for Compressible Flow*, NACA Report 1135, (1953).

[33]Thompson, P. A., *Compressible-Fluid Dynamics*, Maple Press Co., 1984, pp. 487-495.

Droplet Evaporation

[34]Bird, R. B., Stewart, W. E., and Lightfoot, E. N., *Transport Phenomena*, John Wiley and Sons, New York, 1960, pp. 648-649.

[35]Weast, R. C., Astle, M. J., and Beyer, W. H., *CRC Handbook of Chemistry and Physics*, CRC Press, Inc., Boca Raton, Florida, 1984.

Numerical Methods

[36]Davis, R. T., "Numerical Methods for Coordinate Generation Based on Schwarz-Christoffel Transformations," AIAA Paper 79-1463, 1979.

[37]Lardy, P., *Investigation of upwind space discretiaztions for the Navier-Stokes Equations and Application to Conical Supersonic and Hypersonic Flows*, NASA TM 89-163, June 1987.

[38]Bewley, T. R., *An Application of Conformal Mappings to General Grid Generation and Potential Flow Problems*, to be published as a VKI TN, November, 1990

Tunnel Design

[39]Baron, J. R., *Analytic Design of a Family of Supersonic Nozzles by Friedrichs Method, including computation tables and a summary of calibration data*, N.S.L. MIT - WADC Technical Report 54-279, June 1954.

[40]Ginoux, J., *The T.C.E.A. Continuous Supersonic Wind Tunnel S-1*, TCEA TM 7, Oct. 1960.